

Simultaneous Measurement of Oscillation Parameters in Beam and Atmospheric Neutrino Data from Tokai-to-Kamioka and Super-Kamiokande Experiments

Daniel Robert Clement Barrow

Magdalen College, Oxford University

¹⁰ A Dissertation Submitted to Oxford University

¹¹ for the Degree of Doctor of Philosophy

¹²

13 **Simultaneous Measurement of**

14 **Oscillation Parameters in Beam and**

15 **Atmospheric Neutrino Data from**

16 **Tokai-to-Kamioka and**

17 **Super-Kamiokande Experiments**

18 *Abstract*

19 Lorem ipsum dolor sit amet, consectetur adipiscing elit, sed do eiusmod tempor incididunt ut labore et dolore magna aliqua. Nulla aliquet porttitor lacus luctus accumsan tortor posuere. Pulvinar neque laoreet suspendisse interdum. Sem viverra aliquet eget sit. Nunc sed velit dignissim sodales ut eu sem integer vitae. At erat pellentesque adipiscing commodo elit at imperdiet dui accumsan. Fames ac turpis egestas integer eget aliquet nibh. Scelerisque eu ultrices vitae auctor eu augue. Purus non enim praesent elementum facilisis leo vel. Sollicitudin nibh sit amet commodo. Vitae auctor eu augue ut. Vel quam elementum pulvinar etiam. A condimentum vitae sapien pellentesque habitant morbi tristique senectus. Viverra accumsan in nisl nisi scelerisque eu ultrices. Sed viverra ipsum nunc aliquet bibendum enim. Sit amet purus gravida quis. In vitae turpis massa

³² sed elementum tempus egestas sed sed. Vivamus arcu felis bibendum
³³ ut tristique et egestas. Senectus et netus et malesuada fames ac turpis.
³⁴ Ac auctor augue mauris augue.

35 Declaration

36 This dissertation is the result of my own work, except where ex-
37 plicit reference is made to the work of others, and has not been sub-
38 mitted for another qualification to this or any other university. This
39 dissertation does not exceed the word limit for the respective Degree
40 Committee.

41 Daniel Robert Clement Barrow

42 ©The copyright of this thesis rests with the author and is made available under a Creative
43 Commons Attribution Non-Commercial No Derivatives licence. Researchers are free to copy,
44 distribute or transmit the thesis on the condition that they attribute it, that they do not use
45 it for commercial purposes and that they do not alter, transform or build upon it. For any
46 reuse or redistribution, researchers must make clear to others the licence terms of this work.

47

Acknowledgements

48 at pretium nibh ipsum. Eget nunc scelerisque viverra mauris in aliquam. Arcu vitae
49 elementum curabitur vitae nunc sed velit dignissim. Sed arcu non odio euismod lacinia
50 at quis risus sed. Vitae tempus quam pellentesque nec nam aliquam sem et tortor.
51 Viverra aliquet eget sit amet tellus cras adipiscing. Purus sit amet luctus venenatis
52 lectus magna. In aliquam sem fringilla ut morbi tincidunt augue. Fermentum dui
53 faucibus in ornare. Aliquam malesuada bibendum arcu vitae elementum curabitur
54 vitae nunc sed.

55 Ultricies leo integer malesuada nunc vel risus commodo. Tellus cras adipiscing
56 enim eu turpis egestas pretium. Dictumst quisque sagittis purus sit amet volutpat
57 consequat mauris nunc. Vitae congue mauris rhoncus aenean vel elit scelerisque
58 mauris pellentesque. Vel facilisis volutpat est velit egestas dui id ornare. Suscipit
59 adipiscing bibendum est ultricies. At in tellus integer feugiat scelerisque varius
60 morbi enim. Cras semper auctor neque vitae tempus. Commodo sed egestas egestas
61 fringilla phasellus faucibus. Cras pulvinar mattis nunc sed blandit. Pretium viverra
62 suspendisse potenti nullam ac tortor vitae. Purus sit amet volutpat consequat. Orci
63 sagittis eu volutpat odio facilisis mauris. Sit amet massa vitae tortor condimentum
64 lacinia quis. Commodo sed egestas egestas fringilla phasellus. Sed libero enim sed
65 faucibus turpis. Vitae tempus quam pellentesque nec.

66 Blandit massa enim nec dui. Viverra tellus in hac habitasse platea dictumst vestibulu-
67 lum. Bibendum enim facilisis gravida neque convallis. Sagittis nisl rhoncus mattis
68 rhoncus urna neque. Nisl rhoncus mattis rhoncus urna neque. Ac tortor vitae purus
69 faucibus ornare. Aenean sed adipiscing diam donec adipiscing tristique risus. Sapien
70 nec sagittis aliquam malesuada bibendum. Et leo duis ut diam quam nulla. Tellus
71 rutrum tellus pellentesque eu tincidunt tortor aliquam nulla facilisi. Fermentum leo

⁷² vel orci porta non pulvinar neque. Eget sit amet tellus cras adipiscing enim eu. Sed
⁷³ viverra tellus in hac habitasse platea dictumst vestibulum.

⁷⁴ Sit amet consectetur adipiscing elit. At varius vel pharetra vel turpis nunc eget
⁷⁵ lorem. Elit scelerisque mauris pellentesque pulvinar pellentesque habitant morbi
⁷⁶ tristique senectus. Odio euismod lacinia at quis risus sed vulputate odio. Vitae suscipit
⁷⁷ tellus mauris a diam maecenas sed enim ut. Dignissim convallis aenean et tortor at
⁷⁸ risus viverra. Diam sollicitudin tempor id eu. Erat velit scelerisque in dictum. Blandit
⁷⁹ cursus risus at ultrices. Ac tortor vitae purus faucibus ornare suspendisse sed.

Contents

81	1 Neutrino Oscillation Physics	1
82	1.1 Discovery of Neutrinos	1
83	1.2 Theory of Neutrino Oscillation	3
84	1.2.1 Three Flavour Oscillations	3
85	1.2.2 The MSW Effect	7
86	1.3 Neutrino Oscillation Measurements	9
87	1.3.1 Solar Neutrinos	9
88	1.3.2 Atmospheric Neutrinos	12
89	1.3.3 Accelerator Neutrinos	15
90	1.3.4 Reactor Neutrinos	18
91	2 T2K and SK Experiment Overview	20
92	2.1 The Super-Kamiokande Experiment	21
93	2.1.1 The SK Detector	22
94	2.1.2 Calibration	25
95	2.1.3 Data Acquisition and Triggering	28
96	2.1.4 Cherenkov Radiation	30
97	2.2 The Tokai to Kamioka Experiment	32
98	2.2.1 The Neutrino Beam	33
99	2.2.2 The Near Detector at 280m	38
100	2.2.2.1 Fine Grained Detectors	40
101	2.2.2.2 Time Projection Chambers	41
102	2.2.2.3 π^0 Detector	42
103	2.2.2.4 Electromagnetic Calorimeter	44
104	2.2.2.5 Side Muon Range Detector	45

105	2.2.3 The Interactive Neutrino GRID	45
106	3 Bayesian Statistics and Markov Chain Monte Carlo Techniques	48
107	3.1 Bayesian Statistics	49
108	3.2 Monte Carlo Simulation	50
109	3.2.1 Markov Chain Monte Carlo	52
110	3.2.2 Metropolis-Hastings Algorithm	55
111	3.2.3 MCMC Optimisation	56
112	3.3 Understanding the MCMC Results	60
113	3.3.1 Marginalisation	60
114	3.3.2 Parameter Estimation and Credible Intervals	61
115	3.3.3 Application of Bayes' Theorem	63
116	3.3.4 Comparison of MCMC Output to Expectation	64
117	4 Simulation, Reconstruction and Event Selections	66
118	4.1 Simulation	66
119	4.2 Event Reconstruction at SK	71
120	4.3 Event Selection at SK	81
121	5 Oscillation Probability Calculation	86
122	5.1 Overview	87
123	5.2 Treatment of Fast Oscillations	94
124	5.3 Calculation Engine	103
125	5.4 Matter Density Profile	104
126	5.5 Production Height Averaging	111
127	Bibliography	115
128	List of Figures	126

129 List of Tables**134**

¹³¹ **Chapter 1**

¹³² **Neutrino Oscillation Physics**

¹³³ When first proposed, neutrinos were expected to be massless fermions that only in-
¹³⁴ teract through weak and gravitational forces. This meant they were very difficult to
¹³⁵ detect as they can pass through significant amounts of matter without interacting. De-
¹³⁶ spite this, experimental neutrino physics has developed with many different detection
¹³⁷ techniques and neutrino sources being used today. In direct tension with **the** standard
¹³⁸ model physics, neutrinos have been determined to oscillate between different lepton
¹³⁹ flavours, requiring them to have mass.

¹⁴⁰ **The observation techniques which lead to the discovery of the neutrino are doc-**
¹⁴¹ **umented in section 1.1.** The theory underpinning neutrino oscillation is described in
¹⁴² section 1.2. This section includes the approximations which can be made to simplify
¹⁴³ the understanding of neutrino oscillation in a two-flavour approximation as well
¹⁴⁴ as how the medium in which neutrinos propagate can manipulate the oscillation
¹⁴⁵ probability. **Past**, current, and future neutrino experiments are detailed in section 1.3,
¹⁴⁶ including the reactor, atmospheric, and long-baseline accelerator neutrino sources that
¹⁴⁷ have been used to successfully constrain oscillation **parameters determination**.

¹⁴⁸ **1.1 Discovery of Neutrinos**

¹⁴⁹ At the start of the 20th century, the electrons emitted from the β -decay of the nucleus
¹⁵⁰ were found to have a continuous energy spectrum [1,2]. This observation seemingly
¹⁵¹ broke the energy conservation invoked within that period's nuclear models. Postulated

in 1930 by Pauli as the solution to this problem, the neutrino (originally termed “neutron”) was theorized to be an electrically neutral spin-1/2 fermion with a mass of the same order of magnitude as the electron [3]. This neutrino was to be emitted with the electron in β -decay to alleviate the apparent breaking of energy conservation. As a predecessor of **the today's** weak interaction model, Fermi's theory of β -decay developed the understanding by coupling the four constituent particles; electron, proton, neutron, and neutrino, into a consistent model [4].

Whilst Pauli was not convinced of the ability to detect neutrinos, **the first observations of the particle were made in the mid-1950s when neutrinos from a reactor were observed via the inverse β -decay (IBD) process, $\bar{\nu}_e + p \rightarrow n + e^+$ [5, 6]. The detector consisted of two parts: a neutrino interaction medium and a liquid scintillator.** The interaction medium was built from two water tanks. These were loaded with cadmium chloride to allow increased efficiency of neutron capture. The positron emitted from IBD annihilates, $e^+ + e^- \rightarrow 2\gamma$, generating a prompt signal and the neutron is captured on the cadmium via $n + ^{108}Cd \rightarrow ^{109^*}Cd \rightarrow ^{109}Cd + \gamma$, producing a delayed signal. **The experiment observed an increase in the neutrino event rate when the reactor was operating compared to when it was switched off, in much the same way as modern reactor neutrino experiments operate. An increase in the coincidence rate was observed when the reactor was operating which was interpreted as interactions from neutrinos generated in the reactor.**

After the discovery of the ν_e , the natural question of how many flavours of neutrino exist was asked. In 1962, a measurement of the ν_μ was conducted at the Brookhaven National Laboratory [7]. A proton beam was directed at a beryllium target, generating a π -dominated beam which then decayed via $\pi^\pm \rightarrow \mu^\pm + (\nu_\mu, \bar{\nu}_\mu)$, and the subsequent interactions of the ν_μ were observed. **As the subsequent interaction of the neutrino generates muons rather than electrons, it was determined the ν_μ was**

178 **fundamentally different from ν_e .** The final observation to be made was that of the
179 ν_τ from the DONUT experiment [8]. Three neutrinos seem the obvious solution as it
180 mirrors the known number of charged lepton (as they form weak isospin doublets) but
181 there could be evidence of more. Several neutrino experiments have found anomalous
182 results [9, 10] which could be attributed to sterile neutrinos however cosmological
183 observations indicate the number of neutrino species $N_{eff} = 2.99 \pm 0.17$ [11]. DB:
184 Need to determine how N_{eff} is calculated.

185 1.2 Theory of Neutrino Oscillation

186 As direct evidence of beyond Standard Model physics, a neutrino generated with
187 lepton flavour α can change into a different lepton flavour β after propagating some
188 distance. This phenomenon is called neutrino oscillation and requires that neutrinos
189 must have a non-zero mass (as seen in subsection 1.2.1). This **observation** is direct
190 evidence of beyond standard model physics. This behaviour has been characterised
191 by the Pontecorvo-Maki-Nakagawa-Sakata (PMNS) [12–14] mixing matrix which
192 describes how the flavour and mass of neutrinos are associated. This is analogous to
193 the Cabibbo-Kobayashi-Maskawa (CKM) [15] matrix measured in quark physics.

194 1.2.1 Three Flavour Oscillations

195 The PMNS parameterisation defines three flavour eigenstates, ν_e , ν_μ and ν_τ (indexed
196 ν_α), which are **assigned based upon eigenstates of** the weak interaction **flavour states**
197 and three mass eigenstates, ν_1 , ν_2 and ν_3 (indexed ν_i). Each mass eigenstate is the
198 superposition of all three flavour states,

$$|\nu_i\rangle = \sum_{\alpha} U_{\alpha i} |\nu_{\alpha}\rangle. \quad (1.1)$$

199 Where U is the PMNS matrix which **is unitary and connects correlates** the mass
200 and flavour eigenstates.

201 ~~Neutrinos interact with leptons of the same weak flavour eigenstate rather than~~
202 ~~mass eigenstate. The weak interaction couples to flavour eigenstates so neutrinos~~
203 ~~interact with leptons of the same flavour.~~ The propagation of a neutrino flavour
204 eigenstate, in a vacuum, can be re-written as a plane-wave solution to the time-
205 dependent Schrödinger equation,

$$|\nu_{\alpha}(t)\rangle = \sum_i U_{\alpha i}^* |\nu_i\rangle e^{-i\phi_i}. \quad (1.2)$$

206 The probability of observing a neutrino of flavour eigenstate β from one which
207 originated as flavour α can be calculated as,

$$P(\nu_{\alpha} \rightarrow \nu_{\beta}) = |\langle \nu_{\beta} | \nu_{\alpha}(t) \rangle|^2 = \sum_{i,j} U_{\alpha i}^* U_{\beta i} U_{\alpha j} U_{\beta j}^* e^{-i(\phi_j - \phi_i)} \quad (1.3)$$

208 The ϕ_i term can be expressed in terms of the energy, E_i , and magnitude of the
209 three momenta, p_i , of the neutrino, $\phi_i = E_i t - p_i x$ (t and x being time and position
210 coordinates). Therefore,

$$\phi_j - \phi_i = E_j t - E_i t - p_j x + p_i x. \quad (1.4)$$

²¹¹ For a relativistic particle, $E_i \gg m_i$,

$$p_i = \sqrt{E_i^2 - m_i^2} \approx E_i - \frac{m_i^2}{2E_i}. \quad (1.5)$$

²¹² Making the approximations that neutrinos are relativistic, the mass eigenstates
²¹³ were created with the same energy and that $x = L$, where L is the distance traveled by
²¹⁴ the neutrino, Equation 1.4 then becomes

$$\phi_j - \phi_i = \frac{\Delta m_{ij}^2 L}{2E}, \quad (1.6)$$

²¹⁵ where $\Delta m_{ij}^2 = m_i^2 - m_j^2$. This, **teamed combined** with further use of unitarity
²¹⁶ relations results in Equation 1.3 becoming

$$\begin{aligned} P(\nu_\alpha \rightarrow \nu_\beta) &= \delta_{\alpha\beta} - 4 \sum_{i>j} \Re \left(U_{\alpha i}^* U_{\beta i} U_{\alpha j} U_{\beta j}^* \right) \sin^2 \left(\frac{\Delta m_{ij}^2 L}{4E} \right) \\ &\quad + (-) 2 \sum_{i>j} \Im \left(U_{\alpha i}^* U_{\beta i} U_{\alpha j} U_{\beta j}^* \right) \sin \left(\frac{\Delta m_{ij}^2 L}{2E} \right). \end{aligned} \quad (1.7)$$

²¹⁷ Where $\delta_{\alpha\beta}$ is the Kronecker delta function and the negative sign **on the last term** is
²¹⁸ included for the oscillation probability of antineutrinos.

²¹⁹ Typically, the PMNS matrix is parameterised into three mixing angles, a charge
²²⁰ parity (CP) violating phase δ_{CP} , and two Majorana phases $\alpha_{1,2}$,

$$U = \underbrace{\begin{pmatrix} 1 & 0 & 0 \\ 0 & c_{23} & s_{23} \\ 0 & -s_{23} & c_{23} \end{pmatrix}}_{\text{Atmospheric, Accelerator}} \underbrace{\begin{pmatrix} c_{13} & 0 & s_{13}e^{-i\delta_{CP}} \\ 0 & 1 & 0 \\ -s_{13}e^{-i\delta_{CP}} & 0 & c_{13} \end{pmatrix}}_{\text{Reactor, Accelerator}} \underbrace{\begin{pmatrix} c_{12} & s_{12} & 0 \\ -s_{12} & c_{12} & 0 \\ 0 & 0 & 1 \end{pmatrix}}_{\text{Reactor, Solar}} \underbrace{\begin{pmatrix} e^{i\alpha_1/2} & 0 & 0 \\ 0 & e^{i\alpha_2/2} & 0 \\ 0 & 0 & 1 \end{pmatrix}}_{\text{Majorana}}. \quad (1.8)$$

²²¹ Where $s_{ij} = \sin(\theta_{ij})$ and $c_{ij} = \cos(\theta_{ij})$. The oscillation parameters are often
²²² grouped; (1,2) as “solar”, (2,3) as “atmospheric” and (1,3) as “reactor”. Many
²²³ neutrino experiments aim to measure the PMNS parameters from a wide array of
²²⁴ origins, as is the purpose of this thesis.

²²⁵ The Majorana phase, $\alpha_{1,2}$, **containing matrix** included within **the fourth matrix**
²²⁶ **in** Equation 1.8 is only included for completeness. For an oscillation analysis ex-
²²⁷ periment, **any term in this oscillation probability calculation containing this phase**
²²⁸ **disappears any terms containing thtis phase disappear** due to taking the expectation
²²⁹ value of the PMNS matrix. **Measurements of these phases are typically performed**
²³⁰ **by experiments searching for neutrino-less double β -decay [16].**

²³¹ A two flavour approximation can be **attained obtained** when one assumes the third
²³² mass eigenstate is degenerate with another. As discussed in section 1.3, it is found
²³³ that $\Delta m_{21}^2 \ll |\Delta m_{31}^2|$. This results in the two flavour approximation being reasonable
²³⁴ for understanding the features of the oscillation. In this two flavour case, the mixing
²³⁵ matrix becomes,

$$U_{2 \text{ Flav.}} = \begin{pmatrix} \cos(\theta) & \sin(\theta) \\ -\sin(\theta) & \cos(\theta) \end{pmatrix}. \quad (1.9)$$

²³⁶ This culminates in the oscillation probability,

$$\begin{aligned} P(\nu_\alpha \rightarrow \nu_\alpha) &= 1 - \sin^2(2\theta) \sin^2\left(\frac{\Delta m^2 L}{4E}\right), \\ P(\nu_\alpha \rightarrow \nu_\beta) &= \sin^2(2\theta) \sin^2\left(\frac{\Delta m^2 L}{4E}\right). \end{aligned} \quad (1.10)$$

²³⁷ **For Where** $\alpha \neq \beta$. For a fixed neutrino energy, the oscillation probability is a sinusoidal function depending upon the distance over which the neutrino propagates. The ²³⁸ frequency and amplitude of oscillation are dependent upon **the ratio of the** $\Delta m^2 / 4E$ ²³⁹ and $\sin^2 2\theta$, respectively. **The oscillation probabilities presented thus far assume** ²⁴⁰ **c = 1, where c is the speed of light in vacuum. In more familiar units**, the maximum ²⁴¹ oscillation probability for a fixed value of θ is given at $L[\text{km}] / E[\text{GeV}] \sim 1.27 / \Delta m^2$. ²⁴² It is this calculation that determines the best L/E value for a given experiment to be ²⁴³ designed around for measurements of a specific value of Δm^2 . ²⁴⁴

²⁴⁵ 1.2.2 The MSW Effect

²⁴⁶ The theory of neutrino oscillation in a vacuum **is has been** described in subsection 1.2.1. ²⁴⁷ However, the beam neutrinos and atmospheric neutrinos originating from below the ²⁴⁸ horizon propagate through matter in the Earth. The coherent scattering of neutrinos ²⁴⁹ from a material target modifies the Hamiltonian of the system. This results in a change ²⁵⁰ in the oscillation probability. Notably, charged current scattering ($\nu_e + e^- \rightarrow \nu_e + e^-$,

251 propagated by a W boson) only affects electron neutrinos **compared to whereas** the
252 neutral current scattering ($\nu_l + l^- \rightarrow \nu_l + l^-$, propagated by a Z^0 boson) interacts
253 through all neutrino flavours equally. In the two-flavour **limit approximation**, the
254 effective mixing parameter becomes

$$\sin^2(2\theta) \rightarrow \sin^2(2\theta_m) = \frac{\sin^2(2\theta)}{(A/\Delta m^2 - \cos(2\theta))^2 + \sin^2(2\theta)}, \quad (1.11)$$

255 where $A = 2\sqrt{2}G_F N_e E$, **with** N_e is the electron density of the medium and G_F is
256 Fermi's constant. It is clear to see that there exists a value of $A = \Delta m^2 \cos(2\theta)$ for
257 $\Delta m^2 > 0$ which results in a divergent mixing parameter. This resonance is **due to**
258 **termed** the Mikheyev-Smirnov-Wolfenstein (MSW) effect (or more colloquially, the
259 matter resonance) which regenerates the electron neutrino component of the neutrino
260 flux [17–19]. The density at which the resonance occurs is given by

$$N_e = \frac{\Delta m^2 \cos(2\theta)}{2\sqrt{2}G_F E}. \quad (1.12)$$

261 At densities lower than this critical value, the oscillation probability will be much
262 closer to that of vacuum oscillation. **For antineutrinos, $N_e \rightarrow -N_e$ [20].** The reso-
263 nance occurring from the MSW effect depends on the sign of Δm^2 . Therefore, any
264 neutrino oscillation experiment which observes neutrinos and antineutrinos which
265 have propagated through matter can have some sensitivity to the ordering of the
266 neutrino mass eigenstates.

²⁶⁷ 1.3 Neutrino Oscillation Measurements

²⁶⁸ As evidence of beyond standard model physics, the 2015 Nobel Prize in Physics was
²⁶⁹ awarded to the Super-Kamiokande (SK) [21] and Sudbury Neutrino Observatory
²⁷⁰ (SNO) [22] collaborations for the first definitive observation of solar and atmospheric
²⁷¹ neutrino oscillation [23]. Since then, the field has seen a wide array of oscillation
²⁷² measurements from a variety of neutrino sources. As seen in subsection 1.2.1, the
²⁷³ neutrino oscillation probability is dependent on the ratio of the propagation baseline, L ,
²⁷⁴ to the neutrino energy, E . It is this ratio that determines the type of neutrino oscillation
²⁷⁵ a particular experiment is sensitive to.

²⁷⁶ As illustrated in Figure 1.1, there are many neutrino sources that span a wide
²⁷⁷ range of energies. The least energetic neutrinos are from diffuse supernovae and
²⁷⁸ terrestrial neutrinos at $O(1)$ MeV whereas the most energetic neutrinos originate from
²⁷⁹ atmospheric and galactic neutrinos of $> O(1)$ TeV.

²⁸⁰ 1.3.1 Solar Neutrinos

²⁸¹ Solar neutrinos are emitted from fusion reaction chains at the center of the Sun. The
²⁸² solar neutrino flux, given as a function of neutrino energy for different fusion and
²⁸³ decay chains, is illustrated in Figure 1.2. Whilst proton-proton fusion generates the
²⁸⁴ largest flux of neutrinos, the neutrinos are of low energy and are difficult to reconstruct
²⁸⁵ due to the IBD interaction threshold of 1.8MeV. Consequently, most experiments focus
²⁸⁶ on the neutrinos from the decay of 8B (via $^8B \rightarrow ^8Be^* + e^+ + \nu_e$), which are higher
²⁸⁷ energy.

²⁸⁸ The first measurements of solar neutrinos observed a significant reduction in the
²⁸⁹ event rate compared to predictions from the Standard Solar Model [26, 27]. The

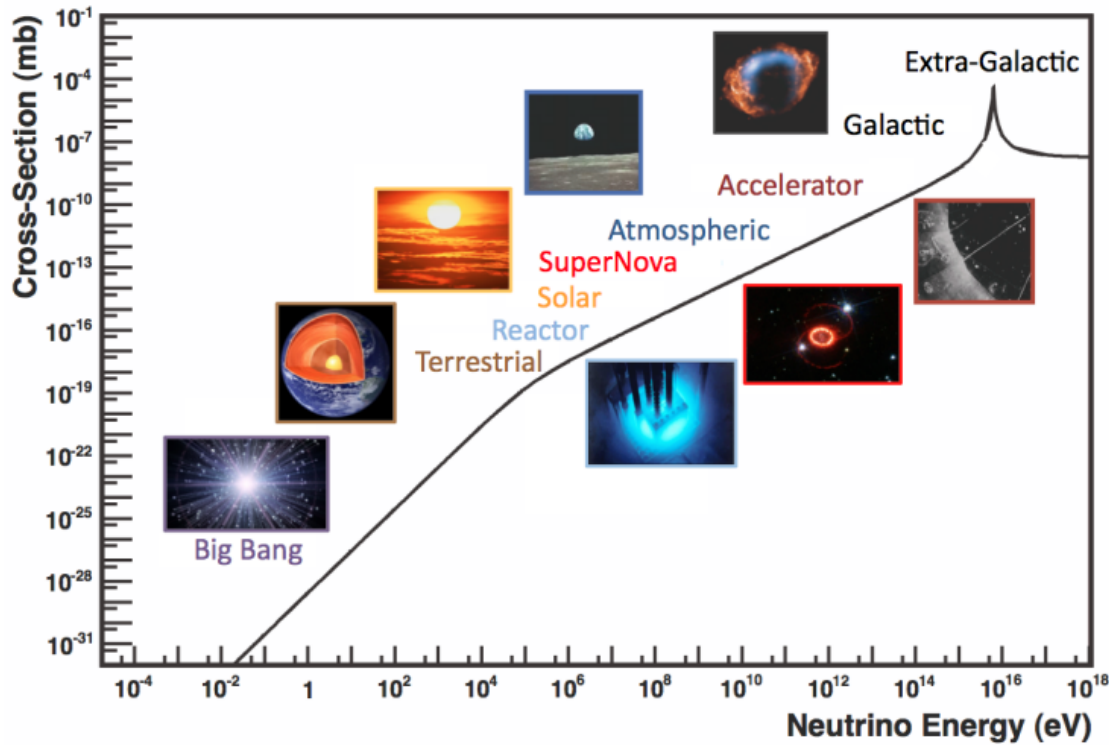


Figure 1.1: The cross-section of neutrinos from various natural and man-made sources as a function of neutrino energy. Taken from [24]

290 proposed solution to this “solar neutrino problem” was $\nu_e \leftrightarrow \nu_\mu$ oscillations in a
 291 precursory version of the PMNS model [28]. The Kamiokande [29], Gallex [30] and
 292 Sage [31] experiments confirmed the ~ 0.5 factor deficit of solar neutrinos.

293 The conclusive solution to this problem was determined by the SNO collabora-
 294 tion [32]. Using a deuterium water target to observe 8B neutrinos, the event rate of
 295 charged current (CC), neutral current (NC), and elastic scattering (ES) interactions
 296 (Given in Equation 1.13) was simultaneously measured. CC events can only occur
 297 for electron neutrinos, whereas the ~~other interaction NC channels are is~~ agnostic
 298 to neutrino flavour (~~Although , and~~ the ES reaction ~~is more sensitive has a slight~~
 299 ~~excess sensitivity~~ to electron neutrino interactions). This meant that there were direct
 300 measurements of the ν_e and ν_x neutrino flux. It was concluded that the CC and ES
 301 interaction rates were consistent with the deficit previously observed. Most impor-

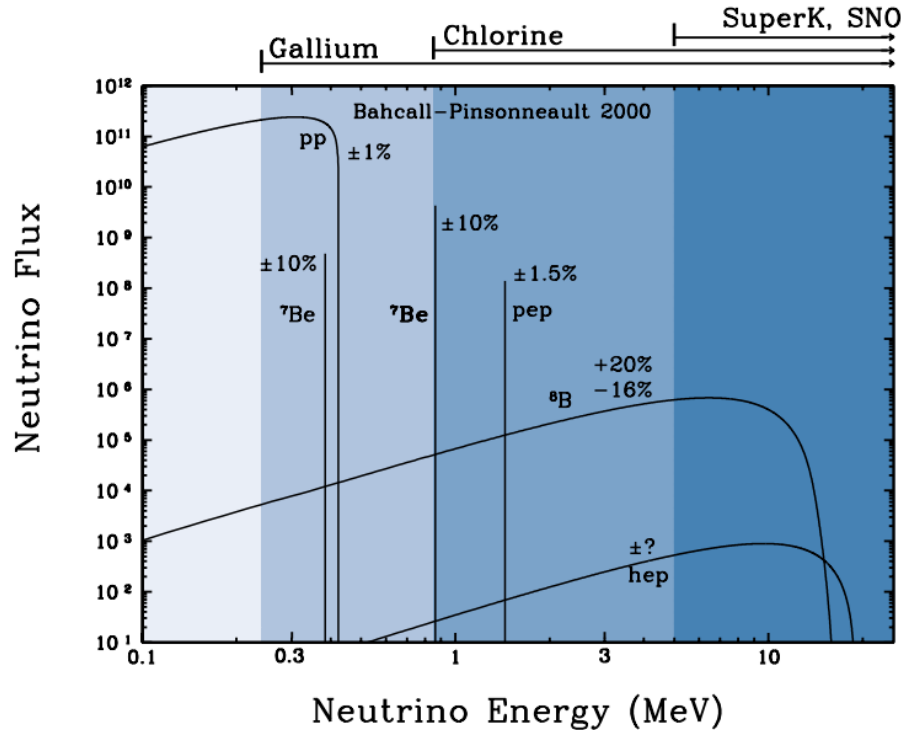
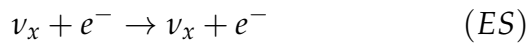
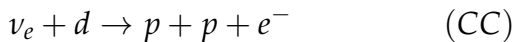


Figure 1.2: The solar neutrino flux as a function of neutrino energy for various fusion reactions and decay chains as predicted by the Standard Solar Model. Taken from [25].

tantly, the NC reaction rate was only consistent with the others under the hypothesis of flavour transformation.



Many experiments have since measured the neutrino flux of different interaction chains within the sun [33–35]. The most recent measurement was that of CNO neutrinos which were recently observed with 5σ significance by the Borexino collaboration. Future neutrino experiments aim to further these spectroscopic measurements of different fusion chains within the Sun [36–38]. Solar neutrinos act as an irreducible

309 background for dark matter experiments like DARWIN but oscillation parameter
310 measurements can be made [39].

311 1.3.2 Atmospheric Neutrinos

312 The interactions of primary cosmic ray protons in Earth's upper atmosphere generate
313 showers of energetic hadrons. These are mostly pions and kaons which when they
314 decay produce a natural source of neutrinos spanning energies of MeV to TeV [40].

315 **This** The main decay is via

$$\begin{aligned} \pi^\pm &\rightarrow \mu^\pm + (\nu_\mu, \bar{\nu}_\mu) \\ \mu^\pm &\rightarrow e^\pm + (\nu_\mu, \bar{\nu}_\mu) + (\nu_e, \bar{\nu}_e) \end{aligned} \tag{1.14}$$

316 such that for a single pion decay, three neutrinos are typically produced. The
317 atmospheric neutrino flux energy spectra as predicted by the Bartol [41], Honda
318 [42–44], and FLUKA [45] models are illustrated in Figure 1.3. The flux distribution
319 peaks at an energy of $O(10)\text{GeV}$. The uncertainties associated with these models
320 are dominated by the hadronic production of kaon and pions as well as the primary
321 cosmic flux.

322 Unlike long-baseline experiments which have a fixed baseline, the distance at-
323 mospheric neutrinos propagate is dependent upon the zenith angle at which they
324 interact. This is illustrated in Figure 1.4. Neutrinos that are generated directly above
325 the detector ($\cos(\theta) = 1.0$) have a baseline equivalent to the height of the atmosphere
326 whereas neutrinos that interact directly below the detector ($\cos(\theta) = -1.0$) have to
327 travel a length equal to the diameter of the Earth. This means atmospheric neutrinos
328 have a baseline that varies from $O(20)\text{km}$ to $O(6 \times 10^3)\text{km}$. Any neutrino generated

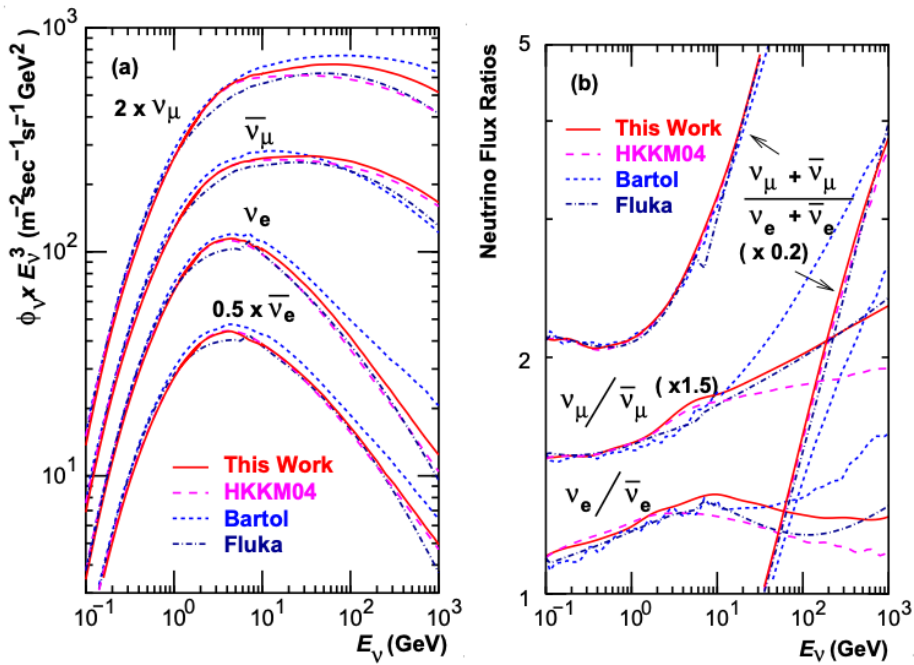


Figure 1.3: Left panel: The atmospheric neutrino flux for different neutrino flavours as a function of neutrino energy as predicted by the 2007 Honda model (“This work”) [42], the 2004 Honda model (“HKKM04”) [43], the Bartol model [41] and the FLUKA model [45]. Right panel: The ratio of the muon to electron neutrino flux as predicted by all the quoted models. Both figures taken from [42].

329 at or below the horizon will be subject to matter effects as they propagate through the
 330 Earth.

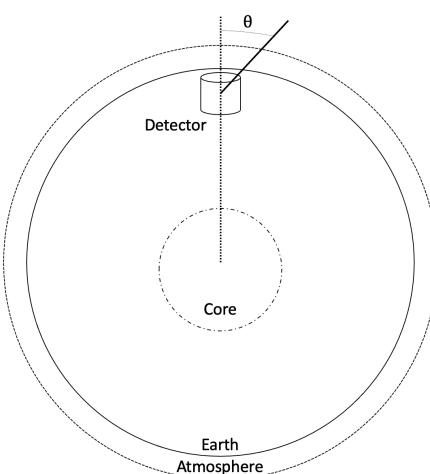


Figure 1.4: A diagram illustrating the definition of zenith angle as used in the Super Kamiokande experiment [46].

Figure 1.5 highlights the neutrino flux as a function of the zenith angle for different slices of neutrino energy. For medium to high-energy neutrinos (and to a lesser degree for low-energy neutrinos), the flux is approximately symmetric around $\cos(\theta) = 0$. To the accuracy of this approximation, the systematic uncertainties associated with atmospheric flux for comparing upward-going and down-going neutrino cancels. This allows the down-going events, which are mostly insensitive to oscillation probabilities, to act as an unoscillated prediction (similar to a near detector in an accelerator neutrino experiment).

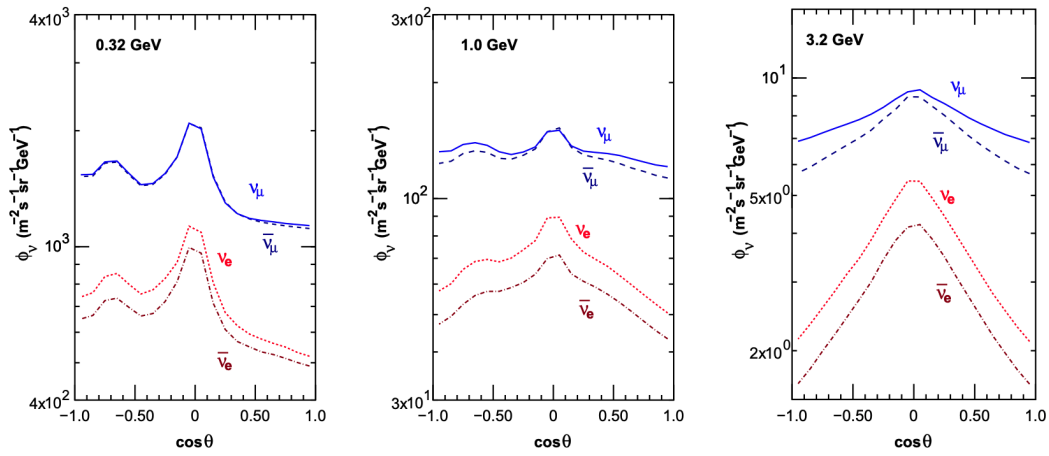


Figure 1.5: Prediction of $\nu_e, \bar{\nu}_e, \nu_\mu, \bar{\nu}_\mu$ fluxes as a function of zenith angle as calculated by the HKKM model [44]. The left, middle and right panels represent three values of neutrino energy, 0.32GeV, 1.0GeV and 3.2GeV respectively. Predictions for other models including Bartol [41], Honda [42] and FLUKA [45] are given in [46].

Precursory hints of atmospheric neutrinos were observed in the mid-1960s searching for $\nu_\mu + X \xrightarrow{(-)} X^* + \mu^\pm$ [47], although it was called an anomaly at the time of measurement. This was succeeded with the IMB-3 [48] and Kamiokande [49] experiments which measured the ratio of muon neutrinos compared to electron neutrinos $R(\nu_\mu/\nu_e)$. Both experiments were found to have a consistent deficit of muon neutrinos, with $R(\nu_\mu/\nu_e) = 0.67 \pm 0.17$ and $R(\nu_\mu/\nu_e) = 0.60^{+0.07}_{-0.06} \pm 0.05$. Super-Kamiokande (SK) [46] extended this analysis by fitting oscillation parameters in $P(\nu_\mu \rightarrow \nu_\tau)$ which found best fit parameters $\sin^2(2\theta) > 0.92$ and $1.5 \times 10^{-3} < \Delta m^2 < 3.4 \times 10^{-3}$ eV².

Since then, atmospheric neutrino experiments have been making precision measurements of the $\sin^2(\theta_{23})$ and Δm_{32}^2 oscillation parameters. Atmospheric neutrino oscillation is dominated by $P(\nu_\mu \rightarrow \nu_\tau)$, where SK observed a 4.6σ discovery of ν_τ appearance [50]. Figure 1.6 illustrates the current estimates on the atmospheric mixing parameters from a wide range of atmospheric and accelerator neutrino observatories.

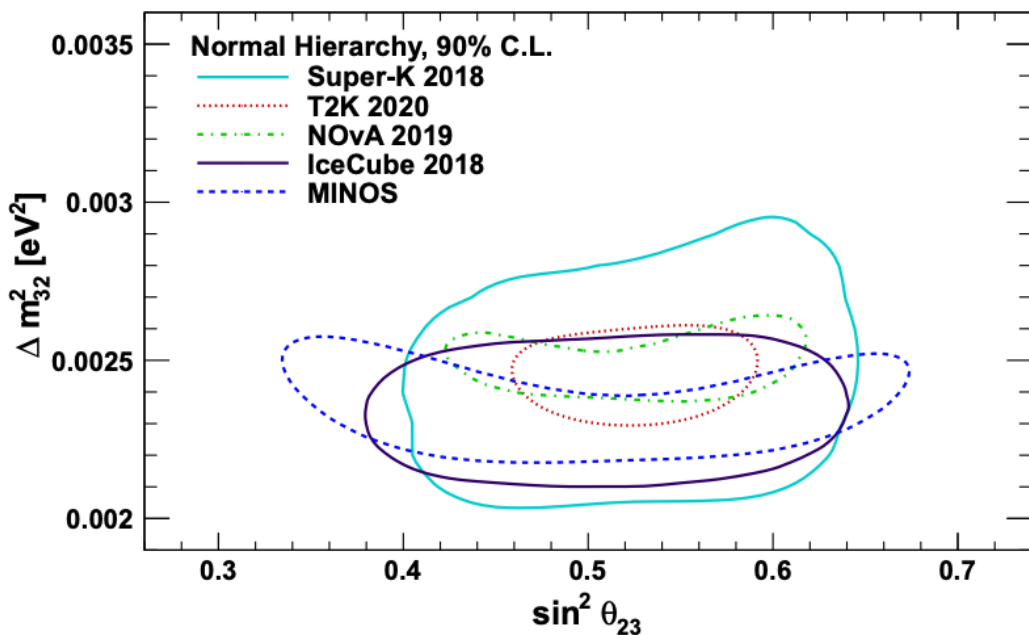


Figure 1.6: Constraints on the atmospheric oscillation parameters, $\sin^2(\theta_{23})$ and Δm_{32}^2 , from atmospheric and long baseline experiments: SK [51], T2K [52], NO ν A [53], IceCube [54] and MINOS [55]. Figure taken from [56].

1.3.3 Accelerator Neutrinos

The concept of using a man-made “neutrino beam” was first realised in 1962 [57]. Since then, many experiments have followed which all use the same fundamental concepts. Typically, a proton beam is aimed at a target producing charged mesons that decay to neutrinos. The mesons can be sign-selected by the use of magnetic focusing horns to generate a neutrino or antineutrino beam. Pions are the primary meson that decay and depending on the orientation of the magnetic field, a muon (anti-)neutrino

beam is generated via $\pi^+ \rightarrow \mu^+ + \nu_\mu$ or $\pi^- \rightarrow \mu^- + \bar{\nu}_\mu$. The decay of muons and kaons does result in an irreducible intrinsic electron neutrino background. In T2K, this background contamination is $O(< 1\%)$ [58]. There is also an approximately $\sim 5\%$ “wrong-sign” neutrino background of $\bar{\nu}_\mu$ generated via the same decays. DB: Need to mention that the beam in proton, not antineutrino so the numu flux is higher in the numubar beam

~~The energy of each neutrino in the beam is dependent on the energy of the initial proton beam. Therefore, tuning the proton energy allows Tuning the proton energy in the beam and using beam focusing techniques allows~~ the neutrino energy to be set to a value that maximises the disappearance oscillation probability in the L/E term in Equation 1.10. This means that accelerator experiments are typically more sensitive to the mixing parameters as compared to a natural neutrino source. However, the disadvantage compared to atmospheric neutrino experiments is that the baseline has to be shorter due to the lower flux. Consequently, there is typically less sensitivity to matter effects and the ordering of the neutrino mass eigenstates.

A neutrino experiment measures

$$R(\vec{x}) = \Phi(E_\nu) \times \sigma(E_\nu) \times \epsilon(\vec{x}) \times P(\nu_\alpha \rightarrow \nu_\beta), \quad (1.15)$$

where $R(\vec{x})$ is the event rate of neutrinos at position \vec{x} , $\Phi(E_\nu)$ is the flux of neutrinos with energy E_ν , $\sigma(E_\nu)$ is the cross-section of the neutrino interaction and $\epsilon(\vec{x})$ is the efficiency **and resolution** of the detector. In order to leverage the most out of an accelerator neutrino experiment, the flux and cross-section systematics need to be constrained. This is typically done via the use of a “near detector”, situated at a baseline

380 of $O(1)$ km. This detector observes the unoscillated neutrino flux and constrains the
381 parameters used within the flux and cross-section model.

382 The first accelerator experiments to precisely measure oscillation parameters were
383 MINOS [59] and K2K [60]. These experiments confirmed the $\nu_\mu \rightarrow \nu_\mu$ **oscillations**
384 ν_μ **disappearance** seen in atmospheric neutrino experiments by finding consistent
385 **mixing** parameter values for $\sin^2(\theta_{23})$ and Δm_{23}^2 . The current generation of accelera-
386 tor neutrino experiments, T2K and NO ν A extended this field by observing $\bar{\nu}_\mu \rightarrow \bar{\nu}_e$
387 and lead the sensitivity to atmospheric mixing parameters as seen in Figure 1.6 [61].
388 The two experiments differ in their peak neutrino energy, baseline, and detection
389 technique. The NO ν A experiment is situated at a baseline of 810km from the NuMI
390 beamline which delivers 2GeV neutrinos. The T2K neutrino beam is peaked around
391 0.6GeV and propagates 295km. The NO ν A experiment also uses functionally iden-
392 tical detectors (near and far) which allow the approximate cancellation of detector
393 systematics whereas T2K uses a plastic scintillator technique at the near detector and
394 a water Cherenkov far detector. The future generation experiments DUNE [62] and
395 Hyper-Kamiokande [63] will succeed these experiments as the high-precision era of
396 neutrino oscillation parameter measurements develops.

397 Several anomalous results have been observed in the LSND [9] and MiniBooNE [10]
398 detectors which were designed with purposefully short baselines. Parts of the neu-
399 trino community attributed these results to oscillations induced by a fourth “sterile”
400 neutrino [64] but several searches in other experiments, MicroBooNE [65] and KAR-
401 MEN [66], found no hints of additional neutrino species. The solution to the anomalous
402 results **are is** still being determined.

⁴⁰³ 1.3.4 Reactor Neutrinos

⁴⁰⁴ As illustrated in the first discovery of neutrinos (section 1.1), nuclear reactors are a very
⁴⁰⁵ useful man-made source of electron antineutrinos. For reactors that use low-enriched
⁴⁰⁶ uranium ^{235}U as fuel, the antineutrino flux is dominated by the β -decay fission of ^{235}U ,
⁴⁰⁷ ^{238}U , ^{239}Pu and ^{241}Pu [67] as illustrated in Figure 1.7.

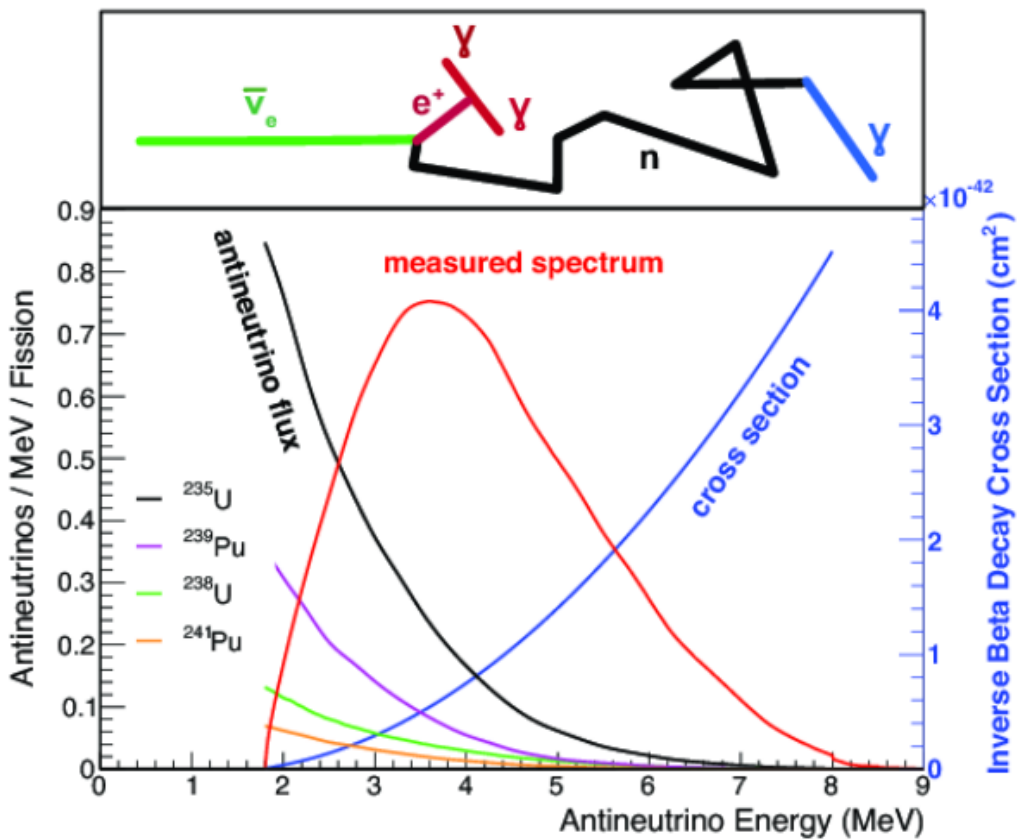


Figure 1.7: Reactor electron antineutrino fluxes for ^{235}U (Black), ^{238}U (Green), ^{239}Pu (Purple), and ^{241}Pu (Orange) isotopes. The inverse β -decay cross-section (Blue) and corresponding measurable neutrino spectrum (Red) are also given. Top panel: Schematic of Inverse β -decay interaction including the eventual capture of the emitted neutron. This capture emits a γ -ray which provides a second signal of the event. Taken from [68].

⁴⁰⁸ Due to their low energy, reactor electron antineutrinos predominantly interact
⁴⁰⁹ via the inverse β -decay (IBD) interaction. The typical signature contains two signals
⁴¹⁰ delayed by $O(200)\mu\text{s}$; firstly the prompt photons from positron annihilation, and

411 secondly the photons emitted ($E_{tot}^\gamma = 2.2\text{MeV}$) from de-excitation after neutron capture
412 on hydrogen. Searching for both signals improves the detector's ability to distinguish
413 between background and signal events [69]. Recently, SK included gadolinium dopants
414 into the ultra-pure water to increase the energy released from the photon cascade to
415 $\sim 8\text{MeV}$ and reduce the time of the delayed signal to $\sim 28\mu\text{s}$.

416 There are many short baseline experiments ($L \sim O(1)\text{km}$) that have measured the
417 $\sin^2(\theta_{13})$ and Δm_{23}^2 oscillation parameters. Daya Bay [70], RENO [71] and Double
418 Chooz [72] have all provided precise measurements, with the first discovery of a
419 non-zero θ_{13} made by Daya Bay and RENO (and ~~complimented complemented~~ by
420 T2K [72]). The constraints on $\sin^2(\theta_{13})$ by the reactor experiments lead the field and
421 are often used as external inputs to accelerator neutrino experiments to improve their
422 sensitivity to δ_{CP} and mass hierarchy determination. JUNO-TAO [73], a small collabora-
423 ration within the larger JUNO experiment, is a next-generation reactor experiment that
424 aims to precisely measure the isotopic antineutrino yields from the different fission
425 chains. Alongside this, it aims to explain the '5MeV excess' [74–76] by conducting a
426 search for sterile neutrinos with a mass scale of around 1eV.

427 Kamland [77] is the only experiment to have observed reactor neutrinos using a
428 long baseline (flux weighted averaged baseline of $L \sim 180\text{km}$) which allows it to have
429 sensitivity to Δm_{12}^2 . Combined with the SK solar neutrino experiment, the combined
430 analysis puts the most stringent constraint on Δm_{12}^2 [78] ~~which is used as a prior~~
431 ~~uncertainty within accelerator neutrino experiments.~~

432 DB: Include a conclusion section with PDG results

⁴³³ **Chapter 2**

⁴³⁴ **T2K and SK Experiment Overview**

⁴³⁵ As the successor of the Kamiokande experiment, the Super-Kamiokande (SK) collaboration has been leading atmospheric neutrino oscillation analyses for over two decades.
⁴³⁶ The detector has provided some of the strongest constraints on proton decay **limits** and **as well as** the first precise measurements of the Δm_{23}^2 and $\sin^2(\theta_{23})$ neutrino oscillation parameters. **Despite this, the The** ability of the detector to low-energy neutrino events has been significantly improved with the recent gadolinium doping of the ultra-pure water target. **section 2.1 describes the history, detection technique, and operation of the SK detector. The history, detection technique, and operation of the SK detector is described in section 2.1.**

⁴⁴⁴ The Tokai-to-Kamioka (T2K) experiment was one of the first long-baseline experiments to use both neutrino and antineutrino beams to precisely measure the charge parity violation within the neutrino sector. With the SK detector observing the oscillated neutrino flux, the T2K experiment observed the first hints of a non-zero $\sin^2(\theta_{13})$ measurement and continues to lead the field with the constraints it provides on $\sin^2(\theta_{13})$, $\sin^2(\theta_{23})$, Δm_{23}^2 and δ_{CP} . **section 2.2 documents the The** techniques which T2K uses in generating its neutrino beam as well as the near-detector used to constrain the flux and cross-section parameters **invoked within the systematic models used in this analysis are documented in section 2.2.**

⁴⁵³ 2.1 The Super-Kamiokande Experiment

⁴⁵⁴ The SK experiment began taking data in 1996 [79] and has had many modifications
⁴⁵⁵ throughout its lifespan. There have been seven defined periods of data taking as
⁴⁵⁶ noted in Table 2.1. Data taking began in SK-I which ran for five years. Between the
⁴⁵⁷ SK-I and SK-II periods, a significant proportion of the PMTs were damaged during
⁴⁵⁸ maintenance. Those that survived were equally distributed throughout the detector
⁴⁵⁹ in the SK-II era, which resulted in a reduced photo-coverage. From SK-III onwards,
⁴⁶⁰ repairs to the detector meant the full suite of PMTs was operational. Before the
⁴⁶¹ start of SK-IV, the data acquisition and electronic systems were upgraded. Between
⁴⁶² SK-IV and SK-V, a significant effort was placed into tank open maintenance and
⁴⁶³ repair/replacement of defective PMTs, a task for which the author of this thesis was
⁴⁶⁴ required. Consequently, the detector conditions were significantly different between
⁴⁶⁵ the two operational periods. SK-VI saw the start of the 0.01% gadolinium doped
⁴⁶⁶ water. SK-VII, which started during the writing of this thesis, has increased the
⁴⁶⁷ gadolinium concentration to 0.03% for continued operation. [DB: Link to Linyan's talk from Nu2022.](#)

Period	Start Date	End Date	Live-time (days)
I	April 1996	July 2001	1489.19
II	October 2002	October 2005	798.59
III	July 2006	September 2008	518.08
IV	September 2008	May 2018	3244.4
V	January 2019	July 2020	461.02
VI	July 2020	May 2022	583.3
VII	May 2022	Ongoing	N/A

Table 2.1: The various SK periods and respective live-time. The SK-VI live-time is calculated until 1st April 2022. SK-VII started during the writing of this thesis.

⁴⁶⁹ 2.1.1 The SK Detector

⁴⁷⁰ The basic structure of the Super-Kamiokande (SK) detector is a cylindrical tank with a
⁴⁷¹ diameter 39.3m and height 41.1m filled with ultrapure water [80]. A diagram of the
⁴⁷² significant components of the SK detector is [illustrated given](#) in Figure 2.1. The SK
⁴⁷³ detector is situated in the Kamioka mine in Gifu, Japan. The mine is underground with
⁴⁷⁴ roughly 1km rock overburden (2.7km water equivalent overburden) [81]. At this depth,
⁴⁷⁵ the rate of cosmic ray muons is significantly decreased to a value of $\sim 2\text{Hz}$. The top of
⁴⁷⁶ the tank is covered with stainless steel which is designed as a working platform for
⁴⁷⁷ maintenance, calibration, and location for high voltage and data acquisition electronics.

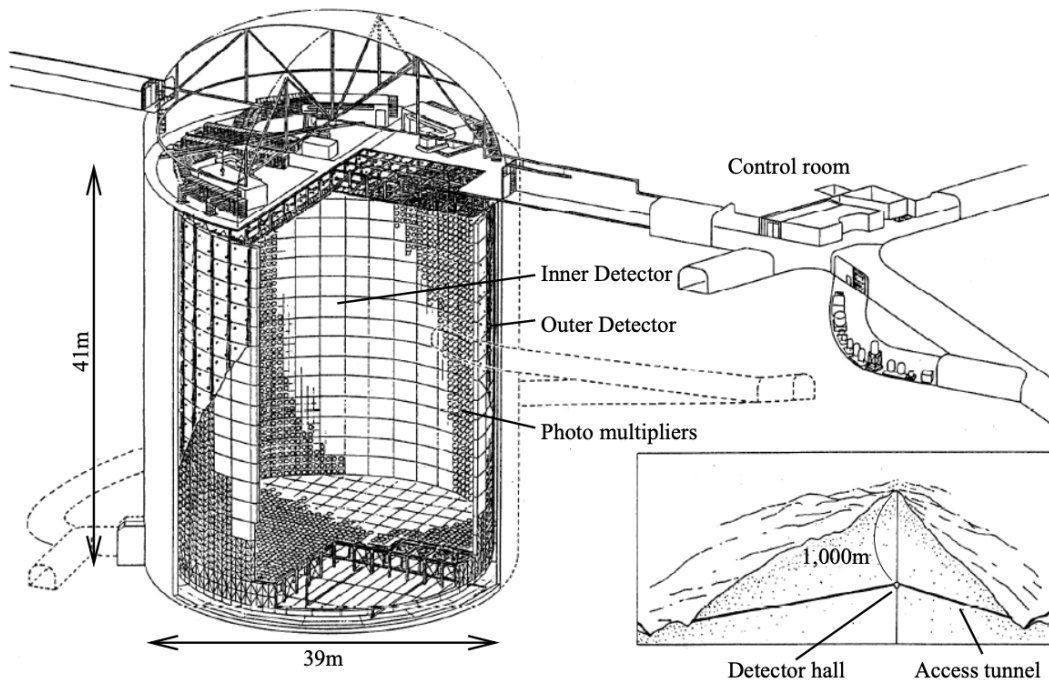


Figure 2.1: A schematic diagram of the Super-Kamiokande Detector. Taken from [82].

⁴⁷⁸ A smaller cylindrical structure (36.2m diameter, 33.8m height) is situated inside the
⁴⁷⁹ tank, with an approximate 2m gap between this structure and the outer tank wall. The
⁴⁸⁰ purpose of this structure is to support the photomultiplier tubes (PMTs). The volume
⁴⁸¹ inside and outside the support structure is referred to as the inner detector (ID) and

482 outer detector (OD), respectively. In the SK-IV era, the ID and OD are instrumented
483 by 11,129 50cm and 1,885 20cm PMTs respectively [80]. The ID contains a 32kton
484 mass of water. Many analyses performed at SK use a “fiducial volume” defined by the
485 volume of water inside the ID excluding some distance to the ID wall. This reduces the
486 volume of the detector which is sensitive to neutrino events but reduces radioactive
487 backgrounds and allows for better reconstruction performance. The nominal fiducial
488 volume is defined as the area contained inside 2m from the ID wall for a total of
489 22.5kton water [83].

490 The two regions of the detector (ID and OD) are optically separated with opaque
491 black plastic. The purpose of this is to determine whether a track entered or exited
492 the ID. This allows cosmic ray muons and partially contained events to be tagged and
493 separated from neutrino events entirely contained within the ID. This black plastic is
494 also used to cover the area between the ID PMTs to reduce photon reflection from the
495 ID walls. Opposite to this, the OD is lined with a reflective material to allow photons to
496 reflect around inside the OD until collected by one of the PMTs. Furthermore, each OD
497 PMT is backed with $50 \times 50\text{cm}$ plates of wavelength shifting acrylic which increases
498 the efficiency of light collection [81].

499 In the SK-IV data-taking period, the photocathode coverage of the detector, or the
500 fraction of the ID wall instrumented with PMTs, is $\sim 40\%$ [81]. The PMTs have a
501 quantum efficiency (the ratio of detected electrons to incident photons) of $\sim 21\%$ for
502 photons with wavelengths of $360\text{nm} < \lambda < 390\text{nm}$. The proportion of photoelectrons
503 that produce a signal in the dynode of a PMT, termed the collection efficiency, is
504 $> 70\%$ [81]. The PMTs used within SK are most sensitive to photons with wavelength
505 $300\text{nm} \leq \lambda \leq 600\text{nm}$ [81]. One disadvantage of using PMTs as the detection media
506 is that the Earth’s geomagnetic field can modify its response. Therefore, a set of

compensation coils is built around the inner surface of the detector to mitigate this effect [84].

As mentioned, the SK detector is filled with ultrapure water, which in a perfect world would contain no impurities. However, bacteria and organic compounds can significantly degrade the water quality. This decreases the attenuation length, which reduces the total number of photons that hit a PMT. To combat this, a sophisticated water treatment system has been developed [81, 85]. UV lights, mechanical filters, and membrane degasifiers are used to reduce the bacteria, suspended particulates, and radioactive materials from the water. The flow of water within the tank is also critical as it can remove stagnant bacterial growth or build-up of dust on the surfaces within the tank. Gravity drifts impurities in the water towards the bottom of the tank which, if left uncontrolled, can create asymmetric water conditions between the top and bottom of the tank. Typically, the water entering the tank is cooled below the ambient temperature of the tank to control convection and inhibit bacteria growth. Furthermore, the **rate of** dark noise hits within PMTs is sensitive to the PMT temperature [86] so controlling the temperature gradients within the tank is beneficial for stable measurements.

SK-VI is the first phase of the SK experiment to use gadolinium dopants within the ultrapure water [DB: Link to Linyan's talk at Nu2022](#). As such, the SK water system had to be replaced to avoid removing the gadolinium concentrate from the ultrapure water [87]. For an inverse β -decay (IBD) interaction in a water target, the emitted neutron is thermally captured on hydrogen. This process releases 2.2MeV γ rays which are difficult to detect **due to as the resulting** Compton scattered electrons **from a γ ray of this energy is are** very close to the Cherenkov threshold, limiting the number of photons produced. Thermal capture of neutrons on gadolinium generates γ rays with higher energy (**8MeV [69]**) meaning they are more easily detected. SK-VI has 0.01%

533 Gd loading (0.02% gadolinium sulphate by mass) which causes \approx 50% of neutrons
534 emitted by IBD to be captured on gadolinium [88,89]. Whilst predominantly useful
535 for low energy analyses, Gd loading allows better $\nu/\bar{\nu}$ separation for atmospheric
536 neutrino event selections [90]. Efforts are currently in place to increase the gadolinium
537 concentrate to 0.03% for \approx 75% neutron capture efficiency on gadolinium **DB: Link to**
538 **Mark's talk at Nu2022**. The final stage of loading targets 0.1% concentrate.

539 2.1.2 Calibration

540 The calibration of the SK detector is documented in [80] and summarised below. The
541 analysis presented within this thesis is dependent upon ‘high energy events’ (Charged
542 particles with $O(> 100)\text{MeV}$ momenta). These are events that are expected to generate
543 a larger number of photons such that each PMT will be hit with multiple photons.
544 The reconstruction of these events depends upon the charge deposited within each
545 PMT and the timing response of each individual PMT. Therefore, the most relevant
546 calibration techniques to this thesis are outlined.

547 Before installation, 420 PMTs were calibrated to have identical charge responses
548 and then distributed throughout the tank in a cross-shape pattern (As illustrated by
549 Figure 2.2). These are used as a standardised measure for the rest of the PMTs installed
550 at similar geometric positions within SK to be calibrated against. To perform this
551 calibration, a xenon lamp is located at the center of the SK tank which flashes uniform
552 light at 1Hz. This allows for geometrical effects, water quality variation, and timing
553 effects to be measured in-situ throughout normal data-taking periods.

554 When specifically performing calibration of the detector (in out-of-data taking
555 mode), the water in the tank was circulated to avoid top/bottom asymmetric water
556 quality. Any non-uniformity within the tank significantly affects the PMT hit proba-

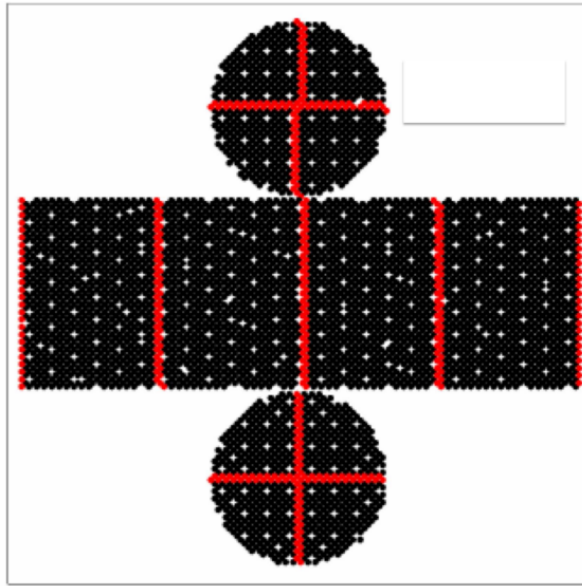


Figure 2.2: The location of “standard PMTs” (red) inside the SK detector. Taken from [80].

557 bility through scattering or absorption. This becomes a dominant effect for the very
 558 low-intensity light sources discussed later which are designed such that only one
 559 photon is incident upon a given PMT.

560 The “gain” of a PMT is defined as the ratio of the total charge of the signal produced
 561 compared to the charge of photoelectrons emitted by the photocathodes within the
 562 PMT. To calibrate the signal of each PMT, the “relative” and “absolute” gain values are
 563 measured. The relative gain is the variation of gain among each of the PMTs whereas
 564 the absolute gain is the average gain of all PMTs.

565 The relative gain is calibrated as follows. A laser is used to generate two measure-
 566 ments: a high-intensity flash that illuminates every PMT with a sufficient number of
 567 photons, and a low-intensity flash in which only a small number of PMTs collect light.
 568 The first measurement creates an average charge, $Q_{obs}(i)$ on PMT i , whereas the second
 569 measurement ensures that each hit PMT only generates a single photoelectron. For the
 570 low-intensity measurement, the number of times each PMT records a charge larger
 571 than 1/4 photoelectrons, $N_{obs}(i)$, is counted. The values measured can be expressed as

$$\begin{aligned} Q_{obs}(i) &\propto I_H \times f(i) \times \epsilon(i) \times G(i), \\ N_{obs}(i) &\propto I_L \times f(i) \times \epsilon(i), \end{aligned} \quad (2.1)$$

572 Where I_H and I_L is the intensity of the high and low flashes, $f(i)$ is the acceptance
 573 efficiency of the i^{th} PMT, $\epsilon(i)$ is the product of the quantum and collection efficiency
 574 of the i^{th} PMT and $G(i)$ is the gain of the i^{th} PMT. The relative gain for each PMT can
 575 determined by taking the ratio of these quantities.

576 The absolute gain calibration is performed by observing fixed energy γ -rays of
 577 $E_\gamma \sim 9\text{MeV}$ emitted isotropically from neutron capture on a NiCf source situated at
 578 the center of the detector. This generates a photon yield of about 0.004 photoelec-
 579 trons/PMT/event, meaning that $> 99\%$ of PMT signals are generated from single
 580 photoelectrons. A charge distribution is generated by performing this calibration over
 581 all PMTs, and the average value of this distribution is taken to be the absolute gain
 582 value.

583 As mentioned in subsection 2.1.1, the average quantum and collection efficiency
 584 for the SK detector is $\sim 21\%$ and $> 70\%$ respectively. However, these values do differ
 585 between each PMT and need to be calibrated accordingly. Consequently, the NiCf
 586 source is also used to calibrate the “quantum \times collection” efficiency (denoted “QE”)
 587 value of each PMT. The NiCf low-intensity source is used as the PMT hit probability
 588 is proportional to the QE ($N_{obs}(i) \propto \epsilon(i)$ in Equation 2.1). A Monte Carlo prediction
 589 which includes photon absorption, scattering, and reflection is made to estimate the
 590 number of photons incident on each PMT and the ratio of the number of predicted
 591 to observed hits is calculated. The difference is attributed to the QE efficiency of that
 592 PMT. This technique is extended to calculate the relative QE efficiency by normalizing
 593 the average of all PMTs which removes the dependence on the light intensity.

594 Due to differing cable lengths and readout electronics, the timing response between
595 a photon hitting the PMT and the signal being captured by the data acquisition can be
596 different between each PMT. Due to threshold triggers (Described in subsection 2.1.3),
597 the time at which a pulse reaches a threshold is dependent upon the size of the pulse.
598 This is known as the ‘time-walk’ effect and also needs to be accounted for in each PMT.
599 To calibrate the timing response, a pulse of light with width 0.2ns is emitted into the
600 detector through a diffuser. Two-dimensional distributions of time and pulse height
601 (or charge) are made for each PMT and are used to calibrate the timing response. This
602 is performed in-situ **whilst during** data taking with the light source pulsing at 0.03Hz.

603 The top/bottom water quality asymmetry is measured using the NiCf calibration
604 data and cross-referencing these results to the “standard PMTs”. The water attenuation
605 length is continuously measured by the rate of vertically-downgoing cosmic-ray
606 muons which enter via the top of the tank.

607 2.1.3 Data Acquisition and Triggering

608 Dark noise is the phenomenon where a PMT registers a pulse that is consistent with a
609 single photoelectron emitted from photon detection despite the PMT being in complete
610 darkness. This is predominately caused by two processes. Firstly there is intrinsic
611 dark noise which is where photoelectrons gain enough thermal energy to be emitted
612 from the photocathode, and secondly, the radioactive decay of contaminants inside the
613 structure of the PMT. Typical dark noise rate for PMTs used within SK are $O(3)$ kHz
614 [81] **which equates to about 12 dark noise hits per 220ns**. This is lower than the
615 expected number of photons generated for a ‘high energy event’ (As described in
616 subsection 2.1.4) but instability in this value can cause biases in reconstruction.

617 The analysis presented in this thesis only uses the SK-IV period of the SK exper-
 618 iment so this subsection focuses on the relevant points of the data acquisition and
 619 triggering systems to that SK period. The earlier data acquisition and triggering
 620 systems are documented in [91, 92].

621 Before the SK-IV period started, the existing front-end electronics were replaced

622 with “QTC-Based Electrons with Ethernet, QBEE” systems [93]. When the QBEE
 623 observes a signal above a 1/4 photoelectron threshold, the charge-to-time (QTC)

624 converter generates a rectangular pulse. The start of the rectangular pulse indicates

625 the time at which the analog photoelectron signal was received and the width of the

626 pulse indicates the total charge integrated throughout the signal. This is then digitized

627 by time-to-digital converters and sent to the “front-end” PCs. The digitized signal

628 from every QBEE is then chronologically ordered and sent to the “merger” PCs. It is

629 the merger PCs that apply the software trigger. Any triggered events are passed to the

630 “organizer” PC. This sorts the data stream of multiple merger PCs into chronologically

631 ordered events which are then saved to disk. The schematic of data flow from PMTs to

632 disk is illustrated in Figure 2.3.

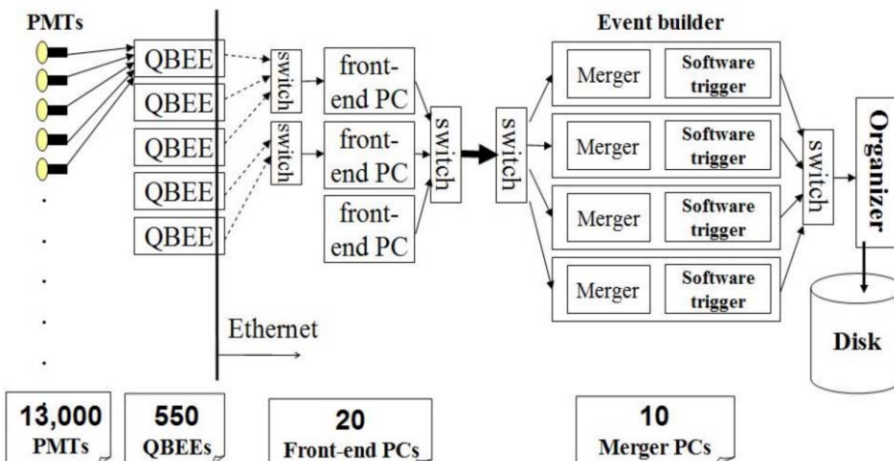


Figure 2.3: Schematic view of the data flow through the data acquisition and online system.
 Taken from [94].

The software trigger (described in [95]) operates by determining the number of PMT hits within a 200ns sliding window, $N_{200\mu s}$. This window coincides with the maximum time that a Cherenkov photon would take to traverse the length of the SK tank [92]. For lower energy events that generate fewer photons, this technique is useful for eliminating background processes like dark noise and radioactive decay which would be expected to separate in time. When the value of $N_{200\mu s}$ exceeds some threshold, a software trigger is issued. There are several trigger thresholds used within the SK-IV period which are detailed in Table 2.2. If one of these thresholds is met, the PMT hits within an extended time window are also read out and saved to disk. In the special case of an event that exceeds the SHE trigger but does not exceed the OD trigger, the AFT trigger looks for delayed coincidences of 2.2MeV gamma rays emitted from neutron capture in a $535\mu s$ window after the SHE trigger. A similar but more complex “Wideband Intelligent Trigger (WIT)” has been deployed and is described in [96].

Trigger	Acronym	Condition	Extended time window (μs)
Super Low Energy	SLE	>34/31 hits	1.3
Low Energy	LE	>47 hits	40
High Energy	HE	>50 hits	40
Super High Energy	SHE	>70/58 hits	40
Outer Detector	OD	>22 hits in OD	N/A

Table 2.2: The trigger thresholds and extended time windows saved around an event which were utilised throughout the SK-IV period. The exact thresholds can change and the values listed here represent the thresholds at the start and end of the SK-IV period.

2.1.4 Cherenkov Radiation

Cherenkov light is emitted from any highly energetic charged particle traveling with relativistic velocity, β , greater than the local speed of light in a medium [97]. Cherenkov light is formed at the surface of a cone with characteristic pitch angle,

$$\cos(\theta) = \frac{1}{\beta n}. \quad (2.2)$$

651 where n is the refractive index of the medium. Consequently, the Cherenkov
 652 momentum threshold, P_{thres} , is dependent upon the mass, m , of the charged particle
 653 moving through the **media medium**,

$$P_{thres} = \frac{m}{\sqrt{n^2 - 1}} \quad (2.3)$$

654 For water, where $n = 1.33$, the Cherenkov threshold momentum and energy for
 655 various particles are given in Table 2.3. In contrast, γ -rays are detected indirectly via
 656 the combination of photons generated by Compton scattering and pair production.
 657 The threshold for detection in the SK detector is typically higher than the threshold
 658 for photon production. This is due to the fact that the attenuation of photons in the
 659 water means that typically $\sim 75\%$ of Cherenkov photons reach the ID PMTs. Then the
 660 collection and quantum efficiencies described in subsection 2.1.1 result in the number
 661 of detected photons being lower than the number of photons which reach the PMTs.

Particle	Threshold Momentum (MeV)	Threshold Energy (MeV)
Electron	0.5828	0.7751
Muon	120.5	160.3
Pion	159.2	211.7
Proton	1070.0	1423.1

Table 2.3: The threshold momentum and energy for a particle to generate Cherenkov light in ultrapure water, as calculated in Equation 2.2 in ultrapure water which has refractive index $n = 1.33$.

The Frank-Tamm equation [98] describes the relationship between the number of Cherenkov photons generated per unit length, dN/dx , the wavelength of the photons generated, λ , and the relativistic velocity of the charged particle,

$$\frac{d^2N}{dxd\lambda} = 2\pi\alpha \left(1 - \frac{1}{n^2\beta^2}\right) \frac{1}{\lambda^2}. \quad (2.4)$$

where α is the fine structure constant. For a 100MeV momentum electron, approximately 330 photons will be produced per centimeter in the $300\text{nm} \leq \lambda \leq 700\text{nm}$ region which the ID PMTs are most sensitive to [81].

2.2 The Tokai to Kamioka Experiment

The Tokai to Kamioka (T2K) experiment is a long-baseline neutrino oscillation experiment located in Japan. Proposed in the early 2000s [99, 100] to replace K2K [101], T2K was designed to observe electron neutrino appearance whilst precisely measuring the oscillation parameters associated with muon neutrino disappearance [102]. The experiment consists of a neutrino beam generated at the Japan Proton Accelerator Research Complex (J-PARC), a suite of near detectors situated 280m from the beam target, and the Super Kamiokande far detector positioned at a 295km baseline. The cross-section view of the T2K experiment is drawn in Figure 2.4.

The T2K collaboration makes world-leading measurements of the $\sin^2(\theta_{23})$, Δm_{23}^2 , and δ_{CP} oscillation parameters. Improvements in the precision and accuracy of parameter estimates are still being made by including new data samples and developing the models which describe the neutrino interactions and detector responses DB: [Link to Christophe's slides from Nu2022](#). Electron neutrino appearance was first observed

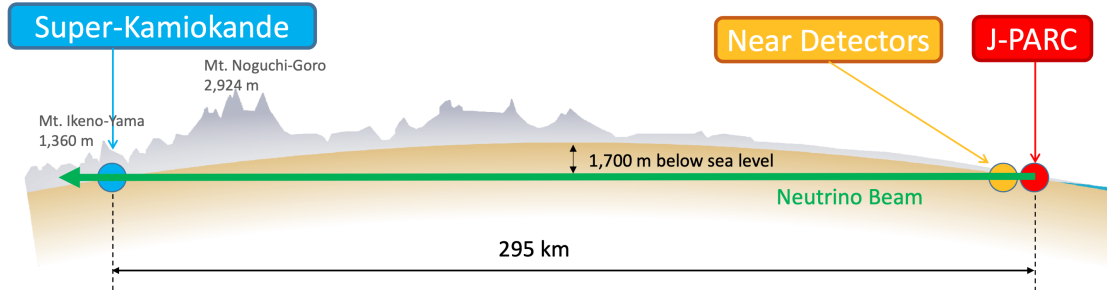


Figure 2.4: The cross-section view of the Tokai to Kamioka experiment illustrating the beam generation facility at J-PARC, the near detector situated at a baseline of 280m and the Super Kamiokande far detector situated 295km from the beam target.

682 at T2K in 2014 [103] ~~which accompanied a 7.3σ significance of a non-zero $\sin^2(\theta_{13})$~~
 683 **measurement with 7.3σ significance.**

684 The near detectors provide constraints on the beam flux and cross-section model
 685 parameters used within the **fit oscillation analysis** by observing the unoscillated
 686 neutrino beam. There are a host of detectors situated in the near detector hall (As
 687 illustrated in Figure 2.5): ND280 (subsection 2.2.2), INGRID (subsection 2.2.3), NINJA
 688 [104], WAGASCI [105], and Baby-MIND [106]. The latter three are not currently used
 689 within the oscillation analysis presented within this thesis.

690 Whilst this thesis presents the ND280 in terms of its purpose for the oscillation
 691 analysis, the detector can also make many cross-section measurements at neutrino
 692 energies of $O(1)\text{GeV}$ for the different targets within the detector [107, 108]. These
 693 measurements are of equal importance as they can lead the way in determining the
 694 model parameters used in the interaction models for the future high-precision era of
 695 neutrino physics.

696 2.2.1 The Neutrino Beam

697 The neutrino beam used within the T2K experiment is described in [58, 109] and
 698 summarised below. The accelerating facility at J-PARC is composed of two sections; the

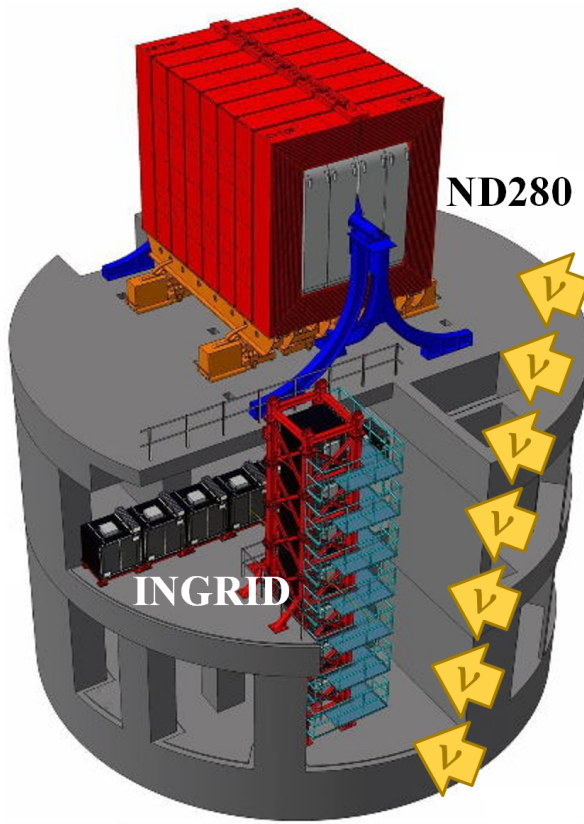
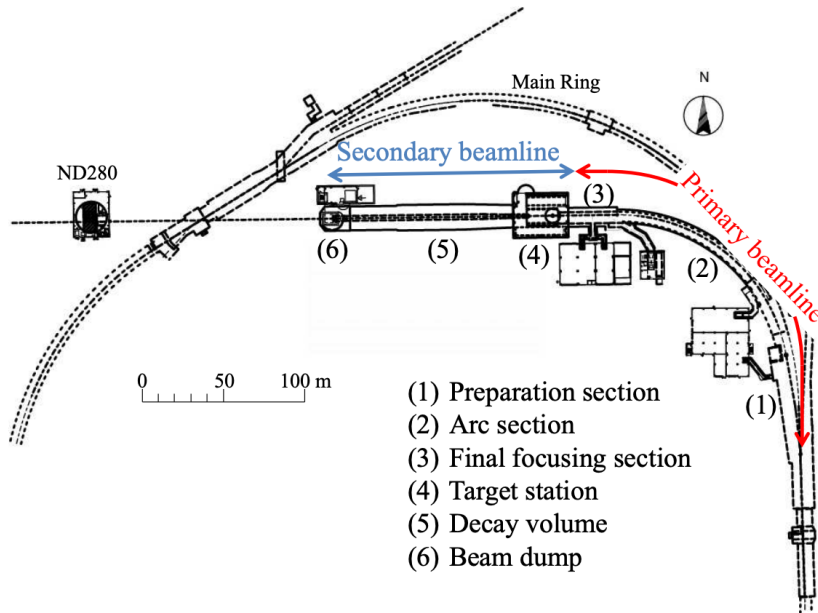


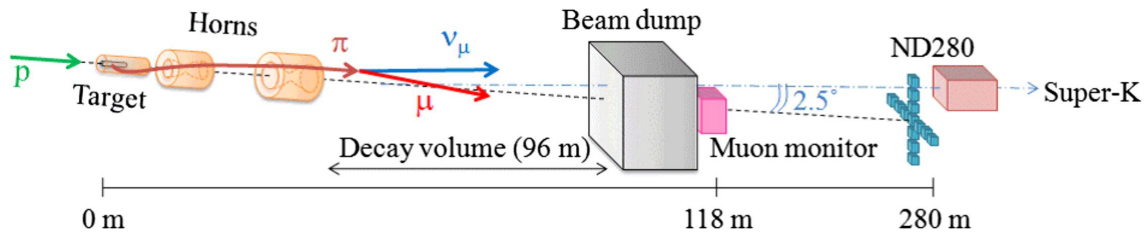
Figure 2.5: The near detector suite for the T2K experiment showing the ND280 and INGRID detectors. The distance between the detectors and the beam target is 280m.

699 primary and secondary beamlines. Figure 2.6 illustrates a schematic of the beamline,
 700 focusing mostly on the components of the secondary beamline. The primary beamline
 701 has three accelerators that progressively accelerate protons; a linear accelerator, a rapid-
 702 cycling synchrotron, and the main-ring (MR) synchrotron. Once fully accelerated by
 703 the MR, the protons have a kinetic energy of 30GeV. Eight bunches of these protons,
 704 separated by 500ns, are extracted per “spill” from the MR and directed towards a
 705 graphite target (a rod of length 91.4cm and diameter 2.6cm). Spills are extracted at
 706 0.5Hz with $\sim 3 \times 10^{14}$ protons contained per spill.

707 The secondary beamline consists of three main components: the target station, the
 708 decay volume, and the beam dump. The target station is comprised of the target, beam
 709 monitors, and three magnetic focusing horns. The proton beam interacts with the
 710 graphite target to form a secondary beam of mostly pions and kaons. The secondary



(a) Primary and secondary beamline



(b) Secondary beamline

Figure 2.6: Top panel: Bird's eye view of the most relevant part of primary and secondary beamline used within the T2K experiment. The primary beamline is the main-ring proton synchrotron, kicker magnet, and graphite target. The secondary beamline consists of the three focusing horns, decay volume, and beam dump. Figure taken from [109]. Bottom panel: The side-view of the secondary beamline including the focusing horns, beam dump and neutrino detectors. Figure taken from [110].

beam travels through a 96m long decay volume, generating neutrinos through the following decays [58],

$$\begin{aligned}
\pi^+ &\rightarrow \mu^+ + \nu_\mu & \pi^- &\rightarrow \mu^- + \bar{\nu}_\mu \\
K^+ &\rightarrow \mu^+ + \nu_\mu & K^- &\rightarrow \mu^- + \bar{\nu}_\mu \\
&\rightarrow \pi^0 + e^+ + \nu_e & &\rightarrow \pi^0 + e^- + \bar{\nu}_e \\
713 \quad &\rightarrow \pi^0 + \mu^+ + \nu_\mu & &\rightarrow \pi^0 + \mu^- + \bar{\nu}_\mu \\
K_L^0 &\rightarrow \pi^- + e^+ + \nu_e & K_L^0 &\rightarrow \pi^+ + e^- + \bar{\nu}_e \\
&\rightarrow \pi^- + \mu^+ + \nu_\mu & &\rightarrow \pi^+ + \mu^- + \bar{\nu}_\mu \\
\mu^+ &\rightarrow e^+ + \bar{\nu}_\mu + \nu_e & \mu^- &\rightarrow e^- + \nu_\mu + \bar{\nu}_e
\end{aligned}$$

714 The electrically charged component of the secondary beam is focused towards the
 715 far detector by the three magnetic horns. These horns direct charged particles of a
 716 particular polarity towards SK whilst defocusing the oppositely charged particles.
 717 This allows a mostly neutrino or mostly antineutrino beam to be used within the
 718 experiment, denoted as “forward horn current (FHC)” or “reverse horn current (RHC)”
 719 respectively.

720 Figure 2.7 illustrates the different contributions to the FHC and RHC neutrino flux.
 721 The low energy flux is dominated by the decay of pions whereas kaon decay becomes
 722 the dominant source of neutrinos for $E_\nu > 3\text{GeV}$. The “wrong-sign” component,
 723 which is the $\bar{\nu}_\mu$ background in a ν_μ beam, and the intrinsic irreducible ν_e background,
 724 are predominantly due to muon decay for $E_\nu < 2\text{GeV}$. As the antineutrino **production**
 725 cross-section is smaller than the neutrino cross-section, the wrong-sign component is
 726 more dominant in the RHC beam as compared to that in the FHC beam.

727 The beam dump, situated at the end of the decay volume, stops all charged particles
 728 other than highly energetic muons ($p_\mu > 5\text{GeV}$). The MuMon detector monitors the
 729 penetrating muons to determine the beam direction and intensity which is used to
 730 constrain some of the beam flux systematics within the analysis [110, 112].

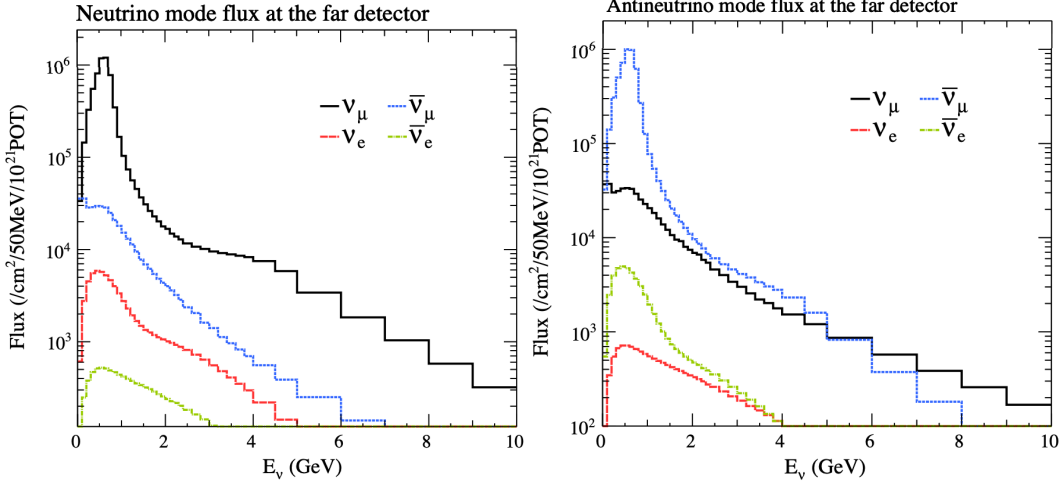


Figure 2.7: The Monte Carlo prediction of the energy spectrum for each flavour of neutrino (ν_e , $\bar{\nu}_e$, ν_μ and $\bar{\nu}_\mu$) in the neutrino dominated beam FHC mode (Left) and antineutrino dominated beam RHC mode (Right) expected at SK. Taken from [111].

The T2K experiment uses an off-axis beam to narrow the neutrino energy distribution.

This was the first implementation of this technique in a long-baseline neutrino oscillation experiment after its original proposal [113]. Pion decay, $\pi \rightarrow \mu + \nu_\mu$, is a two-body decay. Consequently, the neutrino energy, E_ν , can be determined based on the pion energy, E_π , and the angle at which the neutrino is emitted, θ ,

$$E_\nu = \frac{m_\pi^2 - m_\mu^2}{2(E_\pi - p_\pi \cos(\theta))}, \quad (2.5)$$

where m_π and m_μ are the mass of the pion and muon respectively. For a fixed

energy pion, the neutrino energy distribution is dependent upon the angle at which the neutrinos are observed from the initial pion beam direction. For the 295km baseline at T2K, $E_\nu = 0.6\text{GeV}$ maximises the electron neutrino appearance probability, $P(\nu_\mu \rightarrow \nu_e)$, whilst minimising the muon disappearance probability, $P(\nu_\mu \rightarrow \nu_\mu)$. Figure 2.8 illustrates the neutrino energy distribution for a range of off-axis angles, as well as the oscillation probabilities most relevant to T2K.

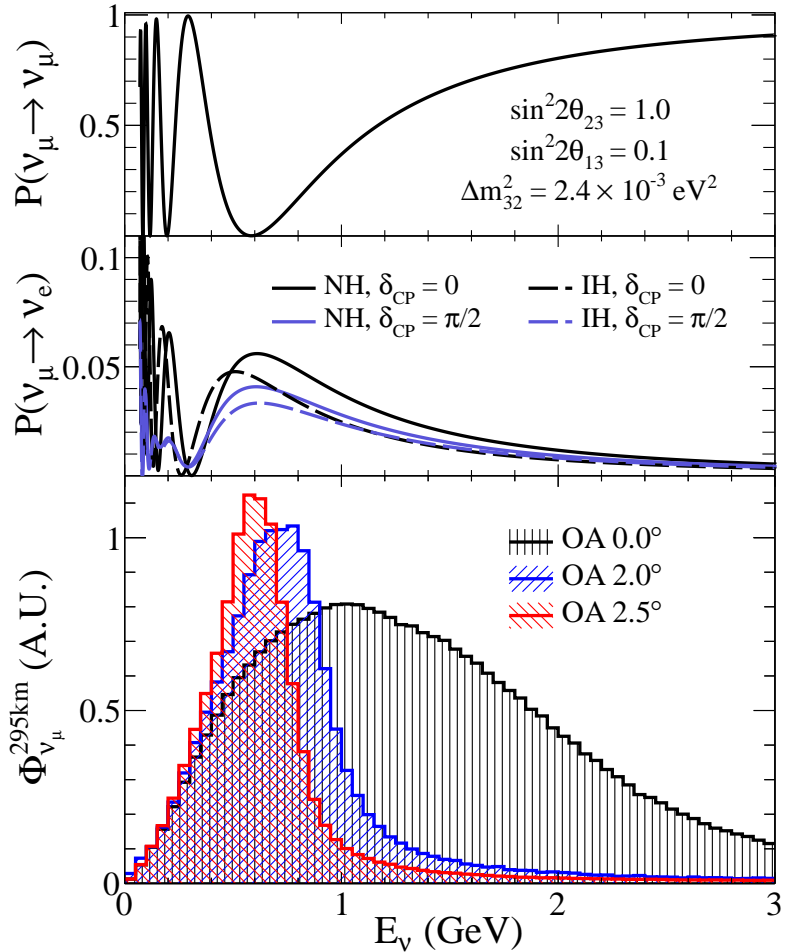


Figure 2.8: Top panel: T2K muon neutrino disappearance probability as a function of neutrino energy. Middle panel: T2K electron neutrino appearance probability as a function of neutrino energy. Bottom panel: The neutrino flux distribution for three different off-axis angles (Arbitrary units) as a function of neutrino energy.

743 2.2.2 The Near Detector at 280m

744 Whilst all the near detectors are situated in the same “pit” located at 280m from the
 745 beamline, the “ND280” detector is the off-axis detector which is situated at the same
 746 off-axis angle as the Super-Kamiokande far detector. It has two primary functions;
 747 firstly it measures the neutrino flux and secondly it counts the event rates of different
 748 types of neutrino interactions. Both of these constrain the flux and cross-section
 749 systematics invoked within the model for a more accurate prediction of the expected
 750 event rate at the far detector.

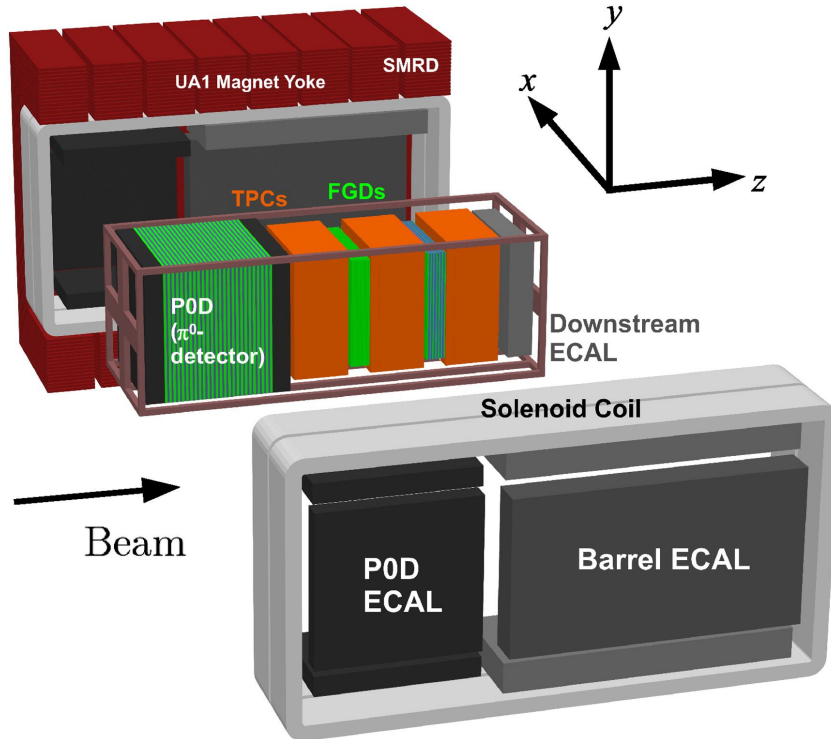


Figure 2.9: The components of the ND280 detector. The neutrino beam travels from left to right. Taken from [109].

As illustrated in Figure 2.9, the ND280 detector consists of several sub-detectors.

The most important part of the detector for this analysis is the tracker region. This is comprised of two time projection chambers (TPCs) sandwiched between three fine grain detectors (FGDs). The FGDs contain both hydrocarbon plastics and water targets for neutrino interactions and provide track reconstruction near the interaction vertex. The emitted charged particles can then propagate into the TPCs which provide particle identification and momentum reconstruction. The FGDs and TPCs are further described in subsubsection 2.2.2.1 and subsubsection 2.2.2.2 respectively. The electromagnetic calorimeter (ECAL) encapsulates the tracker region alongside the π^0 detector (P0D). The ECAL measures the deposited energy from photons emitted from interactions within the FGD. The P0D constrains the cross-section of neutral current interactions which generate neutral pions, which is one of the largest backgrounds in the electron neutrino appearance oscillation channel. The P0D and ECAL detectors are detailed in subsubsection 2.2.2.3 and subsubsection 2.2.2.4 respectively. The entire

765 detector is located within a large **yolk yoke** magnet which produces a 0.2T magnetic
766 field. This design of the magnet also includes a scintillating detector called the side
767 muon range detector (SMRD) which is used to track high-angle muons as well as
768 acting as a cosmic veto. The SMRD is described in subsubsection 2.2.2.5.

769 **2.2.2.1 Fine Grained Detectors**

770 The T2K tracker region is comprised of two fine grained detectors (FGD) and three
771 Time Projection Chambers (TPC). A detailed description of the FGD design, construc-
772 tion, and assembly is found in [114] and summarised below. The FGDs are the primary
773 target for neutrino interactions with a mass of 1.1 tonnes per FGD. Alongside this,
774 the FGDs are designed to be able to track short-range particles which do not exit the
775 FGD. Typically, short-range particles are low momentum and are observed as tracks
776 that deposit a large amount of energy per unit length. This means the FGD needs
777 good granularity to resolve these particles. The FGDs have the best timing resolution
778 ($\sim 3\text{ns}$) of any of the sub-detectors of the ND280 detector. As such, the FGDs are
779 used for time of flight measurements to determine forward going positively charged
780 particles from backward going negatively charged particles. Finally, any tracks which
781 pass through multiple sub-detectors are required to be track matched to the FGD.

782 Both FDGs are made from square scintillator planes of side length 186cm and width
783 2.02cm. Each plane consists of two layers of 192 scintillator bars in an XY orientation.
784 A wave-length shift fiber is threaded through the center of each bar and is read out by
785 a multi-photon pixel counter (MPPC). FGD1 is the most upstream of the two FGDs
786 and contains 15 planes of carbon plastic scintillator which is a common target in
787 external neutrino scattering data. As the far detector is a pure water target, 7 of the 15
788 scintillator planes in FGD2 have been replaced with a hybrid water-scintillator target.
789 Due to the complexity of the nucleus, nuclear effects can not be extrapolated between

⁷⁹⁰ different nuclei. Therefore having the ability to take data on one target which is the
⁷⁹¹ same as external data and another target which is the same as the far detector target is
⁷⁹² beneficial for reliable model parameter estimates.

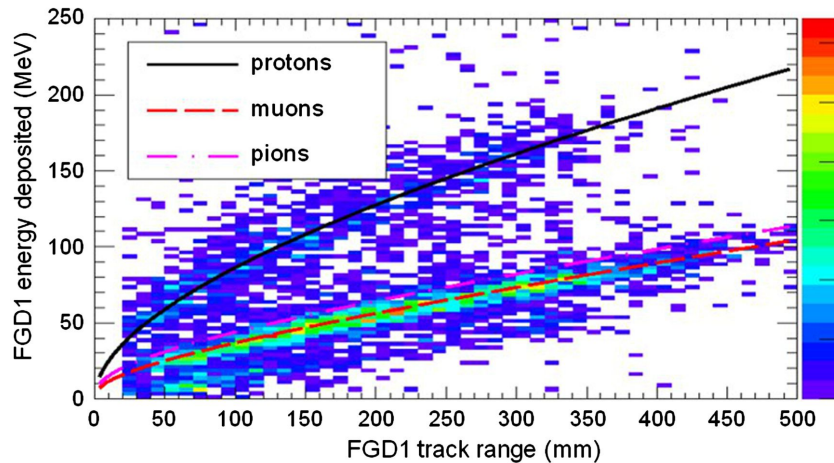


Figure 2.10: Comparison of data to Monte Carlo prediction of integrated deposited energy as a function of track length for particles that stopped in FGD1. Taken from [114].

⁷⁹³ The integrated deposited energy is used for particle identification. The FGD
⁷⁹⁴ can distinguish protons from other charged particles by comparing the integrated
⁷⁹⁵ deposited energy from data to Monte Carlo prediction as seen in Figure 2.10.

⁷⁹⁶ 2.2.2.2 Time Projection Chambers

⁷⁹⁷ The majority of particle identification and momentum measurements within ND280
⁷⁹⁸ are provided by three Time Projection Chambers (TPCs) [115]. The TPCs are located
⁷⁹⁹ on either side of the FGDs. They are located inside of the magnetic field meaning the
⁸⁰⁰ momentum of a charged particle can be determined from the bending of the track.

⁸⁰¹ Each TPC module consists of two gas-tight boxes, as shown in Figure 2.11, which
⁸⁰² are made of non-magnetic material. The outer box is filled with CO₂ which acts as
⁸⁰³ an electrical insulator between the inner box and the ground. The inner box forms
⁸⁰⁴ the field cage which produces a uniform electric drift field of $\sim 275\text{V}/\text{cm}$ and an

805 argon gas mixture. Charged particles moving through this gas mixture ionize the gas
 806 mixture. The ionised charge is drifted towards micromega detectors which measure
 807 the ionization charge. The time and position information in the readout allows a
 808 three-dimensional image of the neutrino interaction.

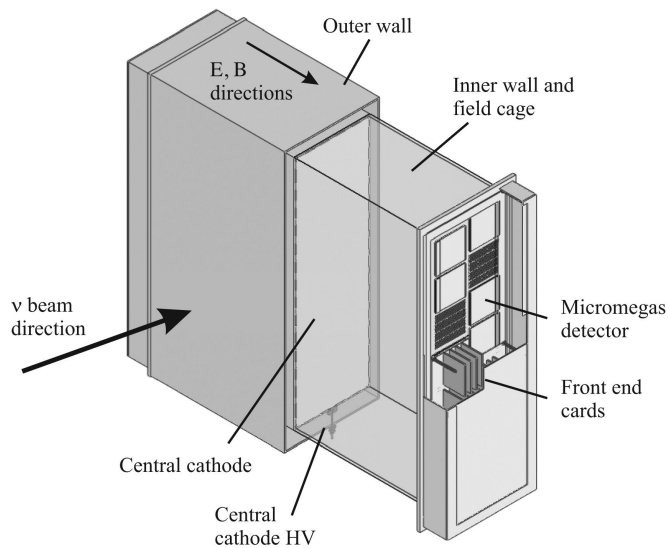


Figure 2.11: Schematic design of a Time Projection Chamber detector. Taken from [115].

809 The particle identification of tracks that pass through the TPCs is performed using
 810 dE/dx measurements. Figure 2.12 illustrates the data to Monte Carlo distributions
 811 of the energy lost by a charged particle passing through the TPC as a function of the
 812 reconstructed particle momentum. The resolution is $7.8 \pm 0.2\%$ meaning that electrons
 813 and muons can be distinguished. This allows reliable measurements of the intrinsic ν_e
 814 component of the beam.

815 2.2.2.3 π^0 Detector

816 If one of the γ -rays from a $\pi^0 \rightarrow 2\gamma$ decay is missed at the far detector, the reconstruc-
 817 tion will determine that event to be electron-like. This is one of the main backgrounds
 818 hindering the electron neutrino appearance searches. Therefore, the π^0 detector (P0D)

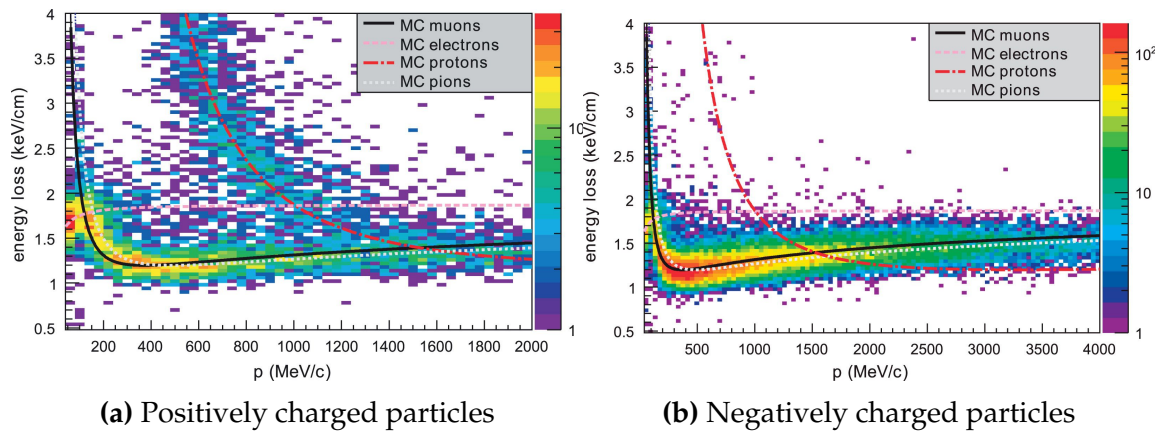


Figure 2.12: The distribution of energy loss as a function of reconstructed momentum for charged particles passing through the TPC, comparing data to Monte Carlo prediction. Taken from [115].

measures the cross-section of the neutral current induced neutral pion production on a water target.

The P0D is a cube of approximately 2.5m length. The P0D consists of layers of scintillating bars, brass and lead sheets, and water bags as illustrated in Figure 2.13. Two electromagnetic calorimeters are positioned at the most upstream and most downstream position in the sub-detector and the water target is situated in between them. The scintillator layers are built from two triangular bars orientated in opposite directions to form a rectangular layer. Each triangular scintillator bar is threaded with optical fiber which is read out by MPPCs. The high-Z brass and lead regions produce electron showers from the photons emitted in π^0 decay.

The sub-detector can generate measurements of NC1 π^0 cross-sections on a water target by measuring the event rate both with and without the water target, with the cross-section on a water target being determined as the difference. The total active mass is 16.1 tonnes when filled with water and 13.3 tonnes when empty.

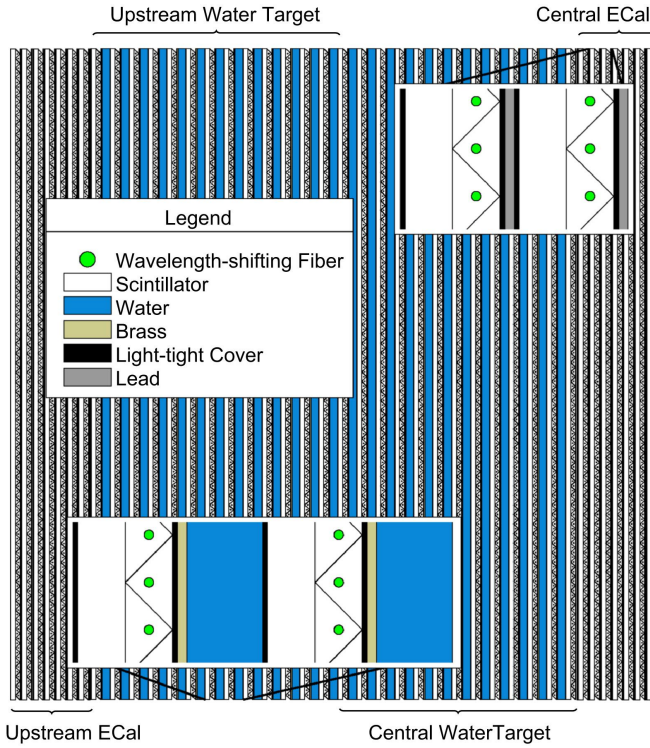


Figure 2.13: A schematic of the P0D side-view. Taken from [116].

833 2.2.2.4 Electromagnetic Calorimeter

834 The electromagnetic calorimeter [117] (ECal) encapsulates the P0D and tracking sub-
 835 detectors. Its primary purpose is to aid π^0 reconstruction from any interaction in
 836 the tracker. To do this, it measures the energy and direction of photon showers from
 837 $\pi^0 \rightarrow 2\gamma$ decay. It can also distinguish pion and muon tracks depending on the shape
 838 of the photon shower deposited.

839 The ECal is comprised of three sections; the P0D ECal which surrounds the P0D,
 840 the barrel ECal which encompasses the tracking region, and the downstream ECal
 841 which is situated downstream of the tracker region. The barrel and downstream
 842 ECals are tracking calorimeters that focus on electromagnetic showers from high-angle
 843 particles emitted from the tracking sub-detectors. Particularly in the TPC, high-angle
 844 tracks (those which travel perpendicularly to the beam-axis) can travel along a single
 845 scintillator bar resulting in very few hits. The width of the barrel and downstream

⁸⁴⁶ ECal corresponds to ~ 11 electron radiation lengths to ensure $\sim 50\%$ of the energy of
⁸⁴⁷ the π^0 is contained. As the P0D has its own calorimetry which reconstructs showers,
⁸⁴⁸ the P0D ECal determines the energy which escapes the P0D.

⁸⁴⁹ Each ECal is constructed of multiple layers of scintillating bars sandwiched between
⁸⁵⁰ lead sheets. The scintillating bars are threaded with optical fiber and read out by
⁸⁵¹ MPPCs. Each sequential layer of the scintillator is orientated perpendicular to the
⁸⁵² previous which allows a two-dimensional readout, which when temporal, information
⁸⁵³ is included results in three-dimension event displays. The target mass of the P0D ECal,
⁸⁵⁴ barrel ECal, and downstream ECal are 1.50, 4.80 and 6.62 tonnes respectively.

⁸⁵⁵ 2.2.2.5 Side Muon Range Detector

⁸⁵⁶ As illustrated in Figure 2.9, the ECal, FGDs, P0D, and TPCs are enclosed within the
⁸⁵⁷ UA1 magnet. Originally designed for the NOMAD [118] experiment and reconditioned
⁸⁵⁸ for use in the T2K experiment [119], the UA1 magnet provides a uniform horizontal
⁸⁵⁹ magnetic field of $0.2 \pm 2 \times 10^{-4}$ T.

⁸⁶⁰ Built into the UA1 magnet, the side muon range detector (SMRD) [120] monitors
⁸⁶¹ high-energy muons which leave the tracking region and permeate through the ECal.
⁸⁶² It additionally acts as a cosmic muon veto and trigger.

⁸⁶³ 2.2.3 The Interactive Neutrino GRID

⁸⁶⁴ The Interactive Neutrino GRID (INGRID) detector is situated within the same “pit” as
⁸⁶⁵ the other near detectors. It is aligned with the beam in the “on-axis” position and mea-
⁸⁶⁶ sures the beam direction, spread, and intensity. The detector was originally designed
⁸⁶⁷ with 16 identical modules [109] (two modules have since been decommissioned) and a

868 “proton” module. The design of the detector is cross-shaped with length and height
869 $10\text{m} \times 10\text{m}$ as illustrated in Figure 2.14.

870 Each module is composed of iron sheets interlaced with eleven tracking scintillator
871 planes for a total target mass of 7.1 tonnes per module. The scintillator design is an X-Y
872 pattern of 24 bars in both orientations, where each bar contains wave-length shifting
873 fibers which are connected to multi-pixel photon counters (MPPCs). The MPPCs
874 convert detected photons into electrical signals via photodiodes. This is then read
875 out by Trip-T front-end electronics [121] and passed to the readout merging modules
876 along with timing information from the clock module. Each module is encapsulated
877 inside veto planes to aid the rejection of charged particles entering the module.

878 The proton module is different from the other modules in that it consists of entirely
879 scintillator planes with no iron target. The scintillator bars are also smaller than those
880 used in the other modules to increase the granularity of the detector and improve
881 tracking capabilities. The module sits in the center of the beamline and is designed to
882 give precise measurements of quasi-elastic charged current interactions to evaluate
883 the performance of the Monte Carlo simulation of the beamline.

884 The INGRID detector can measure the beam direction to an uncertainty of 0.4mrad
885 and the beam center within a resolution of 10cm [109]. The beam direction in both the
886 vertical and horizontal directions is discussed in [122] and it is found to be in good
887 agreement with the MUMON monitor described in subsection 2.2.1.

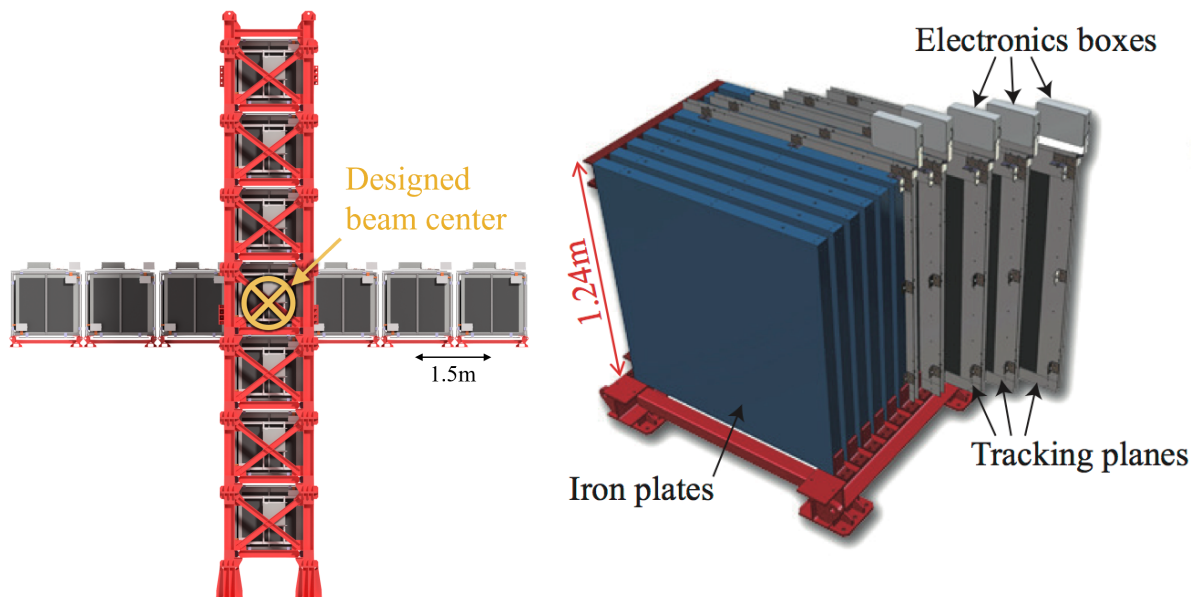


Figure 2.14: Left panel: The Interactive Neutrino GRID on-axis Detector. 14 modules are arranged in a cross-shape configuration, with the center modules being directly aligned with the on-axis beam. Right panel: The layout of a single module of the INGRID detector. Both figures are recreated from [109].

888 **Chapter 3**

889 **Bayesian Statistics and Markov Chain**
890 **Monte Carlo Techniques**

891 The analysis throughout this thesis is based upon a Bayesian oscillation analysis. To
892 extract the oscillation parameters, a Markov Chain Monte Carlo (MCMC) method is
893 used. This chapter explains the theory of how parameter estimates can be determined
894 using this technique and condenses the material found in the literature [123–126].

895 The oscillation parameter determination presented within this thesis is built upon a
896 simultaneous fit to the near detector, far detector beam, and atmospheric neutrino data.
897 In total, there are four oscillation parameters of interest ($\sin^2(\theta_{23})$, $\sin^2(\theta_{13})$, Δm_{23}^2 ,
898 and δ_{CP}), two oscillation parameters to which this study will not be sensitive ($\sin^2(\theta_{12})$
899 , Δm_{12}^2) and many nuisance parameters that control the systematic uncertainty models
900 invoked within this study. The systematic uncertainties can be grouped into categories
901 depending on how they are defined; 574 bin-normalisations due to the near detector
902 response, 45 bin-normalisations to describe the far detector response to neutrino beam
903 events, 27 parameters to describe the detector response to atmospheric neutrino events,
904 100 to model the bin-normalisation due to beam flux uncertainties, 18 which model the
905 atmospheric flux uncertainties, and 87 to describe the correlated cross-section model.
906 An alternative parameterisation, where the far detector response is correlated between
907 the beam and atmospheric samples, replaces the bin-normalisation parameters with
908 224 shift and smear systematics. Section [DB: Link to Systematics Chapter](#) describes
909 the systematic model in more depth.

910 The MCMC technique generates a multi-dimensional probability distribution across
911 all of the model parameters used in the fit. To determine the parameter estimate of a
912 single parameter, this multi-dimensional object is integrated over all other parameters.
913 This process is called Marginalisation and is further described in subsection 3.3.1.
914 Monte Carlo techniques approximate the probability distribution of each parameter
915 within the limit of generating infinite samples. As ever, generating a large number of
916 samples is time and resource-dependent. Therefore, an MCMC technique is utilised
917 within this analysis to reduce the required number of steps to sufficiently sample the
918 parameter space. This technique is described in further detail in subsection 3.2.1.

919 3.1 Bayesian Statistics

920 According to Bayesian Inference, observables and parameters of a statistical model are
921 treated on an equal footing. To estimate model parameters $\vec{\theta}$ from some data D , one
922 needs to define the joint probability distribution $P(D|\vec{\theta})$ which can be described as the
923 prior distribution for model parameters $P(\vec{\theta})$ and the likelihood of the data given the
924 model parameters $P(D|\vec{\theta})$,

$$P(D, \vec{\theta}) = P(D|\vec{\theta})P(\vec{\theta}). \quad (3.1)$$

925 The prior distribution, $P(\vec{\theta})$, describes all previous knowledge about the parameters
926 within the model. For example, if the risk of developing health problems is known
927 to increase with age, the prior distribution would describe the increase. For the
928 purpose of this analysis, the prior distribution is typically the best-fit values taken
929 from external data measurements with a Gaussian uncertainty. The prior distribution

can also contain correlations between model parameters. In an analysis using Monte Carlo techniques, the likelihood of measuring some data assuming some set of model parameters is calculated by comparing the Monte Carlo prediction generated at that particular set of model parameters to the data.

It is parameter estimation that is important for this analysis and as such, we apply Bayes' theorem [127]. To calculate the probability for each parameter to have a certain value given the observed data $P(\vec{\theta}|D)$, known as the posterior distribution (often termed the posterior). This can be expressed as

$$P(\vec{\theta}|D) = \frac{P(D|\vec{\theta})P(\vec{\theta})}{\int P(D|\vec{\theta})P(\vec{\theta})d\vec{\theta}}. \quad (3.2)$$

The denominator in Equation 3.2 is the integral of the joint probability distribution over all values of all parameters used within the fit. For brevity, we say that the posterior distribution is

$$P(\vec{\theta}|D)\alpha P(D|\vec{\theta})P(\vec{\theta}). \quad (3.3)$$

In subsection 3.3.1, we see that for the cases used within this analysis, it is reasonable to know the posterior to some normalisation constant.

3.2 Monte Carlo Simulation

Monte Carlo techniques are used to numerically solve a complex problem that does not necessarily have an analytical solution. These techniques rely on building a large

946 ensemble of samples from an unknown distribution and then using the ensemble to
947 approximate the properties of the distribution.

948 An example that uses Monte Carlo techniques is to calculate the area underneath
949 a curve. For example, take the problem of calculating the area under a straight line
950 with gradient $M = 0.4$ and intercept $C = 1.0$. Analytically, one can calculate the area
951 under the line is equal to 30 units for $0 \leq x \leq 10$. Using Monte Carlo techniques,
952 one can calculate the area under this line by throwing many random values for the x
953 and y components of each sample and then calculating whether that point falls below
954 the line. The area can then be calculated by the ratio of points below the line to the
955 total number of samples thrown multiplied by the total area in which samples were
956 scattered. The study is shown in Figure 3.1 highlights this technique and finds the area
957 under the curve to be 29.9 compared to an analytical solution of 30.0. The deviation
958 of the numerical to analytical solution can be attributed to the number of samples
959 used in the study. The accuracy of the approximation in which the properties of the
960 Monte Carlo samples replicate those of the desired distribution is dependent on the
961 number of samples used. Replicating this study with a differing number of Monte
962 Carlo samples used in each study (As shown in Figure 3.2) highlights how the Monte
963 Carlo techniques are only accurate within the limit of a high number of samples.

964 Whilst the above example has an analytical solution, these techniques are just as
965 applicable to complex solutions. Clearly, any numerical solution is only as useful as its
966 efficiency. As discussed, the accuracy of the Monte Carlo technique is dependent upon
967 the number of samples generated to approximate the properties of the distribution.
968 Furthermore, if the positions at which the samples are evaluated are not 'cleverly'
969 picked, the efficiency of the Monte Carlo technique significantly drops. Given the
970 example in Figure 3.1, if the region in which the samples are scattered significantly
971 extends passed the region of interest, many calculations will be calculated but do

not add to the ability of the Monte Carlo technique to achieve the correct result. For instance, any sample evaluated at a $y \geq 5$ could be removed without affecting the final result. This does bring in an aspect of the ‘chicken and egg’ problem in that to achieve efficient sampling, one needs to know the distribution beforehand.

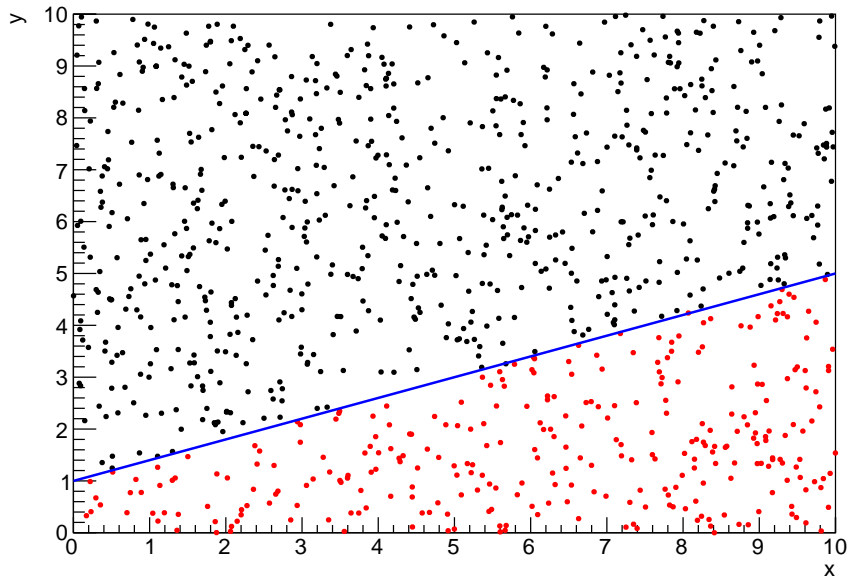


Figure 3.1: Example of using Monte Carlo techniques to find the area under the blue line. The gradient and intercept of the line are 0.4 and 1.0 respectively. The area found to be under the curve using one thousand samples is 29.9 units.

3.2.1 Markov Chain Monte Carlo

This analysis utilises a multi-dimensional probability distribution, with some dimensions being significantly more constrained than others. This could be from prior knowledge of parameter distributions from external data or un-physical regions in which parameters can not exist. Consequently, the Monte Carlo techniques used need to be as efficient as possible. For this analysis, the Markov Chain Monte Carlo (MCMC) technique is chosen. An MCMC technique is a Monte Carlo technique that uses a Markov chain to select which points at which to sample the parameter distribution.

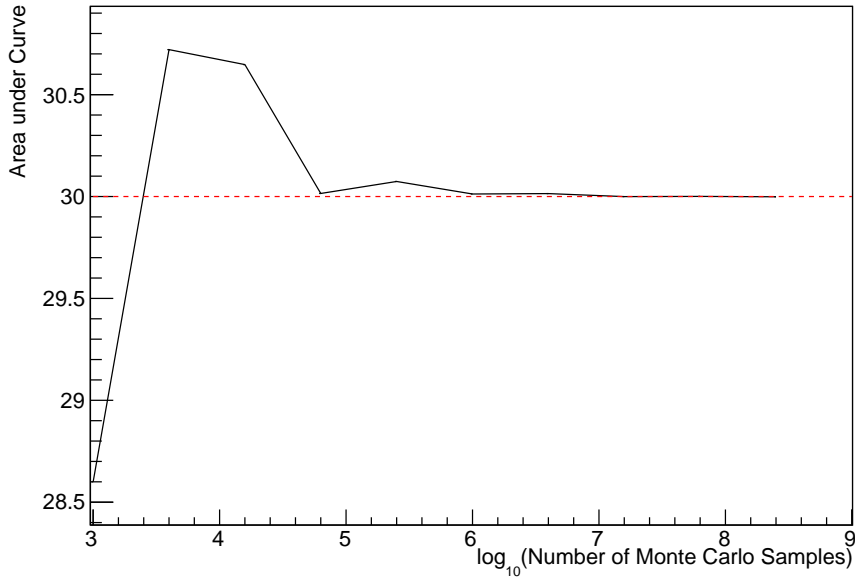


Figure 3.2: The area under a line of gradient 0.4 and intercept 1.0 for the range $0 \leq x \leq 10$ as calculated using Monte Carlo techniques as a function of the number of samples used in each repetition. The analytical solution to the area is 30 units as given by the red line.

984 This technique performs a semi-random stochastic walk through the allowable pa-
 985 rameter space. This builds a posterior distribution which has the property that the
 986 density of sampled points is proportional to the probability density of that parame-
 987 ter. This does mean that the samples produced by this technique are not statistically
 988 independent but they will cover the space of the distribution.

989 A Markov chain functions by selecting the position of step \vec{x}_{i+1} based on the
 990 position of \vec{x}_i . The space in which the Markov chain selects samples is dependent
 991 upon the total number of parameters utilised within the fit, where a discrete point in
 992 this space is described by the N-dimensional space \vec{x} . In a perfectly operating Markov
 993 chain, the position of the next step depends solely on the previous step and not on the
 994 further history of the chain (\vec{x}_0, \vec{x}_1 , etc.). However, in solving the multi-dimensionality
 995 of the fit used within this analysis, each step becomes correlated with several of
 996 the steps preceding itself. This behaviour is further explained in subsection 3.2.3.
 997 Providing the MCMC chain is well optimised, it will begin to converge towards a

998 unique stationary distribution. The period between the chain's initial starting point
999 and the convergence to the unique stationary distribution is colloquially known as the
1000 burn-in period. This is discussed further in subsection 3.2.3. Once the chain reaches
1001 the stationary distribution, all points sampled after that point will look like samples
1002 from that distribution.

1003 Further details of the theories underpinning MCMC techniques are discussed
1004 in [124] but can be summarised by the requirement that the chain satisfies the three
1005 'regularity conditions':

- 1006 • Irreducibility: From every position in the parameter space \vec{x} , there must exist a
1007 non-zero probability for every other position in the parameter space to be reached.
- 1008 • Recurrence: Once the chain arrives at the stationary distribution, every step fol-
1009 lowing from that position must be samples from the same stationary distribution.
- 1010 • Aperiodicity: The chain must not repeat the same sequence of steps at any point
1011 throughout the sampling period.

1012 The output of the chain after burn-in (ie. the sampled points after the chain
1013 has reached the stationary distribution) can be used to approximate the posterior
1014 distribution and model parameters $\vec{\theta}$. To achieve the requirement that the unique
1015 stationary distribution found by the chain be the posterior distribution, one can use
1016 the Metropolis-Hastings algorithm. This guides the stochastic process depending on
1017 the likelihood of the current proposed step compared to that of the previous step.
1018 Implementation and other details of this technique are discussed in subsection 3.2.2.

1019 3.2.2 Metropolis-Hastings Algorithm

1020 As a requirement for MCMCs, the Markov chain implemented in this technique must
 1021 have a unique stationary distribution that is equivalent to the posterior distribution.
 1022 To ensure this requirement and that the regularity conditions are met, this analysis
 1023 utilises the Metropolis-Hastings (MH) algorithm [128,129]. For the i^{th} step in the chain,
 1024 the MH algorithm determines the position in the parameter space to which the chain
 1025 moves to based on the current step, \vec{x}_i , and the proposed step, \vec{y}_{i+1} . The proposed step
 1026 is randomly selected from some proposal function $f(\vec{x}_{i+1}|\vec{x}_i)$, which depends solely
 1027 on the current step (ie. not the further history of the chain). The next step in the chain
 1028 \vec{x}_{i+1} can be either the current step or the proposed step determined by whether the
 1029 proposed step is accepted or rejected. To decide if the proposed step is selected, the
 1030 acceptance probability, $\alpha(\vec{x}_i, \vec{y}_i)$, is calculated as

$$\alpha(\vec{x}_i, \vec{y}_{i+1}) = \min\left(1, \frac{P(\vec{y}_{i+1}|D)f(\vec{x}_i|\vec{y}_{i+1})}{P(\vec{x}_i|D)f(\vec{y}_{i+1}|\vec{x}_i)}\right). \quad (3.4)$$

1031 Where $P(\vec{y}_{i+1}|D)$ is the posterior distribution as introduced in section 3.1. To
 1032 simplify this calculation, the proposal function is required to be symmetric such that
 1033 $f(\vec{x}_i|\vec{y}_{i+1}) = f(\vec{y}_{i+1}|\vec{x}_i)$. In practice, a multi-variate Gaussian distribution is used to
 1034 throw parameter proposals from. This reduces Equation 3.4 to

$$\alpha(\vec{x}_i, \vec{y}_{i+1}) = \min\left(1, \frac{P(\vec{y}_{i+1}|D)}{P(\vec{x}_i|D)}\right). \quad (3.5)$$

After calculating this quantity, a random number, β , is generated uniformly between 0 and 1. If $\beta \leq \alpha(\vec{x}_i, \vec{y}_{i+1})$, the proposed step is accepted. Otherwise, the chain sets the next step equal to the current step and this procedure is repeated. This can be interpreted as if the posterior probability of the proposed step is greater than that of the current step, ($P(\vec{y}_{i+1}|D) \geq P(\vec{x}_i|D)$), the proposed step will always be accepted. If the opposite is true, ($P(\vec{y}_{i+1}|D) \leq P(\vec{x}_i|D)$), the proposed step will be accepted with probability $P(\vec{x}_i|D)/P(\vec{y}_{i+1}|D)$. This ensures that the Markov chain does not get trapped in any local minima in the potentially non-Gaussian posterior distribution. The outcome of this technique is that the density of steps taken in a discrete region is directly proportional to the probability density in that region.

3.2.3 MCMC Optimisation

As discussed in subsection 3.2.2, the proposal function invoked within the MH algorithm can take any form and the chain will still converge to the stationary distribution. As discussed in [DB: Link to Analysis Strategy Section](#), this analysis performs the Monte Carlo reweighting on an event-by-event basis. This requires significant computational resources to perform a parameter fit. Therefore, the number of steps taken before the unique stationary distribution is found should be minimised as only steps after convergence add information to the fit. Furthermore, the chain should entirely cover the allowable parameter space to ensure that all values have been considered. Tuning the distance that the proposal function jumps between steps on a parameter-by-parameter basis can both minimise the length of the burn-in period and ensure that the correlation between step \vec{x}_i and \vec{x}_j is sufficiently small.

The effect of changing the width of the proposal function is highlighted in Figure 3.3. Three scenarios, each with the same underlying stationary distribution (A Gaussian of width 1.0 and mean 0.), are presented. The only difference between the three scenarios

is the width of the proposal function, colloquially known as the ‘step size σ ’. Each scenario starts at an initial parameter value of 10.0 which would be considered an extreme variation. For the case where $\sigma = 0.1$, it is clear to see that the chain takes a long time to reach the expected region of the parameter. This indicates that this chain would have a large burn-in period and does not converge to the stationary distribution until step ~ 500 . Furthermore, whilst the chain does move towards the expected region, each step is significantly correlated with the previous. Considering the case where $\sigma = 5.0$, the chain approaches the expected parameter region almost instantly meaning that the burn-in period is not significant. However, there are clearly large regions of steps where the chain does not move. This is likely due to the chain proposing steps in the tails of the distribution which have a low probability of being accepted. Consequently, this chain would take a significant number of steps to fully span the allowable parameter region. For the final scenario, where $\sigma = 0.5$, you can see a relatively small burn-in period of approximately 100 steps. Once the chain reaches the stationary distribution, it moves throughout the expected region of parameter values many times, sufficiently sampling the full parameter region. This example is a single parameter varying across a continuous distribution and does not fully reflect the difficulties in the many-hundred multi-variate parameter distribution used within this analysis. However, it does give a conceptual idea of the importance of selecting the proposal function and associated step size.

As discussed, step size tuning directly correlates to the average step acceptance rate. If the step size is too small, many steps will be accepted but the chain moves slowly. If the opposite is true, many steps will be rejected as the chain proposes steps in the tails of the distribution. Discussion in [130] suggests that the ‘ideal’ acceptance rate of a high dimension MCMC chain should be approximately $\sim 25\%$. An “ideal” step size [130] of

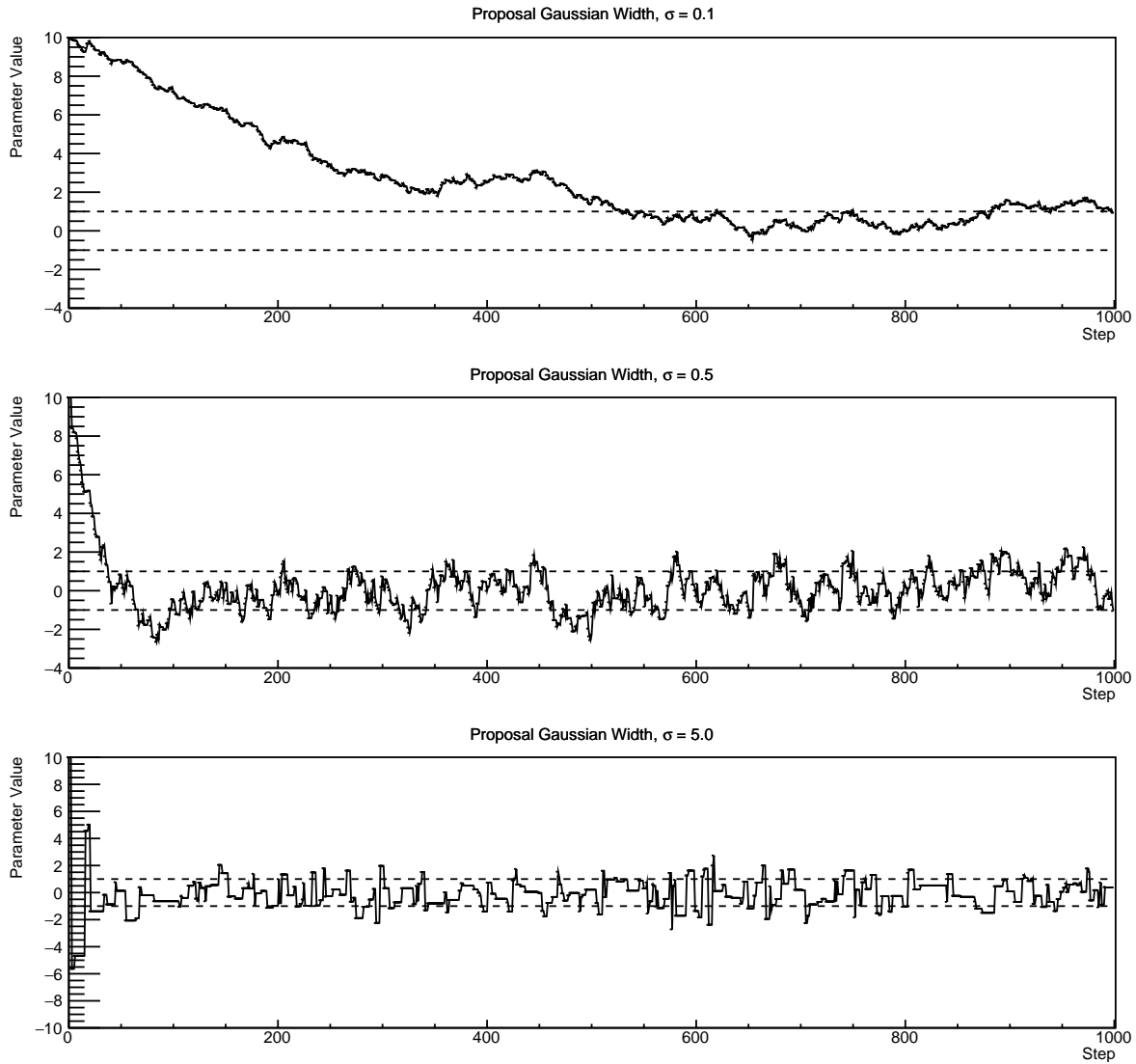


Figure 3.3: Three MCMC chains, each with a stationary distribution equal to a Gaussian centered at 0 and width 1 (As indicated by the black dotted lines). All of the chains use a Gaussian proposal function but have different widths (or ‘step size σ ’). The top panel has $\sigma = 0.1$, middle panel has $\sigma = 0.5$ and the bottom panel has $\sigma = 5.0$.

$$\sigma = \frac{2.4}{N_p}, \quad (3.6)$$

1086 where N_p is the number of parameters included in the MCMC fit. However, the
1087 complex correlations between systematics mean that some parameters have to be hand

1088 tuned and many efforts have been taken to select a set of parameter-by-parameter step
 1089 sizes to approximately reach the ideal acceptance rate.

1090 Figure 3.3 highlights the likelihood as calculated by the fit in [DB: Link to AsimovA](#)
 1091 [Sensitivity Section](#) as a function of the number of steps in each chain. In practice,
 1092 many independent MCMC chains are run simultaneously to parallelise the task of
 1093 performing the fit. This figure overlays the distribution found in each chain. As seen,
 1094 the likelihood decreases from its initial value and converges towards a stationary
 1095 distribution after $\sim 1 \times 10^5$ steps. Each fit (whether it be different asimov fits or data
 1096 fit) will have a different set of preferred parameter values which results in a different
 1097 stationary distribution. For each fit presented in this thesis, a burn-in period of 1×10^5
 1098 steps was found to be sufficient.

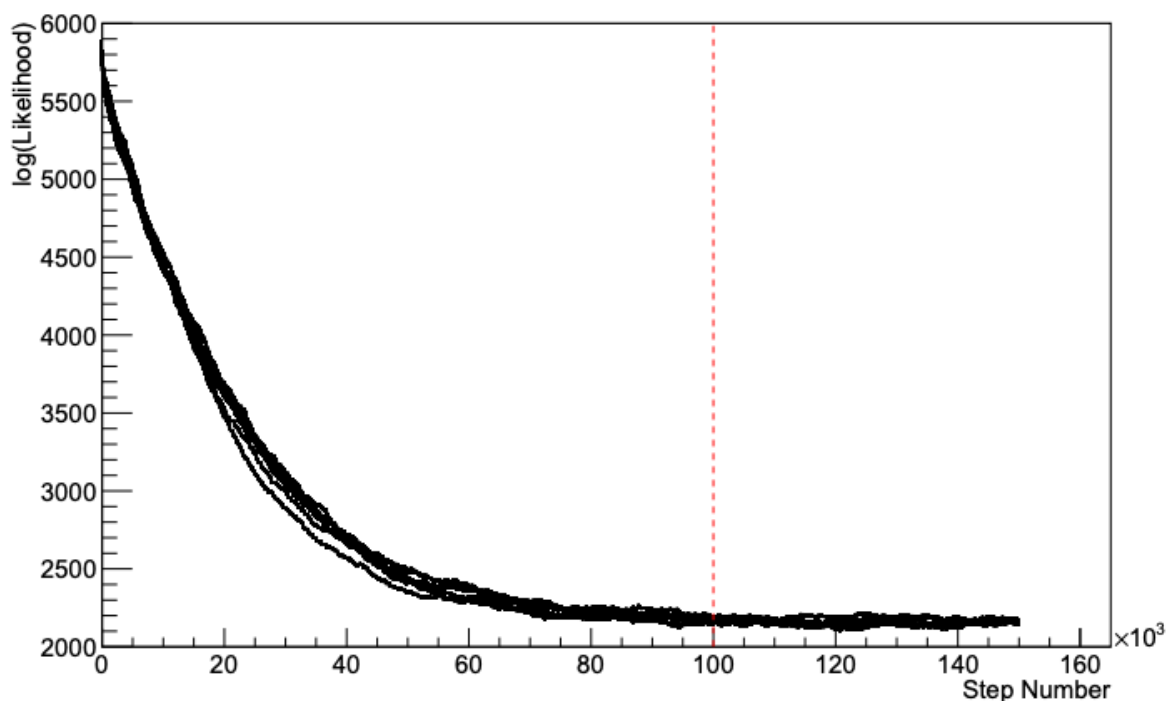


Figure 3.4: The log-likelihood from the fit detailed in [DB: Link to AsimovA](#) [Sensitivity Section](#) as a function of the number of steps accumulated in each fit. Many independent MCMC chains were run in parallel and overlaid on this plot. The red line indicates the 1×10^5 step burn-in period after which the log-likelihood becomes stable.

¹⁰⁹⁹ 3.3 Understanding the MCMC Results

¹¹⁰⁰ Whilst section 3.1 and section 3.2 describe how to interpret Bayesian statistics and
¹¹⁰¹ explains the MCMC techniques used within this analysis, there is no mention of
¹¹⁰² how to interpret the output of the chain. The posterior distribution output from the
¹¹⁰³ chain is a high dimension object, with as many dimensions as there are parameters
¹¹⁰⁴ included in the fit. However, this multi-dimensional object is difficult to conceptualize
¹¹⁰⁵ so parameter estimations are often presented in one or two-dimensional projections
¹¹⁰⁶ of this probability distribution. To do this, we invoke the marginalisation technique
¹¹⁰⁷ highlighted in subsection 3.3.1.

¹¹⁰⁸ 3.3.1 Maginalisation

¹¹⁰⁹ The output of the MCMC chain is a highly dimensional probability distribution
¹¹¹⁰ which is very difficult to interpret. From the standpoint of an oscillation analysis
¹¹¹¹ experiment, the one or two-dimensional ‘projections’ of the oscillation parameters of
¹¹¹² interest are most relevant. Despite this, the best fit values and uncertainties on the
¹¹¹³ oscillation parameters of interest should correctly encapsulate the correlations to the
¹¹¹⁴ other systematic uncertainties (colloquially called ‘nuisance’ parameters). For this joint
¹¹¹⁵ beam and atmospheric analysis, the oscillation parameters of interest are $\sin^2(\theta_{23})$,
¹¹¹⁶ $\sin^2(\theta_{13})$, Δm_{23}^2 , and δ_{CP} . All other parameters (Including the oscillation parameter
¹¹¹⁷ this fit is insensitive to) are deemed nuisance parameters. To generate these projections,
¹¹¹⁸ we rely upon integrating the posterior distribution over all nuisance parameters. This
¹¹¹⁹ is called marginalisation. A simple example of this technique is to imagine the scenario
¹¹²⁰ where two coins are flipped. To determine the probability that the first coin returned
¹¹²¹ a ‘head’, the exact result of the second coin flip is disregarded and simply integrated

1122 over. For the parameters of interest, $\vec{\theta}_i$, we can calculate the marginalised posterior by
1123 integrating over the nuisance parameters, $\vec{\theta}_n$. In this case, Equation 3.2 becomes

$$P(\vec{\theta}_i|D) = \frac{\int P(D|\vec{\theta}_i, \vec{\theta}_n)P(\vec{\theta}_i, \vec{\theta}_n)d\vec{\theta}_n}{\int P(D|\vec{\theta})P(\vec{\theta})d\vec{\theta}} \quad (3.7)$$

1124 Where $P(\vec{\theta}_i, \vec{\theta}_n)$ encodes the prior knowledge about the uncertainty and correlations
1125 between the parameters of interest and the nuisance parameters. In practice, this
1126 is simply taking the one or two-dimensional projection of the multi-dimensional
1127 probability distribution.

1128 Whilst in principle an easy solution to a complex problem, correlations between the
1129 interesting and nuisance parameters can bias the marginalised results. A similar effect
1130 is found when the parameters being marginalised over have non-Gaussian probability
1131 distributions. For example, Figure 3.5 highlights the marginalisation bias in the
1132 probability distribution found for a parameter when requiring a correlated parameter
1133 to have a positive parameter value. Due to the complex nature of this oscillation
1134 parameter fit presented in this thesis, there are certainly correlations occurring between
1135 the oscillation parameters of interest and the other nuisance parameters included in
1136 the fit.

1137 3.3.2 Parameter Estimation and Credible Intervals

1138 The purpose of this analysis is to determine the best fit values for the oscillation
1139 parameters that the beam and atmospheric samples are sensitive to; $\sin^2(\theta_{23})$, $\sin^2(\theta_{13})$
1140, Δm_{23}^2 , and δ_{CP} . Typically, the results presented take the form of one or two-dimension
1141 marginalised probability distributions for the appearance ($\sin^2(\theta_{13})$ and δ_{CP}) and

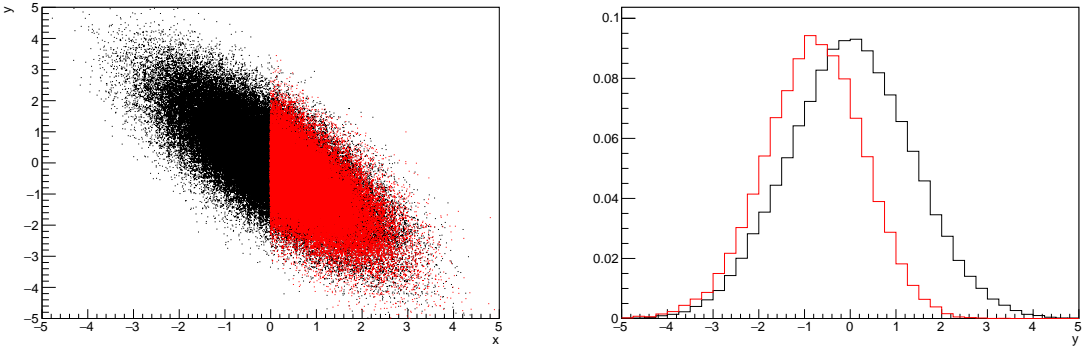


Figure 3.5: Left: The two dimensional probability distribution for two correlated parameters x and y . The red distribution shows the two dimensional probability distribution when $0 \leq x \leq 5$. Right: The marginalised probability distribution for the y parameter found when requiring the x to be bound between $-5 \leq x \leq 5$ and $0 \leq x \leq 5$ for the black and red distribution, respectively.

1142 disappearance ($\sin^2(\theta_{23})$ and Δm_{23}^2) parameters. The posterior probability density
 1143 taken from the output MCMC chain is binned in these parameters. The parameter
 1144 best-fit point is then taken to be the value that has the highest posterior probability.
 1145 This is performed in both one and two-dimensional projections.

1146 However, the single best-fit point in a given parameter is not of much use on its
 1147 own. We would also like to determine the uncertainty, or credible interval, on that
 1148 best-fit point. The definition of the 1σ credible interval is that we have 68% belief that
 1149 the parameter is within those bounds. For a more generalised definition, the credible
 1150 interval is the region of the posterior distribution that contains a specific fraction of
 1151 the total probability, such that

$$\int P(\theta|D)d\theta = \alpha \quad (3.8)$$

1152 Where θ is the parameter on which we calculate the credible interval. This technique
 1153 then calculates the $\alpha \times 100\%$ credible interval.

1154 In practice, this analysis uses the highest posterior density (HPD) credible intervals
 1155 which are calculated through the following method. First, the probability distribution
 1156 is area-normalised such that it has an integrated area equal to 1.0. The bins of proba-
 1157 bility are then summed from the highest to lowest until the sum exceeds the 1σ level
 1158 (0.68 in this example). This process is repeated for a range of credible intervals, notably
 1159 the 1σ , 2σ and 3σ along with other levels where the critical values for each level can
 1160 be found in [131]. This process can be repeated for the two-dimensional probability
 1161 distributions by creating two-dimensional contours of credible intervals rather than a
 1162 one-dimensional result.

1163 3.3.3 Application of Bayes' Theorem

1164 Due to the matter resonance, this analysis has some sensitivity to the mass hierarchy
 1165 of neutrino states (whether Δm_{23}^2 is positive or negative) and the octant of $\sin^2(\theta_{23})$
 1166 . The Bayesian approach utilised within this analysis gives an intuitive method of
 1167 model comparison by determining which hypothesis is most favourable. Taking the
 1168 ratio of Equation 3.3 for the two hypotheses of normal hierarchy, NH , and inverted
 1169 hierarchy, IH , gives

$$\frac{P(\vec{\theta}_{NH}|D)}{P(\vec{\theta}_{IH}|D)} = \frac{P(D|\vec{\theta}_{NH})}{P(D|\vec{\theta}_{IH})} \times \frac{P(\vec{\theta}_{NH})}{P(\vec{\theta}_{IH})}. \quad (3.9)$$

1170 The middle term defines the Bayes factor which is a data-driven interpretation of
 1171 how strong the data prefers one hierarchy to the other. For this analysis, equal priors
 1172 on both mass hierarchy hypotheses are chosen ($P(\vec{\theta}_{NH}) = P(\vec{\theta}_{IH}) = 0.5$). In practice,
 1173 the MCMC chain proposes a value of $|\Delta m_{23}^2|$ and then applies a 50% probability
 1174 that the value is sign flipped. Consequently, the Bayes factor can be calculated from

₁₁₇₅ the ratio of the probability density in either hypothesis. This equates to counting the
₁₁₇₆ number of steps taken in the normal and inverted hierarchies and taking the ratio. The
₁₁₇₇ same approach can be taken to compare the upper octant (UO) compared to the lower
₁₁₇₈ octant (LO) hypothesis of $\sin^2(\theta_{23})$.

₁₁₇₉ Whilst the value of the Bayes factor should always be shown, the Jeffreys scale [132]
₁₁₈₀ (highlighted in Table 3.1) gives an indication of the strength of preference for one model
₁₁₈₁ compared to the other. Other interpretations of the strength of preference of a model
₁₁₈₂ exist, e.g. the Kass and Raferty Scale [133].

$\log_{10}(B_{AB})$	B_{AB}	Strength of Preference
< 0.0	< 1	No preference for hypothesis A (Supports hypothesis B)
0.0 – 0.5	1.0 – 3.16	Preference for hypothesis A is weak
0.5 – 1.0	3.16 – 10.0	Preference for hypothesis A is substantial
1.0 – 1.5	10.0 – 31.6	Preference for hypothesis A is strong
1.5 – 2.0	31.6 – 100.0	Preference for hypothesis A is very strong
> 2.0	> 100.0	Decisive preference for hypothesis A

Table 3.1: Jeffreys scale for strength of preference for two models A and B as a function of the calculated Bayes factor ($B_{AB} = B(A/B)$) between the two models [132]. The original scale is given in terms of $\log_{10}(B(A/B))$ but converted to linear scale for easy comparison throughout this thesis.

₁₁₈₃ 3.3.4 Comparison of MCMC Output to Expectation

₁₁₈₄ Whilst not important for the extraction of oscillation parameters, understanding how
₁₁₈₅ the data constrains the model parameters is important to the understanding of this
₁₁₈₆ analysis. A simple method of doing this is to perform a comparison in the fitting
₁₁₈₇ parameters (For instance, the reconstructed neutrino energy and lepton direction for
₁₁₈₈ T2K far detector beam samples) of the spectra generated by the MCMC chain to ‘data’.
₁₁₈₉ This ‘data’ could be true data or some variation of Monte Carlo prediction. This allows
₁₁₉₀ easy comparison of the MCMC probability distribution to the data. To perform this, N

1191 steps from the post burn-in MCMC chain are randomly selected (Where for all plots
1192 of this style in this thesis, $N = 3000$). From these, the Monte Carlo prediction at each
1193 step is generated by reweighting the model parameters to the values specified at that
1194 step. Due to the probability density being directly correlated with the density of steps
1195 in a certain region, parameter values close to the best fit value are most likely to be
1196 selected.

1197 In practice, for each bin of the fitting parameters has a probability distribution
1198 of event rates, with one entry per sampled MCMC step. This distribution is binned
1199 where the bin with the highest probability is selected as the mean and an error on
1200 the width of this probability distribution is calculated using the approach highlighted
1201 in subsection 3.3.2. Consequently, the best fit distribution in the fit parameter is not
1202 necessarily that which would be attained by reweighting the Monte Carlo prediction
1203 to the most probable parameter values.

1204 A similar study can be performed to illustrate the freedom of the model parameter
1205 space prior to the fit. This can be done by throwing parameter values from the prior
1206 uncertainty of each parameter. This becomes troublesome for parameters with no
1207 prior uncertainty as the range is technically infinite. Where applicable solutions to
1208 remove these have been addressed.

₁₂₀₉ **Chapter 4**

₁₂₁₀ **Simulation, Reconstruction and Event Se-**
₁₂₁₁ **lections**

₁₂₁₂ **4.1 Simulation**

₁₂₁₃ In order to generate a Monte Carlo prediction of the expected event rate at the far
₁₂₁₄ detector for both sets of samples, all the processes in the beamline, atmospheric flux,
₁₂₁₅ neutrino interaction, and detector need to be modeled. The beamline simulation
₁₂₁₆ consists of three distinct parts; initial hadron interaction modeling, target station
₁₂₁₇ geometry and particle tracking and hadronic re-interactions. These are modeled by
₁₂₁₈ FLUKA [134], JNUBEAM [135, 136], and GCALOR [137], respectively. FLUKA is
₁₂₁₉ not very adaptable but matches external cross-section measurements in the region of
₁₂₂₀ interest better than GCALOR ($O(10)$ GeV). Thus a small simulation is built to model
₁₂₂₁ the interactions in the target and the output is then passed to JNUBEAM and GCALOR
₁₂₂₂ for propagation. The hadronic interactions are tuned to data from the NA61/SHINE
₁₂₂₃ [138–140] and HARP [141] experiments. The tuning is done by reweighting the FLUKA
₁₂₂₄ and GCALOR predictions to match the external data multiplicity and cross-section
₁₂₂₅ measurements, based on final state particle kinematics [142]. The predicted flux for
₁₂₂₆ neutrino and antineutrino beam modes is illustrated in Figure 2.7.

₁₂₂₇ The atmospheric neutrino flux predictions are simulated by the HKKM model
₁₂₂₈ [42, 44], where the primary cosmic ray flux is tuned to AMS [143] and BESS [144]

1229 external data assuming the US-standard atmosphere '76 [145] density profile and
1230 includes geomagnetic field effects. Secondary interactions of pions and muons are
1231 handled by DPMJET-III [146] for energies above 32GeV and JAM [44, 147] for energies
1232 below that value. These hadronic interactions are tuned to external data [148, 149]
1233 using the same methodology as the tuning of the beamline simulation. The energy
1234 and cosine zenith predictions of $\nu_e, \bar{\nu}_e, \nu_\mu, \bar{\nu}_\mu$ flux are given in Figure 1.3 and Figure 1.5,
1235 respectively. The flux is approximately symmetrical and peaked around $\cos(\theta_Z) = 0.0$.
1236 This is because horizontally-going pions and kaons can travel further than their
1237 vertically-going counterparts resulting in a larger probability of decay to neutrinos.
1238 The symmetry is broken in low-energy neutrinos due to geomagnetic effects, which
1239 modify the track of the primary cosmic rays.

1240 The neutrino interactions in all three detectors are simulated with NEUT [150, 151].
1241 This simulates quasi-elastic (QE), meson exchange (MEC), single meson production
1242 (PROD), coherent pion production (COH), and deep inelastic scattering (DIS) interac-
1243 tions. These interaction categories can be further broken down by whether they were
1244 propagated via a W^\pm boson in Charged Current (CC) interactions or via a Z^0 boson
1245 in Neutral Current (NC) interactions. CC interactions have a charged lepton in the
1246 final state, which can be flavour-tagged in reconstruction to determine the flavour
1247 of the neutrino. In contrast, NC interactions have a neutrino in the final state so no
1248 flavour information can be determined from the observables in the detector. This is
1249 the reason why NC events are assumed to not oscillate within the analysis. Both CC
1250 and NC interactions are modeled for all the above interaction categories, other than
1251 MEC interactions which are only modeled for CC events. The SK detector is only
1252 sensitive to charged particles, so all charged current interactions are simulated whilst
1253 only neutral current processes that produce charged mesons (NCDIS, NCCOH, and
1254 NCPROD) are modeled. NC MEC interactions can only produce charged particles
1255 through secondary re-interactions which is a low cross-section process.

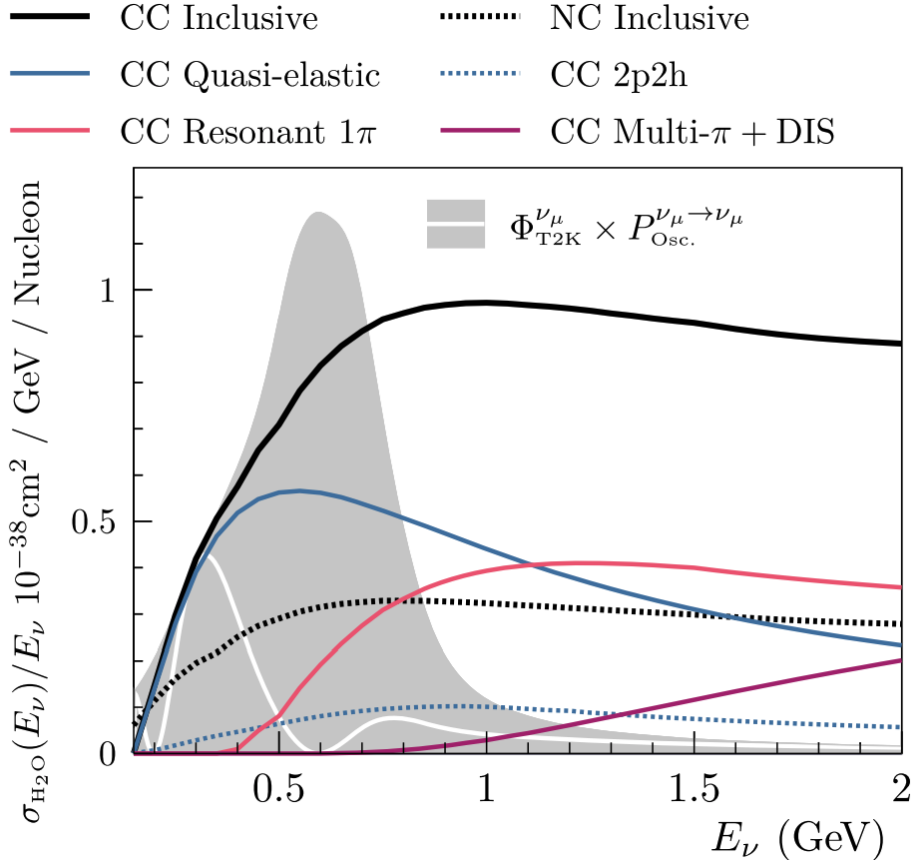


Figure 4.1: The NEUT prediction of the ν_μ -H₂O cross-section overlaid on the T2K ν_μ flux. The charged current (black, solid) and neutral current (black, dashed) inclusive, charged current quasi-elastic (blue, solid), charged current 2p2h (blue, dashed), charged current single pion production (pink), and charged current multi- π and DIS (Purple) cross-sections are illustrated. Taken from [150].

As illustrated in Figure 4.1, QE interactions dominate the low-energy cross-section of neutrino interactions. The NEUT implementation adopts the Llewellyn Smith [152] model for neutrino-nucleus interactions, where the nuclear ground state of any bound nucleons (neutrino-oxygen interactions) is approximated by a spectral-function [153] model that simulates the effects of Fermi momentum and Pauli blocking. The cross-section of QE interactions are controlled by vector and axial-vector form factors parameterised by the BBBA05 [154] model and a dipole form factor with $M_A^{QE} = 1.21\text{GeV}$ fit to external data [155], respectively. QE interactions only account for single-nucleon interactions whereas multi-nucleon interactions (or MEC) can contribute significantly to the overall cross-section. NEUT implements the Valencia [156] model

1266 to simulate MEC events, where two nucleons and two holes in the nuclear target are
1267 produced (Often called 2p2h interactions due to this effect).

1268 For neutrinos of energy $O(1)\text{GeV}$, PROD interactions become dominant. These
1269 predominantly produce charged and neutral pions although γ , kaon, and η production
1270 is also considered. To simulate these interactions, the Berger-Sehgal [157] model is
1271 implemented within NEUT. It simulates the excitation of a nucleon from a neutrino
1272 interaction, production of an intermediate baryon, and the consequential decay to a
1273 single meson or γ . Pions can also be produced through COH interactions, which occur
1274 when the incoming neutrino interacts with the entire oxygen nuclei target leaving a
1275 single pion outside of the nucleus. NEUT utilises the Berger-Sehgal [158] model to
1276 simulate these interactions.

1277 DIS and multi- π producing interactions become the most dominant for energies
1278 $> O(5)\text{GeV}$. PYTHIA [159] is used to simulate any interaction with invariant mass,
1279 $W > 2\text{GeV}/c^2$, which produces at least one meson. For any interaction which produces
1280 at least two mesons but has $W < 2\text{GeV}/c^2$, the Bronner model is invoked [160].
1281 Both of these models use Parton distribution functions based on the Bodek-Yang
1282 model [161–163].

1283 Any pion which is produced within the nucleus can re-interact through final state
1284 interactions before it exits, as illustrated by the scattering, absorption, production, and
1285 exchange interactions in Figure 4.2. These re-interactions alter the observable particles
1286 within the detector. For instance, if the charged pion from a CC PROD interaction
1287 is absorbed, the observables would mimic a CC QE interaction. To simulate these
1288 effects, NEUT uses a semi-classical intranuclear cascade model [150]. This cascade
1289 functions by stepping the pion through the nucleus in fixed-length steps equivalent
1290 to $dx = R_N/100$, where R_N is the radius of the nucleus. At each step, the Monte
1291 Carlo allows the pion to interact through scattering, charged exchange, absorption, or

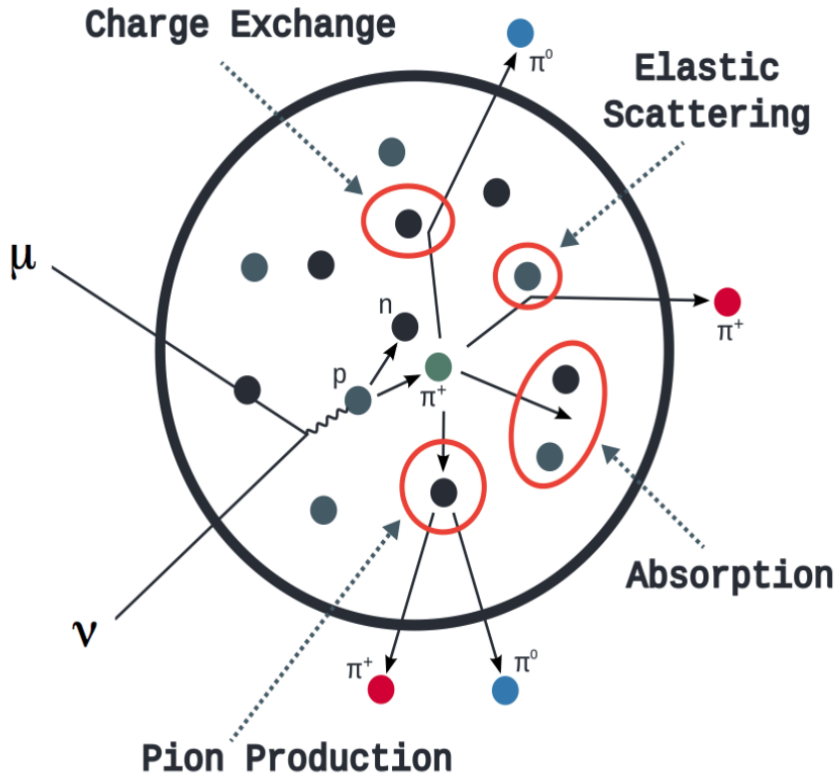


Figure 4.2: Illustration of the various processes which a pion can undergo before exiting the nucleus. Taken from [164].

1292 production with an interaction-dependent probability calculated from a fit to external
 1293 data [165]. This cascade continues until the pion is absorbed or exits the nucleus.

1294 Once the outgoing particle kinematics have been determined from NEUT, they
 1295 are passed into the detector simulation. The near detectors ND280 and INGRID are
 1296 simulated using a GEANT4 package [109, 166] to simulate the detector geometry and
 1297 particle tracking. The response of the detectors is simulated using the elecSim pack-
 1298 age. The far detector simulation is based upon the original Kamiokande experiment
 1299 software which uses the GEANT3-based SKDETSIM [109, 167] package. This controls
 1300 the interactions of particles in the water as well as Cherenkov light production. The
 1301 water quality and PMT calibration measurements detailed in subsection 2.1.2 are also
 1302 used within this simulation to make accurate predictions of the detector response.

1303 4.2 Event Reconstruction at SK

1304 Any above Cherenkov threshold event which occurs in SK will be recorded by the
1305 PMT array, where each PMT records the time and accumulated charge is measured.
1306 This is shown in the event displays illustrated in Figure 4.3. To be useful for physics
1307 analyses, this series of PMT hit information needs to be reconstructed to determine the
1308 particle’s identity and kinematics. This is because the charge and timing distribution
1309 of photons generated by a particular particle in an event is dependent upon its initial
1310 vertex position, time, direction, and momentum of the particle.

1311 For the purposes of this analysis, the `fitQun` reconstruction algorithm is utilised.
1312 Its core function is to compare a prediction of the accumulated charge and timing
1313 distribution from each PMT, generated for a particular particle hypothesis, to that
1314 observed in the neutrino event. It determines the best particle hypothesis by min-
1315 imising a likelihood function which includes information from PMTs which were hit
1316 and those that were not hit. This improves upon the `APFit` reconstruction algorithm
1317 which has been used for many previous SK analyses. `APFit` only includes information
1318 from PMTs within the 43 deg Cherenkov cone and then sequentially fits the kinematic
1319 parameters and particle configuration. Conversely, `fitQun` performs a simultaneous
1320 fit, improving both the accuracy of the fit parameters and the rejection of neutral
1321 current π^0 events [168, 169]. The `fitQun` algorithm is based on the key concepts
1322 on the MiniBooNE reconstruction algorithm [170] and is described in [171] which is
1323 summarised below.

1324 An event in SK can consist of multiple “sub-events”. For example, a muon neutrino
1325 interaction will generate a muon which will subsequently decay into an electron.
1326 Both the muon and electron can generate Cherenkov photons but both subevents
1327 need to be reconstructed separately. Therefore, to avoid assigning photons generated

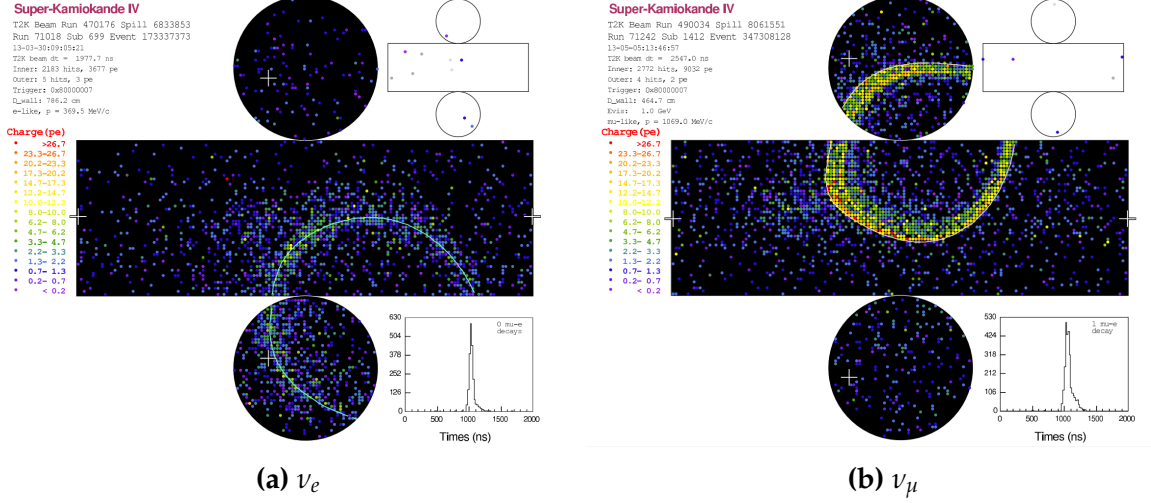


Figure 4.3: Event displays from Super Kamiokande illustrating the “crisp” ring from a muon and the typically “fuzzy” electron ring. Each pixel represents a PMT and the color scheme denotes the accumulated charge deposited on that PMT. Figures taken from [172].

1328 by the decay-electron to the muon, each event is divided into time clusters, termed
 1329 “subevents”, where subevent is defined to contain at most one hit for each PMT. To
 1330 find the subevents, a vertex goodness metric is calculated for some vertex position \vec{x}
 1331 and time t ,

$$G(\vec{x}, t) = \sum_i^{\text{hit PMTs}} \exp \left(-\frac{1}{2} \left(\frac{T_{Res}^i(\vec{x}, t)}{\sigma} \right)^2 \right) \quad (4.1)$$

1332 where

$$T_{Res}^i(\vec{x}, t) = t_i - t - |R_{PMT}^i - \vec{x}| / c_n \quad (4.2)$$

1333 is the residual hit time, R_{PMT}^i is the position of the i^{th} PMT, c_n is the speed of light in
 1334 water and $\sigma = 4\text{ns}$ which is comparable to the time resolution of the PMT. When the fit

1335 values of time and vertex are close to the true values, $T_{Res}^i(\vec{x}, t)$ tends to zero resulting
 1336 in subevents appearing as spikes in the goodness metric. The fit vertex and time are
 1337 grid-scanned, and the values which maximise the goodness metric are selected as the
 1338 “pre-fit vertex”. Whilst this predicts a vertex for use in the clustering algorithm, the
 1339 final vertex is fit using the higher-precision maximum likelihood method described
 1340 below.

1341 Once the pre-fit vertex has been determined, the goodness metric is scanned as a
 1342 function of t to determine the number of delayed peaks. A peak-finding algorithm
 1343 is then used on the goodness metric, requiring the goodness metric to exceed some
 1344 threshold and drop below a reduced threshold before any delayed additional peaks
 1345 are considered. The thresholds are set such that the rate of false peak finding is
 1346 minimised while still attaining good data to Monte Carlo agreement. To improve
 1347 performance, the pre-fit vertex for each delayed subevent is re-calculated after PMT
 1348 hits from the primary subevent are masked. This improves the decay-electron tagging
 1349 performance. Once all subevents have been determined, the time window around
 1350 each subevent is then defined by the earliest and latest time which satisfies $-180 <$
 1351 $T_{Res}^i < 800\text{ns}$. The subevents and associated time windows are then used as seeds for
 1352 further reconstruction.

1353 For a given subevent, `fiTQun` constructs a likelihood based on the accumulated
 1354 charge q_i and time information t_i from the i^{th} PMT,

$$L(\Gamma, \vec{\theta}) = \prod_j^{\text{unhit}} P_j(\text{unhit}|\Gamma, \vec{\theta}) \prod_i^{\text{hit}} \{1 - P_i(\text{unhit}|\Gamma, \vec{\theta})\} f_q(q_i|\Gamma, \vec{\theta}) f_t(t_i|\Gamma, \vec{\theta}), \quad (4.3)$$

1355 where $\vec{\theta}$ defines the track parameters; vertex position, direction vector and mo-
 1356 menta, and Γ represents the particle hypothesis. $P_i(\text{unhit}|\Gamma, \vec{\theta})$ defines the probability

₁₃₅₇ of the i^{th} tube to not register a hit given the track parameters and particle hypothesis.
₁₃₅₈ The charge likelihood, $f_q(q_i|\Gamma, \vec{\theta})$, and time likelihood, $f_t(t_i|\Gamma, \vec{\theta})$, represent the probability density function of observing charge q_i and time t_i on the i^{th} PMT given track parameters $\vec{\theta}$ and particle hypothesis Γ .

₁₃₆₁ As the generation and propagation of the optical photons are independent of the
₁₃₆₂ PMT and electronics response, it is natural to split the calculation into two. Firstly,
₁₃₆₃ calculating the expected number of photoelectrons (or predicted charge), μ_i , at the
₁₃₆₄ i^{th} PMT, and then calculating the likelihood based on this value. This substitution
₁₃₆₅ allows the charge likelihood density $f_q(q_i|\mu_i)$ and unhit probability $P_i(\text{unhit}|\mu_i)$ to be
₁₃₆₆ expressed via quantities that are only dependent on the response of the PMT.

₁₃₆₇ The predicted charge is calculated based on contributions from both the direct
₁₃₆₈ light and the scattered light. The direct light contribution is determined based on the
₁₃₆₉ integration of the Cherenkov photon profile along the track. PMT angular acceptance
₁₃₇₀ and water quality and calibration measurements discussed in subsection 2.1.2 are
₁₃₇₁ included to accurately model the detector's response. The scattered light is calculated
₁₃₇₂ in a similar way although it includes a scattering function that depends on the vertex
₁₃₇₃ of the particle and the position of the PMT. The charge likelihood is calculated by
₁₃₇₄ comparing the prediction to the observed charge in the PMT, where the prediction
₁₃₇₅ assumes photoelectron generation obeys a Poisson distribution.

₁₃₇₆ The time likelihood is approximated to depend on the vertex \vec{x} , direction \vec{d} , and
₁₃₇₇ time t of the track parameters as well as the particle hypothesis. The expected time
₁₃₇₈ for PMT hits is calculated by assuming unscattered photons being emitted from the
₁₃₇₉ midpoint of the track, S_{mid} ,

$$t_i^{exp} = t + S_{mid}/c + |R_{PMT}^i - \vec{x} - S_{mid}\vec{d}|/c_n, \quad (4.4)$$

where c is the speed of light in a vacuum. The time likelihood is then expressed in terms of the residual difference between the PMT hit time and the expected hit time, $t_i^{Res} = t_i - t_i^{exp}$. As the first photon hit defines the PMT hit time, the time likelihood density profile is narrower for higher momenta particles which introduces a dependence on the predicted charge. The particle hypothesis and momentum also affect the Cherenkov photon distribution which modifies the shape of the time likelihood density since in reality not all photons are emitted at the midpoint of the track. As with the charge likelihood, the contributions from both the direct and scattered light to the time likelihood density are calculated separately, which are both calculated from particle gun studies.

The track parameters, $\vec{\theta}$, which maximise $L(\Gamma|\vec{\theta})$ are defined the best fit parameters. In practice MINUIT [173] is used to minimise the value of $-\ln L(\Gamma, \vec{\theta})$. The particle hypothesis is determined by the comparison of $L(\Gamma, \vec{\theta})$ across all viable hypotheses, Γ . The fit considers an electron-like, muon-like, and charged pion-like hypothesis. The particle's identity is determined by taking the ratio of the likelihood of each of the hypotheses. For instance, electrons and muons are distinguished by considering the value of $\ln(L_e/L_\mu)$ as illustrated in Figure 4.4.

Alongside the three hypotheses which have a single final state particle generating optical photons, denoted “single-ring” particle hypotheses, the `fitQun` algorithm also considers a π^0 hypothesis. To do this, it performs a fit looking for two standard electron-hypothesis tracks which point to the same vertex position and time. This assumes the electron tracks are generated from photon-conversion so the electron tracks actually appear offset from the proposed π^0 vertex. For these fits, the conversion length, direction, and momenta of each photon are also considered as track parameters which are then fit in the same methodology as the standard single-ring hypotheses.

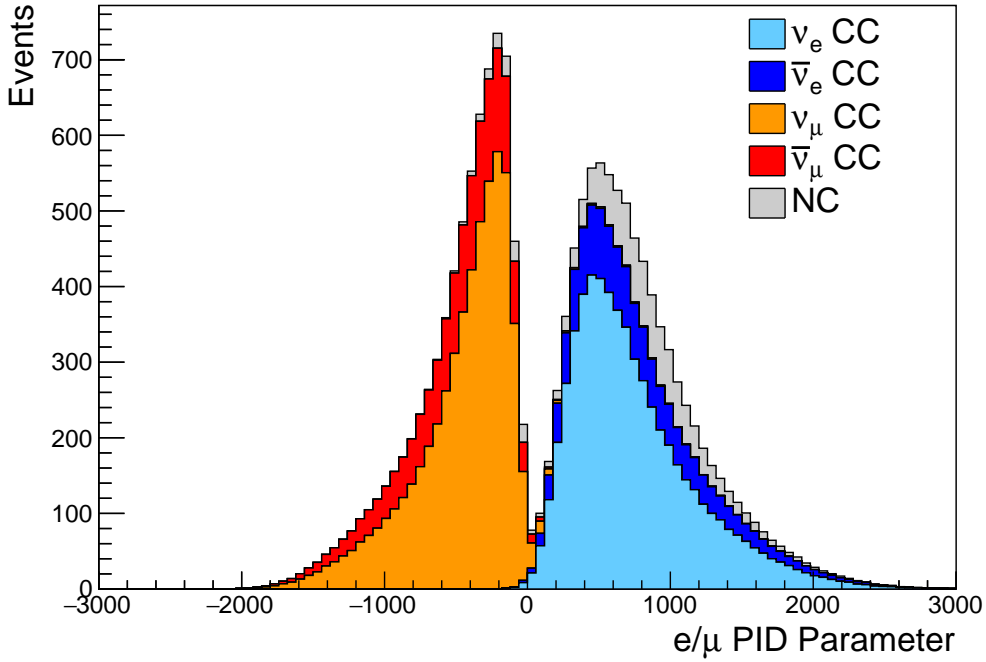


Figure 4.4: The electron/muon PID separation parameter for all sub-GeV single-ring events in SK-IV. The charged current (CC) component is broken down in four flavours of neutrino ($\nu_\mu, \bar{\nu}_\mu, \nu_e$ and $\bar{n}u_e$). Events with positive values of the parameter are determined to be electron-like.

The previous discussion pertains to a single final state particle that generates optical photons. However, the higher energy atmospheric neutrino events can generate final states with multiple particles which generate Cherenkov photons. These “multi-ring” hypotheses are also considered in the `fitQun` algorithm, but only for the first subevent in each ring to reduce computational cost. When calculating the charge likelihood density, the predicted charge associated with each ring is calculated separately and then merged to calculate the total accumulated charge on each PMT. Similarly, the time likelihood for the multi-ring hypothesis is calculated assuming each ring is independent. However, each track is then time-ordered based on the time of flight from the center of the track to the PMT, and the direct light from any ring incident on the PMT arrives before any scattered light. To reduce computational resources required for a fit, the multi-ring fits only consider electron-like and charged pion-like rings as the pion fit can be used as a proxy for a muon fit due to their similar mass.

1418 Typically, multi-ring fits have the largest likelihood because of the additional
1419 degrees of freedom introduced. Multi-ring fits proceed by proposing another ring
1420 to the previous fit and then fitting the parameters in the method described above.
1421 The additional ring is only added if the ratio of likelihoods between the n and $n + 1$
1422 passes the criteria. The criteria values for single-ring and multi-ring separation have
1423 been determined to be 9.35(11.83) based on Monte-Carlo studies, for hypotheses with
1424 electron-like(muon-like) the first ring.

1425 As an example of how the reconstruction depends on the detector conditions, the
1426 author of this thesis assessed the quality of event reconstruction for SK-V data. The
1427 detector systematics invoked within the T2K-only oscillation analysis are determined
1428 using data to Monte Carlo comparisons using the SK-IV data [174]. Due to tank-open
1429 maintenance occurring between SK-IV and SK-V, the dark rate of each PMT was
1430 observed to increase due to light exposure for a significant time during the repairs.
1431 This can be seen in Figure 4.5. Run-10 of the T2K experiment was conducted in the SK-
1432 V period, so the consistency of SK-IV and SK-V data needs to be studied to determine
1433 whether the SK-IV defined systematics can be applied to the run-10 data. This study
1434 was performed using the stopping muon data set for both the SK-IV and SK-V periods.
1435 This data is used due to the high rate of interactions, $O(200)$ events per hour, as well
1436 as having similar energies to muons from CCQE ν_μ interactions. The rate of cosmic
1437 muons does depend on the solar activity cycle [175]. This has been neglected in this
1438 comparison study as it is the shape of the distributions which is important for the
1439 purposes of being compared to the detector systematics. 2398.42 and 626.719 hours of
1440 SK-IV and SK-V are used which equates to 686743 and 192504 events respectively.

1441 The predicted charge used in the `fitQun` charge likelihood calculation for each
1442 PMT includes the photoelectron emission contribution from the dark rate of the PMT.
1443 Therefore, the increase in the dark rate needs to be accounted for. In practice, the

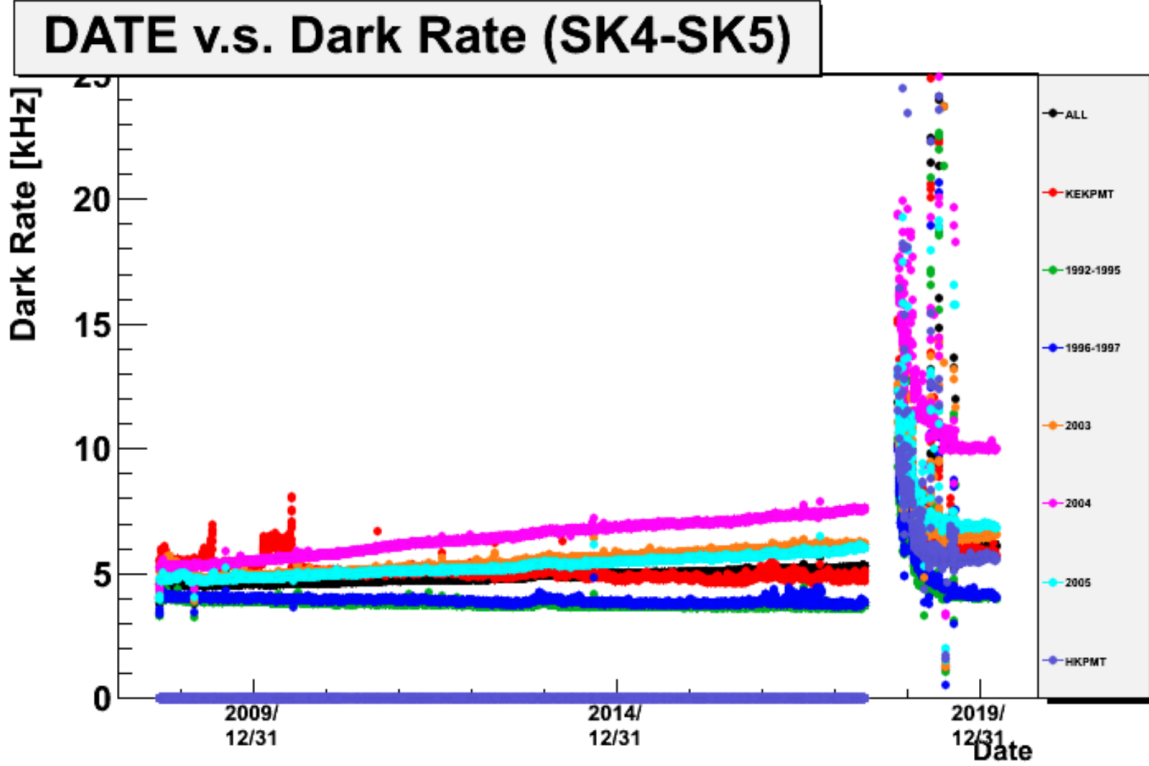


Figure 4.5: The variation of the measured dark rate as a function of date, broken down by PMT type. The SK-IV and SK-V periods span September 2008 to May 2018 and January 2019 to July 2020 respectively. The break in measurement between 2018 corresponds to the period of tank repair and refurbishment. Figure adapted from [174].

reconstruction algorithm takes the average dark rate for all PMTs for each SK period as an input and predicts the associated charge from this contribution. The dark rate was calculated by averaging the dark rate per run for each period separately, using the calibration measurements detailed in subsection 2.1.2. The average dark rate from SK-IV and SK-V were found to be 4.57kHz and 6.30kHz , respectively. The associated charge with the muon and decay electron subevents are illustrated in Figure 4.6. As expected, the increase in dark rate is not observed in the muon subevent which is of typically higher energy. However, it has a clear effect on the decay electron subevent which is lower energy.

The energy scale systematic for the SK-IV period was determined to be 2.1% [176]. It is defined to be equal to the difference between data and Monte Carlo prediction

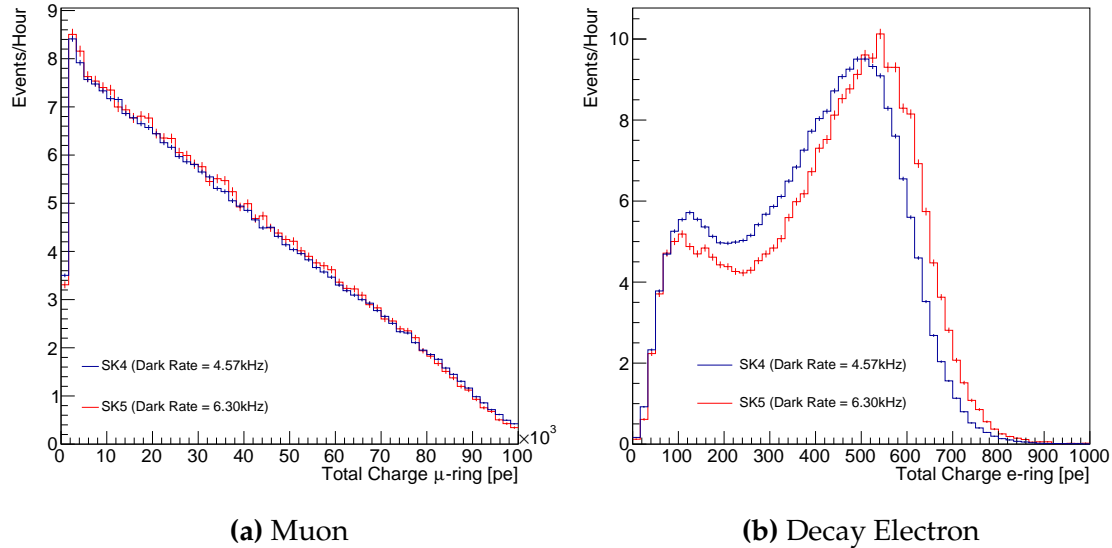


Figure 4.6: Comparison of the measured raw charge deposited per event from the stopping muon data samples between SK-IV (Blue) and SK-V (Red), split by the primary muon subevent and the associated decay electron subevent.

1455 in the stopping muon data sample. To determine the consistency of the SK-IV and
1456 SK-V with respect to the energy scale systematic, the muon momentum distribution
1457 is compared between the two SK periods. The distribution of Cherenkov photons is
1458 dependent upon the momentum of the particle. This is then integrated along the track
1459 length of the particle to determine the PMT hit probability for each PMT. Consequently,
1460 the reconstructed momentum divided by track length is compared between SK-IV and
1461 SK-V as illustrated in Figure 4.7.

The consistency between these distributions has been computed in two ways.

Firstly, a Gaussian is fit to each distribution separately. The mean of which is found to be $(2.272 \pm 0.003)\text{MeV/cm}$ and $(2.267 \pm 0.006)\text{MeV/cm}$ for SK-IV and SK-V respectively. The ratio of these is equal to 1.002 ± 0.003 . The mean of the Gaussian's is consistent with the expected stopping power of a minimum ionising muon for a target material (water) with $Z/A \sim 0.5$ [177]. The second consistency check is performed by introducing a nuisance parameter, α , which modifies the SK-V distribution. The value of α which minimises the χ^2 between the SK-IV and SK-V is determined by

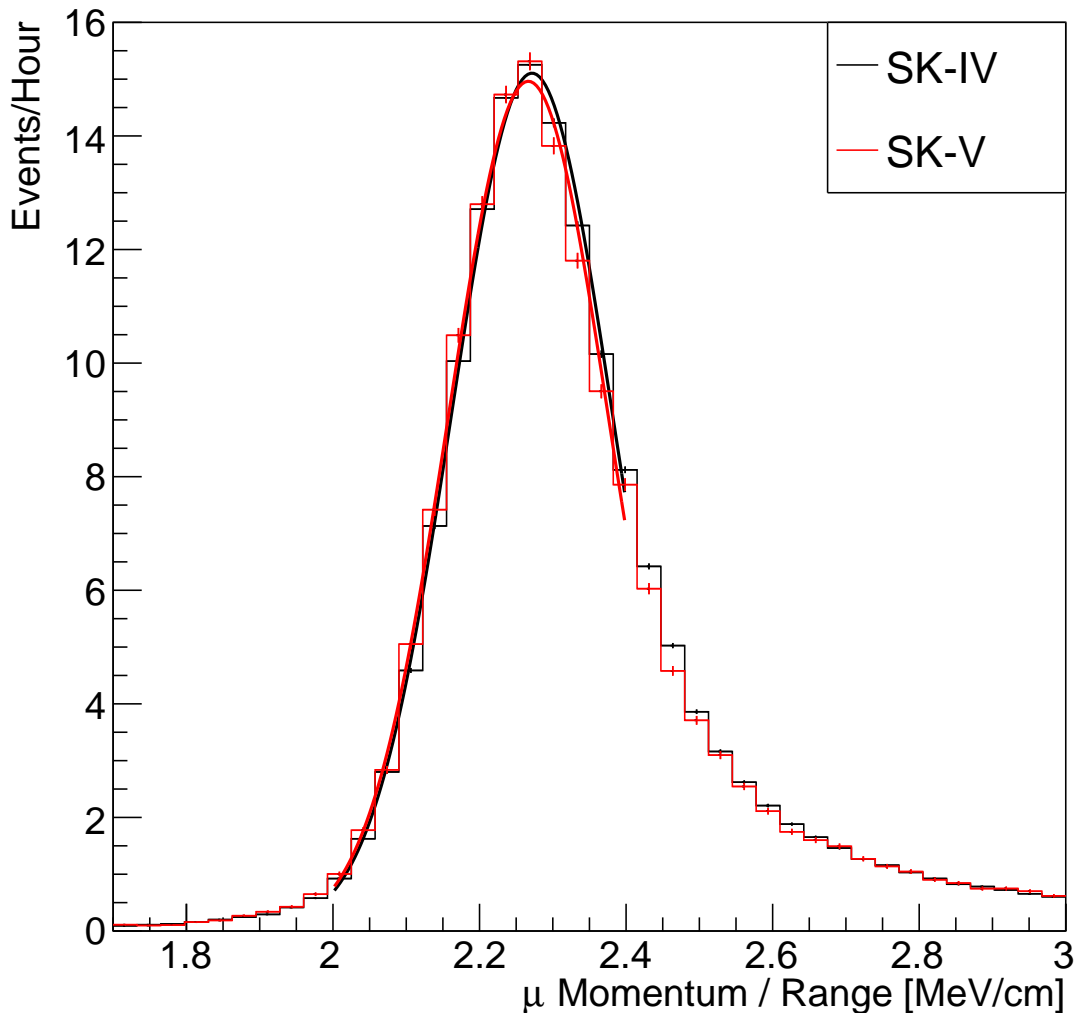


Figure 4.7: The distribution of the reconstructed momentum from the muon ring divided by the distance between the reconstructed muon and decay electron vertices as found in the stopping muon data sets of SK-IV (Black) and SK-IV (Red). Only events with one tagged decay electron and considered. A Gaussian fit is considered in the range [2.0, 2.4] MeV/cm and illustrated as the solid curve.

scanning across a range of values. This is repeated by applying α as a multiplicative factor and an additive shift. The χ^2 distributions for different values of α is illustrated in Figure 4.8. The values which minimise the χ^2 are found to be 0.0052 and 1.0024 for the additive and multiplicative implementations respectively. No evidence of shifts larger than the 2.1% uncertainty on the energy scale systematic has been found in the reconstructed momentum distribution of SK-IV and SK-V.

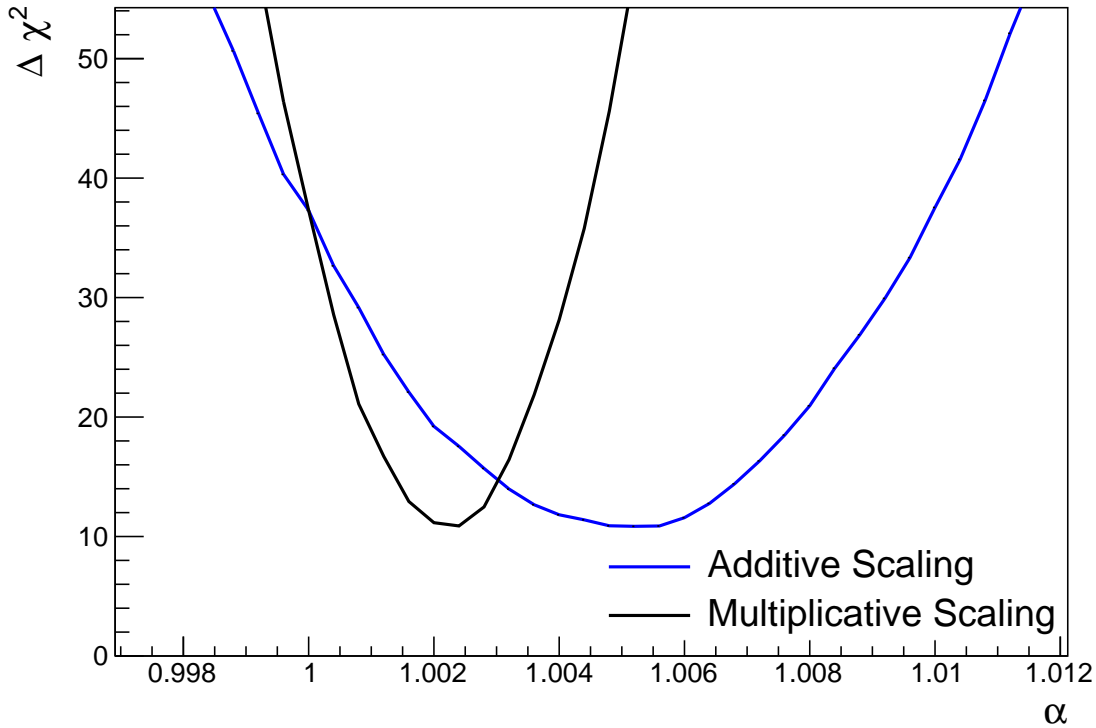


Figure 4.8: The χ^2 difference between the SK-IV and SK-V reconstructed muon momentum divided by range when the SK-V is modified by the scaling parameter α . Both additive (Blue) and multiplicative (Black) scaling factors have been considered. In practice, the additive scaling factor actually uses the value of $(\alpha - 1.0)$.

¹⁴⁷⁶ 4.3 Event Selection at SK

¹⁴⁷⁷ Atmospheric neutrino events observed in the SK detector are categorised into three
¹⁴⁷⁸ different types of samples; fully contained (FC), partially contained (PC) and up-
¹⁴⁷⁹ going muon (Up- μ), using signatures in the inner and outer detector (ID and OD,
¹⁴⁸⁰ respectively). To identify FC neutrino events, it is required that the neutrino interacts
¹⁴⁸¹ inside the fiducial volume of the ID such that no significant OD activity is observed.
¹⁴⁸² For this analysis, an event is defined to be in the fiducial volume providing the
¹⁴⁸³ event vertex is at least 0.5m away from the ID walls. PC events have the same ID
¹⁴⁸⁴ requirements but can have a larger signal present inside the OD. Typically these events
¹⁴⁸⁵ are higher energy muon interactions that penetrate the ID walls. The Up- μ sample

¹⁴⁸⁶ contains events where muons are created in the OD water or rock below the tank
¹⁴⁸⁷ and then propagate upwards through the detector. The reason downward-going
¹⁴⁸⁸ muons generated from neutrino interactions above the tank are neglected is due to
¹⁴⁸⁹ the difficulty in separating their signature from the cosmic muon shower background.
¹⁴⁹⁰ The sample categories are visually depicted in Figure 4.9.

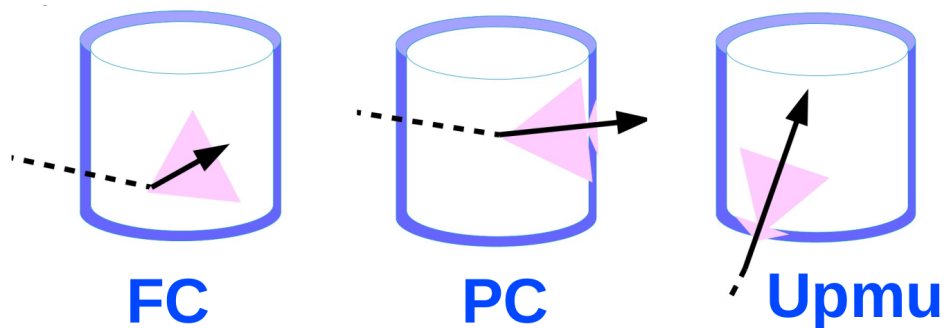


Figure 4.9: A depiction of the topology patterns for fully-contained (FC), partially-contained (PC) and up-going muon ($\text{Up-}\mu$) samples included in this analysis.

¹⁴⁹¹ Based on the event characteristics as defined by the `fitQun` event reconstruction
¹⁴⁹² software, the FC events are further divided up by

- ¹⁴⁹³ • **Visible Energy:** equal to the sum of the reconstructed kinetic energy above the
¹⁴⁹⁴ Cerenkov threshold for all rings present in the event. The purpose is to separate
¹⁴⁹⁵ events into sub-GeV and multi-GeV categories.
- ¹⁴⁹⁶ • **Number of observed Cerenkov rings.** The purpose is to separate single-ring and
¹⁴⁹⁷ multi-ring events, where single-ring events predominantly consist of quasi-elastic
¹⁴⁹⁸ interactions and multi-ring events are resonant pion production or deep inelastic
¹⁴⁹⁹ scattering events.
- ¹⁵⁰⁰ • **Particle identification parameter of the most energetic ring:** A value deter-
¹⁵⁰¹ mined from the maximum likelihood value based on `fitQun`'s electron, muon, or
¹⁵⁰² pion hypothesis. The purpose is to separate electron-like and muon-like events.

- 1503 • **Number of sub-events:** Based on optimised time cuts, this quantity determines
1504 the number of observed decay electrons associated with an event. The main
1505 purpose is to separate quasi-elastic events (which have one decay electron emitted
1506 from the muon decay) and resonant pion production events (which have two
1507 decay electrons emitted from the muon and pion).

1508 The PC and Up- μ categories are broken down into “through-going” and “stopping”
1509 samples depending on whether the muon left the detector. This is because the stopping
1510 events deposited the entire energy of the interaction into the detector, resulting in better
1511 reconstruction. Through-going Up- μ samples are further broken down by whether
1512 any hadronic showering was observed in the event which would be mostly likely due
1513 to DIS interactions. The expected neutrino energy for the different categories is given
1514 in Figure 4.10. FC sub-GeV and multi-GeV events peak around 0.7GeV and 3GeV
1515 respectively, with slightly different peak energies for $\nu_x \rightarrow \nu_e$ and $\nu_x \rightarrow \nu_\mu$. PC and
1516 Up- μ are almost entirely comprised of $\nu_x \rightarrow \nu_\mu$ events and peak around 7GeV and
1517 100GeV respectively.

1518 In data-taking operation, the SK detector observes many background events along-
1519 side the beam and atmospheric neutrino signal events of physics interest. Cosmic
1520 ray muons and flasher events, which is the spontaneous discharge of a given PMTm
1521 contribute the largest amount of background events in the energy range relevant to
1522 oscillation analyses. Lower energy analyses like DSNB searches are also subject to
1523 radioactive backgrounds [178]. Therefore the data recorded is reduced with the aim of
1524 removing these background events. The reduction process is detailed in [46, 83] and
1525 briefly summarised below.

1526 The first two steps in the FC reconstruction remove most cosmic ray muons by
1527 requiring a significant amount of ID activity compared to that measured in the OD.
1528 This is done by counting the total number of photoelectrons recorded in the ID as

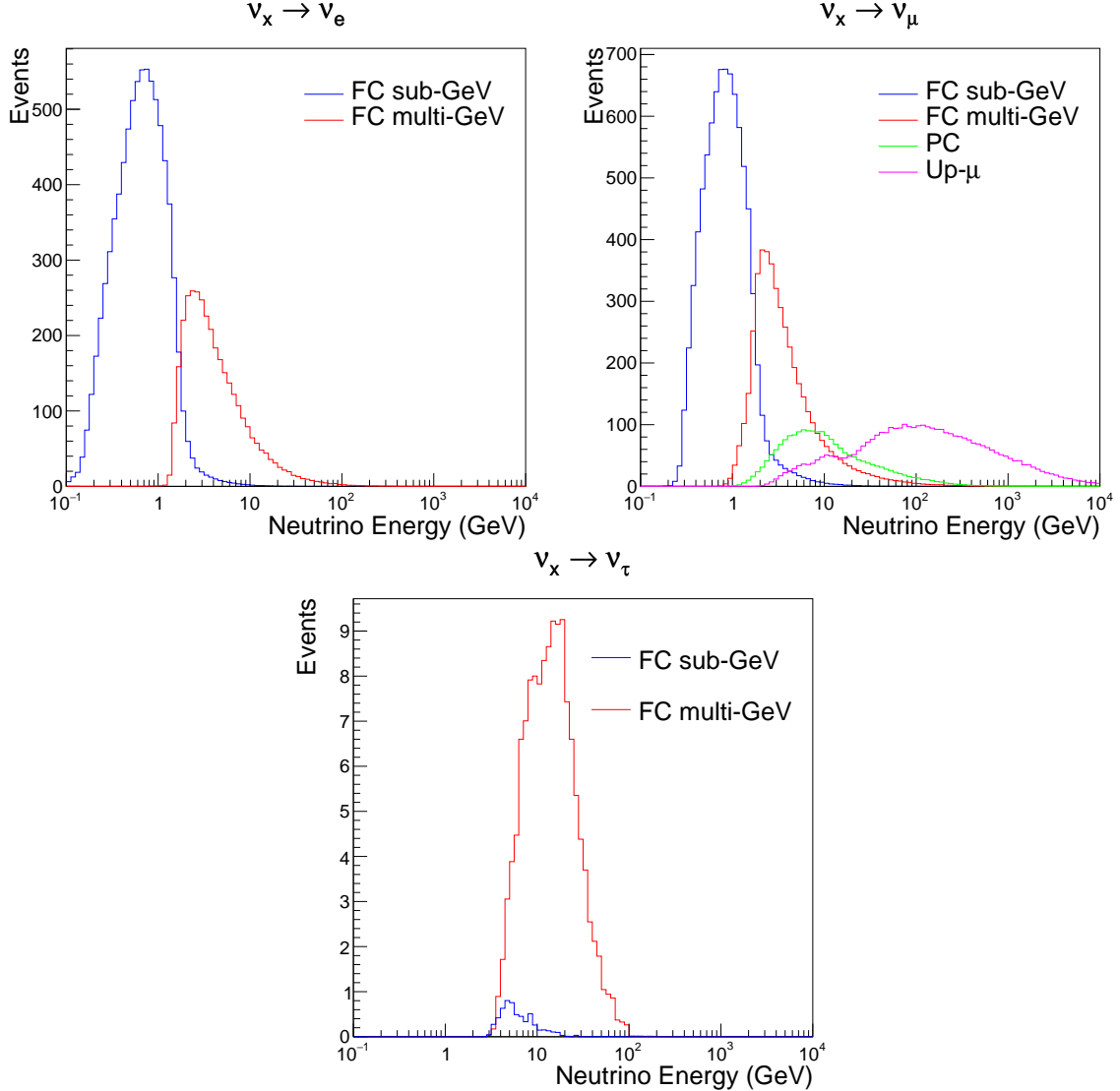


Figure 4.10: The predicted neutrino flux of the fully contained (FC) sub-GeV and multi-GeV, partially contained (PC) and upward-going muon (Up- μ) events. The prediction is broken down by the $\nu_x \rightarrow \nu_e$ prediction (top left), $\nu_x \rightarrow \nu_\mu$ prediction (top right) and $\nu_x \rightarrow \nu_\tau$ prediction (bottom). All systematic dials are set to their nominal values and the Asimov A oscillation parameters are assumed.

well as the number of hits in the OD. A third reduction step is then applied to select cosmic-ray muons that pass the initial reduction. These are typically high momentum muons or events which leave only a small number of hits in the OD. A purpose-built cosmic muon fitter is used to determine the entrance (or exit) position of the muon from the OD and a cut is applied to OD activity contained within 8m of this position. Flasher events are removed in the fourth reduction step which is based on the close

1535 proximity of PMT hits surrounding the PMT producing the flash. Events that pass the
1536 reduction stage to this point are reconstructed using the more accurate APFit algorithm
1537 and the fifth step of the reduction uses the information from this more accurate fitter
1538 to repeat the third and fourth reduction steps using tighter cuts. This particularly
1539 targets invisible muons which are below the Cherenkov threshold resulting in no
1540 OD activity but whose decay electrons generate light inside the ID. The final cuts
1541 require the event vertex to be within the fiducial volume (0.5m from the wall although
1542 the nominal distance is 2.0m), visible energy $E_{vis} > 30\text{MeV}$ and fewer than 16 hits
1543 within the higher energy OD cluster. The culmination of the fully contained reduction
1544 results in 8.09 events/day in the nominal fiducial volume [179]. The uncertainty in the
1545 reconstruction is calculated by comparing Monte Carlo prediction to data. The largest
1546 discrepancy is found to be 1.3% in the fourth reduction step.

1547 The PC and Up- μ events are also processed through their own reduction processes
1548 detailed in [46]. Both of these samples are reconstructed with the APFit algorithm
1549 rather than `fiTQun`. This is because the efficiency of reconstructing events that leave
1550 the detector has not been sufficiently studied for reliable systematic uncertainties. 0.66
1551 and 1.44 events/day are found after the final step of reduction for the PC and Up- μ
1552 samples respectively.

₁₅₅₃ **Chapter 5**

₁₅₅₄ **Oscillation Probability Calculation**

₁₅₅₅ The calculation of the oscillation probability is crucial to the reliability of the sensitivity
₁₅₅₆ measurements of the analysis presented within this thesis. Firstly, it is important to
₁₅₅₇ understand how and where the sensitivity to the oscillation parameters comes from
₁₅₅₈ for both atmospheric and beam samples. An overview of how these sets of samples
₁₅₅₉ observe changes in δ_{CP} , Δm_{23}^2 , and $\sin^2(\theta_{23})$ as well as how the atmospheric samples
₁₅₆₀ have an increased sensitivity to mass hierarchy determination is given in section 5.1.
₁₅₆₁ It also explains the additional complexities involved when including atmospheric
₁₅₆₂ neutrinos as compared to a beam-only analysis.

₁₅₆₃ Without additional techniques, atmospheric sub-GeV upward-going neutrinos can
₁₅₆₄ artificially inflate the sensitivity to δ_{CP} due to the quickly varying oscillation probabil-
₁₅₆₅ ity in this region. Therefore, a “sub-sampling” approach has been developed to reduce
₁₅₆₆ these biases ensuring accurate and reliable sensitivity measurements. This technique
₁₅₆₇ ensures that small-scale unresolvable features of the oscillation probability have been
₁₅₆₈ averaged over whilst the large-scale resolvable features in the oscillation probability
₁₅₆₉ have been kept. The documentation of this technique is found in section 5.2 alongside
₁₅₇₀ the validation of the choices which have been made. The CUDAProb3 implementation
₁₅₇₁ choice made within the fitting framework, as detailed in section 5.3, ensures that the
₁₅₇₂ analysis can be done in a timely manner.

₁₅₇₃ Whilst the beam neutrinos are assumed to propagate through a constant density
₁₅₇₄ slab of material, the density variations through the Earth result in more complex
₁₅₇₅ oscillation patterns Furthermore, the uncertainty in the electron density can modify

1576 the oscillation probability for the denser core layers of the Earth. section 5.4 details
1577 the model of the Earth used within this analysis. This includes the official SK-only
1578 methodology as well as relatively straightforward improvements that can be made to
1579 more closely approximate the PREM model. Another quirk of atmospheric neutrinos
1580 oscillation studies is that the height of production in the atmosphere is not known
1581 on an event-by-event analysis. An analytical averaging technique that approximates
1582 the uncertainty of the oscillation probability has been followed, with the author of
1583 this thesis being responsible for the implementation and validation. This technique is
1584 illustrated in section 5.5 alongside the variation in oscillation probability which would
1585 be an expected effect in the down-going and horizontal-going neutrinos.

1586 5.1 Overview

1587 The analysis presented within this thesis focuses on the determination of oscillation
1588 parameters from atmospheric and beam neutrinos. Whilst subject to the same oscil-
1589 lation probability, the way in which the two sets of samples have sensitivity to the
1590 different oscillation parameters differs quite significantly.

1591 Atmospheric neutrinos have a varying baseline, or “path length”, such that the
1592 distance each neutrino travels before interacting is dependent upon the zenith angle.
1593 Therefore the oscillation probability can be represented as a two-dimensional “oscillo-
1594 gram” as shown in Figure 5.1. For this calculation, four layers of fixed density were
1595 used to model the Earth with values taken from an approximation of the PREM model.
1596 These can be seen in the distinct discontinuities in the oscillogram as a function of the
1597 zenith angle.

1598 Another complexity of atmospheric neutrino oscillation probability calculation is
1599 the uncertainty in the height at which a neutrino was produced, termed the “produc-

tion height". Primary cosmic rays, which contribute most of the neutrino flux, can interact anywhere between the Earth's surface and ~ 50 km above that. The baseline, L , for a neutrino generated with zenith angle, θ , and production height, h , can be calculated as

$$L = \sqrt{(R_E + h)^2 - R_E^2 (1 - \cos^2(\theta))} - R_E \cos(\theta), \quad (5.1)$$

where $R_E = 6,371$ km is the Earth's radius.

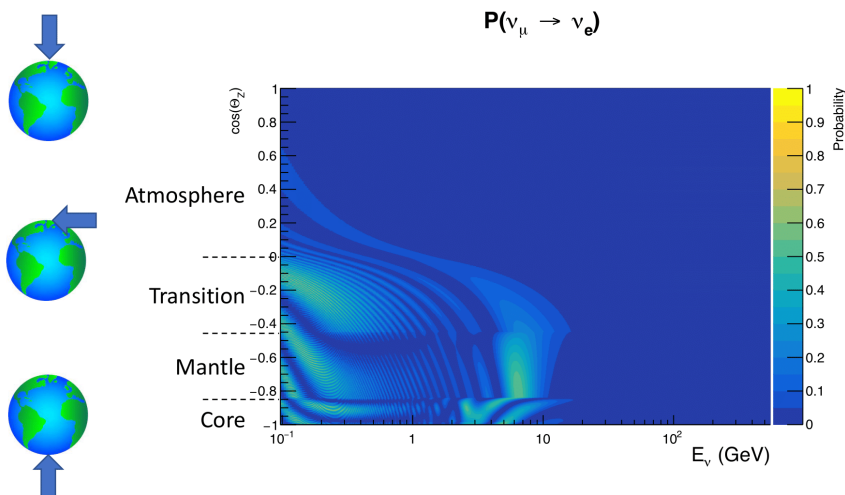


Figure 5.1: An "Oscillogram" that depicts the $P(\nu_\mu \rightarrow \nu_e)$ oscillation probability as a function of neutrino energy and cosine of the zenith angle. The zenith angle is defined such that $\cos(\theta_Z) = 1.0$ represents neutrinos that travel from directly above the detector. The four-layer constant density PREM model approximation is used and Asimov A oscillation parameters are assumed.

Atmospheric neutrinos do have some sensitivity to δ_{CP} through a normalisation term. Figure 5.2 illustrates the difference in oscillation probability between CP-conserving and CP-violating δ_{CP} values. The result is a complicated oscillation pattern in the appearance probability for sub-GeV upgoing neutrinos. The detector does not have sufficient resolution to resolve these individual patterns so the sensi-

tivity to δ_{CP} for atmospheric neutrinos comes via the overall normalisation of the
 sub-GeV upgoing events. The presence of matter means that the effect δ_{CP} has on
 the oscillation probability is not equal between neutrinos and antineutrinos which
 would be expected when propagating through a vacuum. This is further extenuated
 by the fact that SK can not distinguish neutrinos and antineutrinos well and that the
 cross-section neutrino interaction is larger than that for antineutrinos. Finally, sample
 selections (discussed in [DB: Link to selection chapter](#)) targeting different neutrino
 interaction modes (charge current quasi-elastic and single pion production) result in
 an imbalance in the percentage of neutrinos to anti-neutrinos in these samples due
 to pion capture. Negatively charged pions from antineutrino interactions are more
 likely to be captured by a nucleus compared to a positively charged pion emitted from
 a neutrino interaction. This all culminates in atmospheric neutrinos having a very
 complex sensitivity to δ_{CP} .

Atmospheric neutrinos are subject to matter effects as they travel through the dense
 matter in the Earth. The vacuum and matter oscillation probabilities for $P(\nu_e \rightarrow \nu_e)$
 and $P(\bar{\nu}_e \rightarrow \bar{\nu}_e)$ are presented in Figure 5.3. The oscillation probability for both neutrinos
 and antineutrinos are affected in the presence of matter but the resonance (Effects
 around $E_\nu \sim 5\text{GeV}$) only occurs for neutrinos in normal mass hierarchy and antineu-
 trinos for inverse mass ordering. The exact position and amplitude of the resonance
 depend on $\sin^2(\theta_{23})$ meaning that the atmospheric neutrinos have sensitivity to the
 octant of θ_{23} .

As the T2K beam flux is centered at the first oscillation maximum, the sensitivity
 to δ_{CP} is predominantly observed as a change in the event-rate of e-like samples in
 $\nu/\bar{\nu}$ modes. Figure 5.4 illustrates the $P(\nu_\mu \rightarrow \nu_e)$ oscillation probability for a range
 of δ_{CP} values. A circular modulation of the oscillation peak (in both magnitude and
 position) is observed when varying throughout the allowable values of δ_{CP} . The CP-

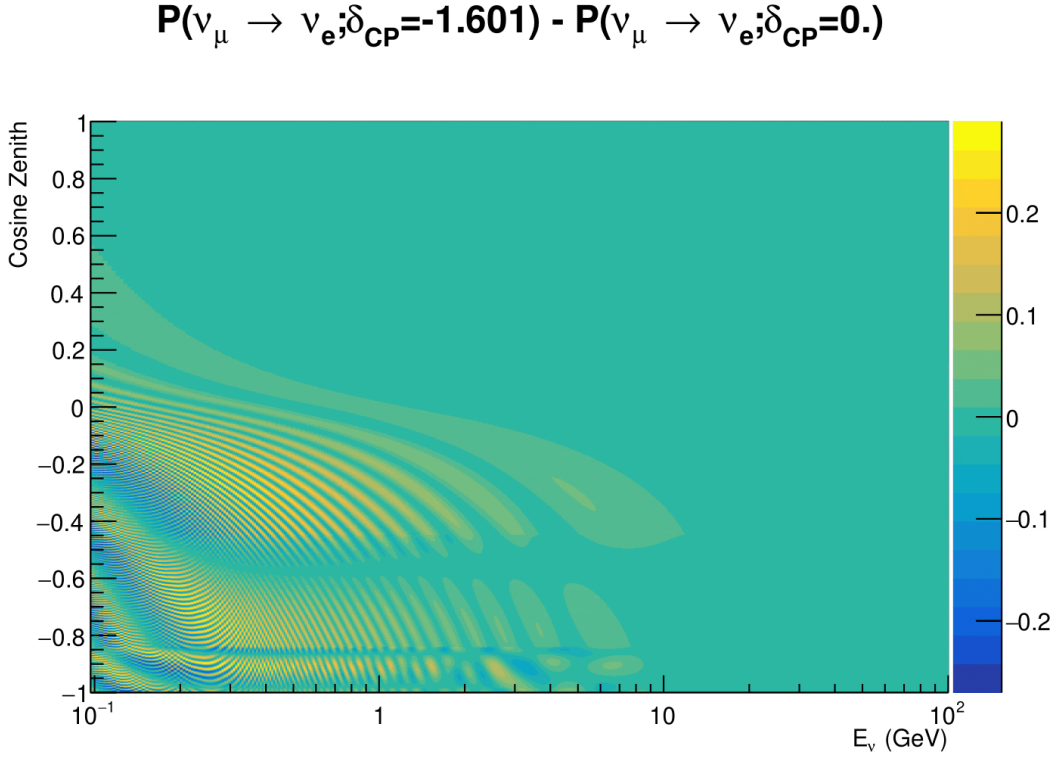


Figure 5.2: The effect of δ_{CP} for atmospheric neutrinos given in terms of the neutrino energy and zenith angle. The oscillogram compares the $P(\nu_\mu \rightarrow \nu_e)$ oscillation probability for a CP conserving ($\delta_{CP} = 0.0$) and CP violating ($\delta_{CP} = -1.601$) value of δ_{CP} . The other oscillation parameters assume the “Asimov A” oscillation parameter set given in Table 5.1.

1636 conserving values of $\delta_{CP} = 0, \pi$ have a lower(higher) oscillation maximum than the
 1637 CP-violating values of $\delta_{CP} = -\pi/2 (\delta_{CP} = \pi/2)$ leading to a $\sin(\delta_{CP})$ type sensitivity.
 1638 A sub-dominant shift in the energy of the oscillation peak is also present to aid in
 1639 separating the two CP-conserving values of δ_{CP} .

1640 T2K’s sensitivity to the atmospheric oscillation parameters is more of a shape-
 1641 based variation of the muon-like samples, as illustrated in Figure 5.4. The value of
 1642 Δm_{32}^2 laterally shifts the position of the oscillation dip (around $E_\nu \sim 0.6$ GeV) in the
 1643 $P(\nu_\mu \rightarrow \nu_\mu)$ oscillation probability. A variation of $\sin^2(\theta_{23})$ is predominantly observed
 1644 as a vertical shift of the oscillation dip with second-order horizontal shifts being due
 1645 to matter effects. The beam neutrinos have limited sensitivity to matter effects due

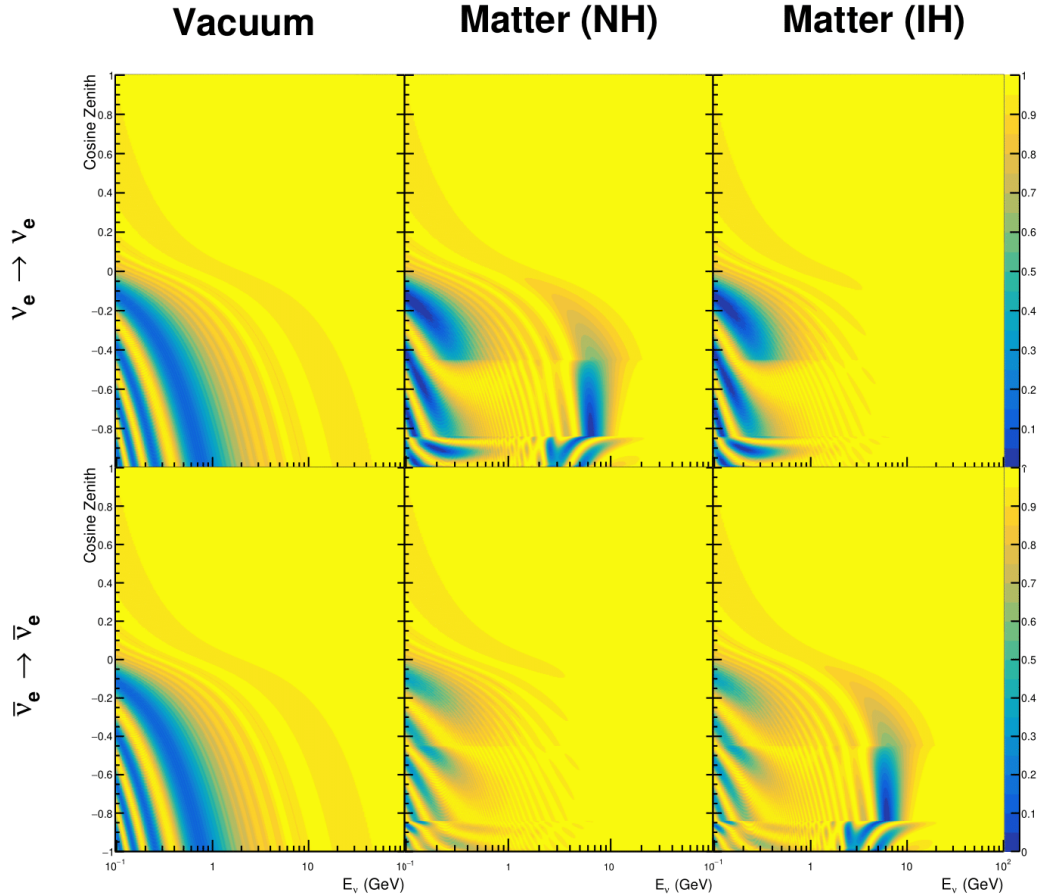


Figure 5.3: An illustration of the matter-induced effects on the oscillation probability, given as a function of neutrino energy and zenith angle. The top row of panels gives the $P(\nu_e \rightarrow \nu_e)$ oscillation probability and the bottom row illustrates the $P(\bar{\nu}_e \rightarrow \bar{\nu}_e)$ oscillation probability. The left column highlights the oscillation probability in a vacuum, whereas the middle and right column represents the oscillation probabilities when the four layer fixed density PREM model is assumed. All oscillation probabilities assume the “Asimov A” set given in Table 5.1, but importantly, the right column sets an inverted mass hierarchy. The “matter resonance” effects at $E_\nu \sim 5\text{GeV}$ can be seen in the $P(\nu_e \rightarrow \nu_e)$ for normal mass hierarchy and $P(\bar{\nu}_e \rightarrow \bar{\nu}_e)$ for inverted hierarchy.

to the shorter baseline as well as the Earth’s mantle is relatively low-density material
 (as compared to the Earth’s core). For some values of δ_{CP} , the degeneracy in the number of e-like events allows the mass hierarchy to be resolved. This leads to a δ_{CP} -dependent mass hierarchy sensitivity which can be seen in Figure 5.5.
 1646 to the shorter baseline as well as the Earth’s mantle is relatively low-density material
 1647 (as compared to the Earth’s core). For some values of δ_{CP} , the degeneracy in the
 1648 number of e-like events allows the mass hierarchy to be resolved. This leads to a δ_{CP}
 1649 -dependent mass hierarchy sensitivity which can be seen in Figure 5.5.

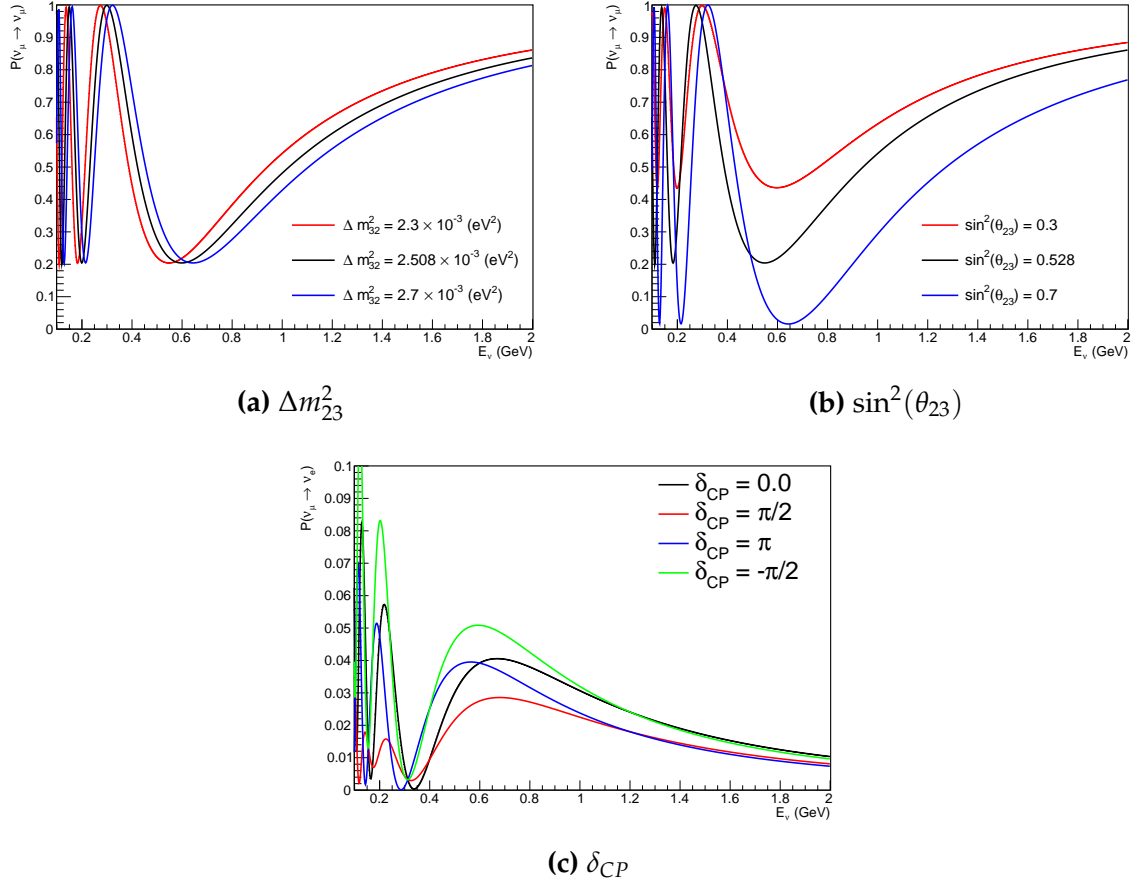


Figure 5.4: The oscillation probability for beam neutrino events given as a function of neutrino energy. All oscillation parameters assume the “Asimov A” set given in Table 5.1 unless otherwise stated. Each panel represents a change in one of the oscillation parameters whilst keeping the remaining parameters fixed.

Whilst all oscillation channels should be included for completeness, the computational resources required to run a fit are limited and any reasonable approximations which reduce the number of oscillation probability calculations that need to be made should be applied. The $\nu_e \rightarrow \nu_{e,\mu,\tau}$ (and antineutrino equivalent) oscillations can be ignored for beam neutrinos as the $\nu_e/\bar{\nu}_e$ fluxes being approximately two orders of magnitude smaller than the corresponding $\nu_\mu/\bar{\nu}_\mu$ flux. Furthermore, as the peak neutrino energy of the beam is well below the threshold for τ production ($E_\nu \sim 3\text{GeV}$ [180]) only a small proportion of the neutrinos produced in the beam have the required energy. For the few neutrinos that have sufficient energy, the oscillation probability is very small due to the short baseline. Whilst these approximations can be made for the

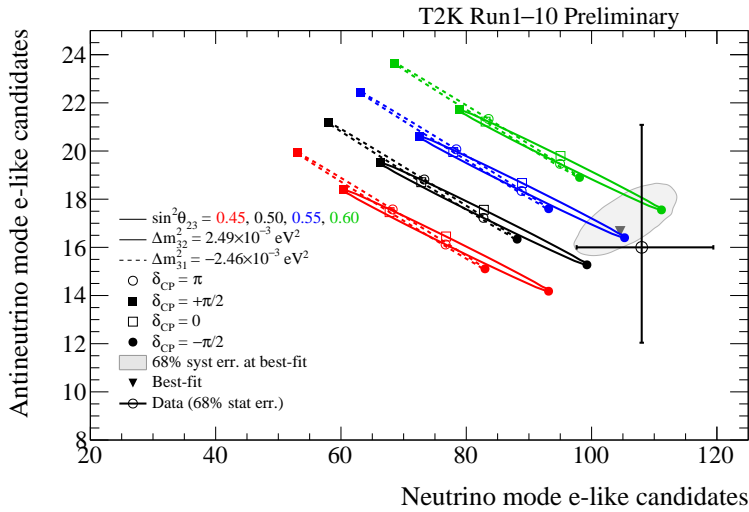


Figure 5.5: The number of electron-like events in the FHC and RHC operating mode of the beam, as a function of the oscillation probabilities. Both normal hierarchy (Solid) and inverse hierarchy (Dashed) values of Δm_{23}^2 are given.

beam neutrinos, the atmospheric flux of ν_e is of the same order of magnitude as the ν_μ flux and the energy distribution of atmospheric neutrinos extends well above the tau production threshold.

Throughout this thesis, several spectra predictions, Asimov fits, and contour comparisons are presented which require oscillation parameters to be assumed. Table 5.1 defines two sets of oscillation parameters, with “Asimov A” set being close to the preferred values from a previous T2K-only fit [181] and “Asimov B” being CP-conserving and further from maximal θ_{23} mixing.

Parameter	Asimov A	Asimov B
Δm_{12}^2	$7.53 \times 10^{-5} \text{ eV}^2$	
Δm_{32}^2	$2.509 \times 10^{-3} \text{ eV}^2$	
$\sin^2(\theta_{12})$	0.304	
$\sin^2(\theta_{13})$	0.0219	
$\sin^2(\theta_{23})$	0.528	0.45
δ_{CP}	-1.601	0.0

Table 5.1: Reference values of the neutrino oscillation parameters for two different oscillation parameter sets.

1668 5.2 Treatment of Fast Oscillations

1669 As shown in Figure 5.6, atmospheric neutrino oscillations have a significantly more
1670 complex structure for upgoing neutrinos with energy below 1GeV. This is because the
1671 L/E dependence of the oscillation probability in this region induces rapid variations
1672 for small changes in L or E . As discussed in section 5.1, this is also the region in which
1673 atmospheric neutrinos have sensitivity to δ_{CP} . In practice, the direction between
1674 the detector and a neutrino's production vertex is inferred from the direction of any
1675 secondary particles created in the detector target. For low-energy neutrinos, this
1676 inference can be rather poor and introduces a distinct difference to beam neutrinos
1677 where the direction to production vertex is very well known.

1678 As a consequence of the poor detector resolution, an average oscillation probability
1679 is observed in this region. This creates a computational problem as a significantly
1680 large amount of MC statistics would be required to accurately predict the number
1681 of events in each bin if MC averaging was the only technique used. This section
1682 describes the ‘sub-sampling’ approach developed for this analysis and compares it to
1683 the methodology used within the SK-only analysis.

1684 The official SK-only analysis uses the osc3++ oscillation parameter fitter [182]. To
1685 perform the fast oscillation averaging, it uses a ‘nearest-neighbour’ technique. For a
1686 given neutrino MC event, the nearest neighbours in reconstructed lepton momentum
1687 and zenith angle are found and a distribution of neutrino energies is built. This
1688 distribution is then used to compute an average oscillation probability for the given
1689 neutrino MC event.

1690 For the i^{th} event, the oscillation weight is calculated as

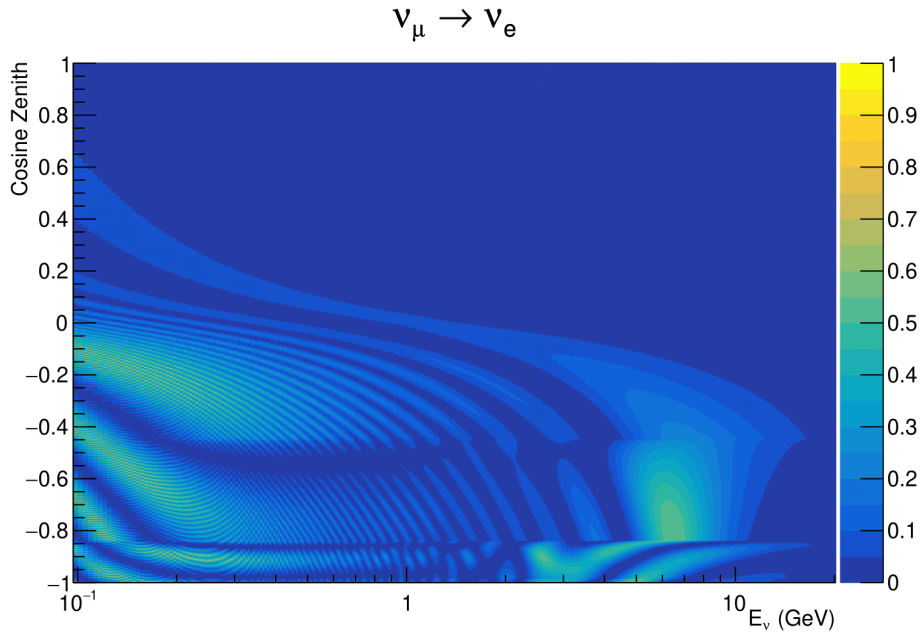


Figure 5.6: The oscillation probability $P(\nu_\mu \rightarrow \nu_e)$, given as a function of neutrino energy and zenith angle, which highlights an example of the “fast” oscillations in the sub-GeV upgoing region.

$$W_i = \frac{1}{5}P(E_i, \bar{L}_i) + \frac{1}{5} \sum_{\beta=-1,-0.5,0.5,1} P(E_i + \beta\sigma_i, L_\beta), \quad (5.2)$$

where $P(E, L)$ is the oscillation probability calculation for neutrino energy E and path length L , σ_i is the RMS of the energy distribution for the given event, and the two path lengths, \bar{L}_i and L_β are discussed below. In practice, twenty of the nearest neighbours are used to generate the neutrino energy distribution. All of the oscillation probability calculations are performed with a fixed zenith angle (and therefore have same matter density profile).

The uncertainty in the production height is controlled by using an “average” production height. \bar{L}_i represents the average path length computed using twenty production heights taken from the Honda flux model’s prediction [44] for a fixed zenith angle, where the production heights are sampled in steps of 5% of their cumulative

1701 distribution function. L_β values are similarly calculated but instead use different
1702 combinations of four production heights (sampled in the same way),

$$\begin{aligned} L_{-1.0} &= \frac{1}{4}L(45, 50, 55, 60), \\ L_{-0.5} &= \frac{1}{4}L(35, 40, 65, 70), \\ L_{+0.5} &= \frac{1}{4}L(25, 30, 75, 68), \\ L_{+1.0} &= \frac{1}{4}L(15, 20, 85, 89). \end{aligned} \tag{5.3}$$

1703 This averaging works well because of the correlation between the true neutrino
1704 zenith angle and the inferred direction from secondary particles in the detector. For
1705 low-energy neutrinos, where the resolution of the true neutrino direction is poor, σ_i
1706 will be large, resulting in significant averaging effects. Contrary to this, the inferred
1707 direction of high-energy neutrinos will be much closer to the true value, meaning that
1708 σ_i will be smaller.

1709 In practice, this technique is performed before the fit in order to deal with the
1710 computational cost. Oscillation probabilities are pre-calculated on a 4D grid. This
1711 is possible as the Osc3++ framework uses binned oscillation parameters rather than
1712 continuous so the oscillation parameters used in the fit are known prior to run-time.
1713 The framework used in the analysis presented within this thesis uses continuous
1714 oscillation parameters. Due to the MCMC technique invoked within the fitter (see
1715 chapter 3), there is no way to know which oscillation parameter values will be selected
1716 in each step at run-time. Therefore, the oscillation parameter calculation would have
1717 to be performed at run-time which is very expensive for event-by-event reweighting.
1718 Having to compute five oscillation probabilities per event would require far too many

1719 computational resources to be viable so the SK technique can not be used within this
1720 analysis. However, the concept of the averaging technique can be taken from it.

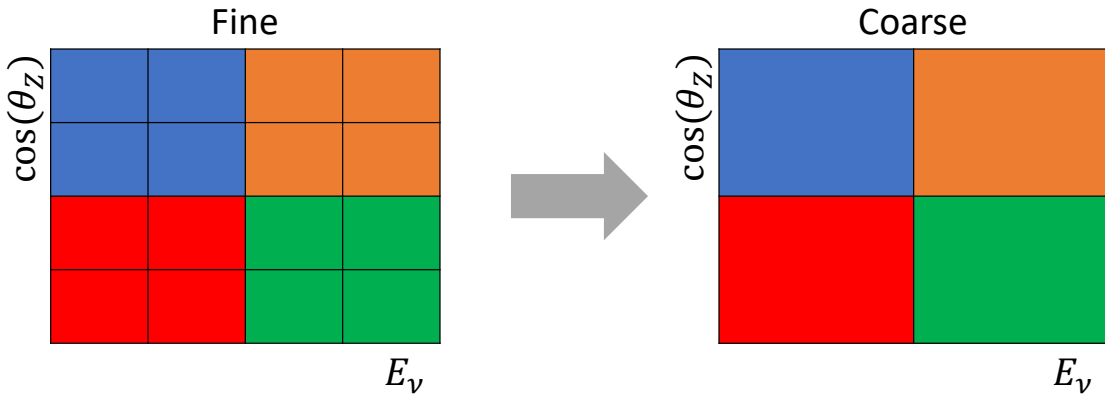


Figure 5.7: Illustration of the averaging procedure for $N = 2$. The oscillation probabilities calculated on the finer left binning are averaged to obtain the oscillation probabilities in the coarser right binning. These averaged oscillation probabilities with the coarser binning are then applied to each event during the fit.

1721 This analysis uses a binned oscillogram in which oscillation probabilities for a given
1722 event are selected based on that event's attributes. To perform a similar averaging as
1723 the SK analysis, a sub-sampling approach has been devised. The technique can be
1724 explained by considering a "fine" and "coarse" oscillogram. The fine oscillograms
1725 are used to define the array of cosine zeniths and energies for the neutrino oscillation
1726 engine. The coarse oscillograms cover the same phase-space as the fine oscillograms
1727 but have fewer bins in that range. Then, for a given coarse oscillogram bin, the value
1728 of that bin will be taken as the average of all the oscillation probabilities of all the fine
1729 oscillogram bins which fall into that coarse oscillogram bin.

1730 The binning which is used to calculate the oscillation probabilities, known as the
1731 'fine' binning, has $N \times N$ subdivisions per coarse bin. The value assigned to a coarse
1732 bin is the linear average (flat prior in E_ν and $\cos(\theta_Z)$) of all the oscillation probabilities
1733 calculated at the center of each fine bin contained within that coarse bin. Figure 5.7
1734 illustrates the $N = 2$ example where the assigned value to a coarse bin is the linear

1735 average of the four fine bins which fall in that coarse bin. Whilst the coarse bin edges
1736 are not linear on either axis, the sub-division of the fine bins is linear over the range
1737 of a coarse bin. The alignment of the fine and coarse binning edges is checked at
1738 run-time.

1739 The coarse binning is defined with 67×52 bins in true neutrino energy \times cosine
1740 zenith. In general, the binning is logarithmically spaced in neutrino energy but has
1741 some hand-picked bin edges. Firstly, the bin density around the matter resonance is
1742 smoothly increased around the matter resonance region. This is to avoid smearing
1743 this region which can be well sampled by the Monte Carlo. Secondly, bin edges
1744 are selected to hit $0.4, 0.6, 1, 10, 30, 50, 100\text{GeV}$. This is to ensure that the Coloumb
1745 correction systematic and the atmospheric flux systematics definitions in neutrino
1746 energy can be hit. The cosine zenith binning is approximately linearly spaced across
1747 the allowable range but the values of layer transitions are hit precisely; -0.8376
1748 (core-mantle) and -0.4464 (mantle/transition zone). Bins are spread further apart for
1749 downgoing events as this is a region unaffected by the fast oscillation wavelengths
1750 and reduces the total number of calculations required to perform the reweight (Not
1751 the number required to perform the oscillation calculation).

1752 The choice of N is justified based on two studies. Firstly, the variation of event
1753 rates of each sample is studied as a function of the number of subdivisions. For
1754 a given set of oscillation parameters thrown from the PDG prior constraints, the
1755 oscillation probabilities are calculated using a given value of N . Each sample is re-
1756 weighted and the event rate is stored. The value of N is scanned from 1, which
1757 corresponds to no averaging, to 24, which corresponds to the largest computationally
1758 viable subdivision binning. The event rate of each sample at large N is expected to
1759 converge to a stationary value due to the fine binning fully sampling the small-scale

1760 structure. Figure 5.8 illustrates this behaviour for the SubGeV_elike_0dcy sample for
 1761 30 different throws of the oscillation parameters.

SubGeV-elike-0dcy

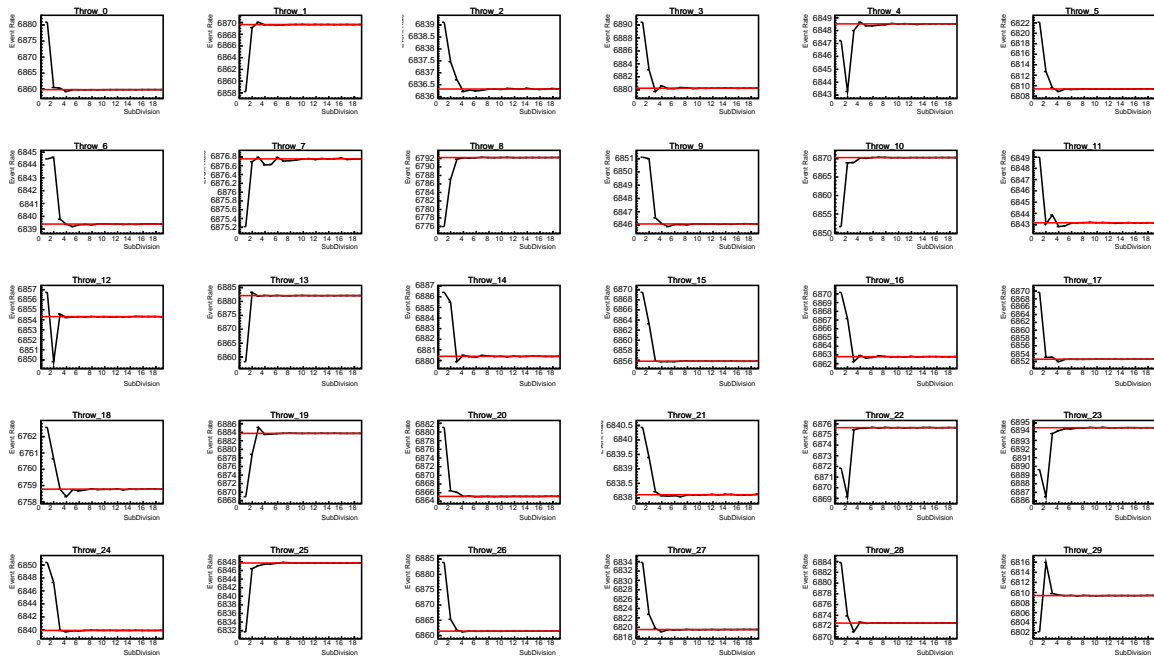


Figure 5.8: Event rate of the SubGeV_elike_0dcy sample as a function of the number of subdivisions per coarse bin. Each subplot represents the event rate of the sample at a different oscillation parameter set (thrown from the PDG priors). The red line in each subplot represents the mean of the event rate over the different values of sub-divisions for that particular oscillation parameter throw.

1762 Denoting the event rate for one sample for a given throw t at each N by $\lambda_t^{(N)}$, the
 1763 average over all considered N values ($\bar{\lambda}_t = \frac{1}{24} \sum_{N=1}^{24} \lambda_t^{(N)}$) is computed. The variance
 1764 in the event rate at each N is then calculated from

$$\text{Var}[\lambda^{(N)}] = \frac{1}{N_{\text{throws}}} \sum_{t=1}^{N_{\text{throws}}} \left(\lambda_t^{(N)} - \bar{\lambda}_t \right)^2 - \left[\frac{1}{N_{\text{throws}}} \sum_{t=1}^{N_{\text{throws}}} \left(\lambda_t^{(N)} - \bar{\lambda}_t \right) \right]^2. \quad (5.4)$$

The aim of the study is to find the lowest value of N such that this variance is below 0.001. This is the typical threshold used by T2K fitters to validate systematic implementation so is just as applicable to the oscillation probability calculation. The results of this study for each atmospheric sample used within this thesis are illustrated in Figure 5.9 for 2000 throws of the oscillation parameters. As can be seen, the variance is below the threshold at $N = 10$, and is driven primarily by the SubGeV_mulike_1dcy and SubGeV_elike_0dcy selections.

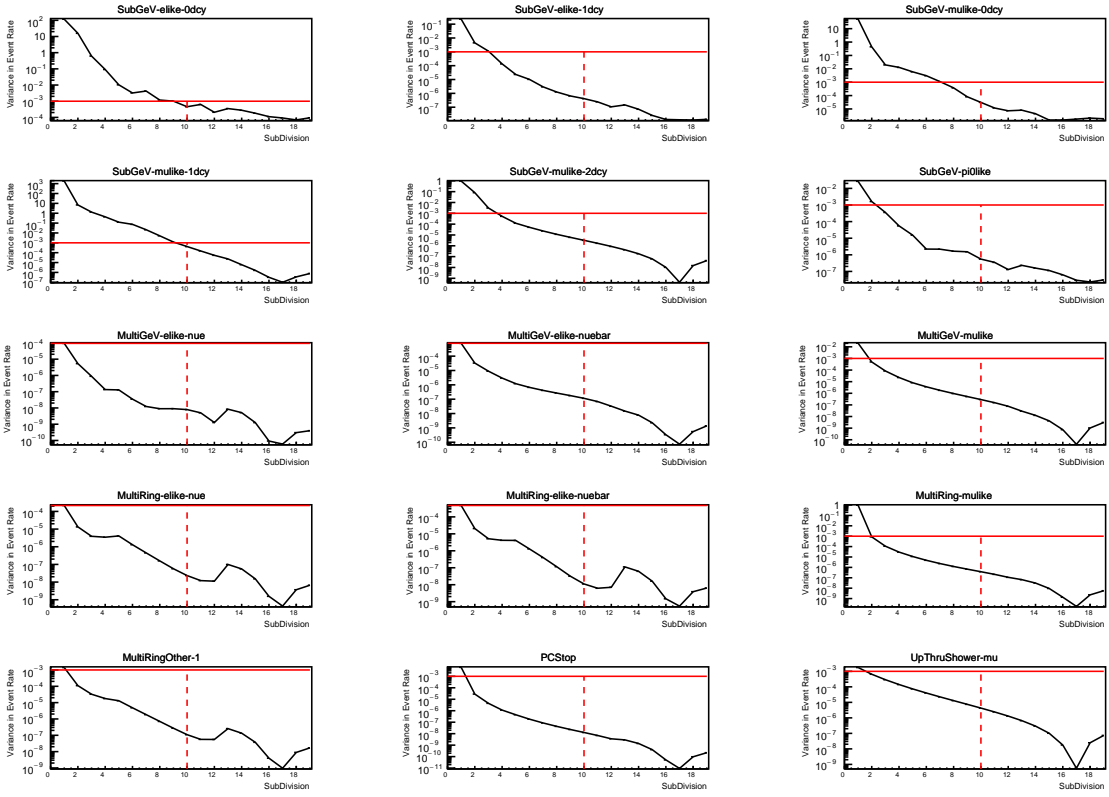


Figure 5.9: Variance of event rate for each atmospheric sample as a function of the number of sub-divisions per coarse bin. The solid red line indicates the 0.1% threshold and the dashed red line is a graphical indication of the variance at a sub-division $N = 10$.

The second study to determine the value of N is as follows. The likelihood for each sample is computed against an Asimov data set created with oscillation parameters from “Asimov A” in Table 5.1. Following Equation 5.4, the variance of the log-likelihood over all considered N is computed. The results are shown in Figure 5.10.

1776 This tests the impact of the averaging on each sample's binning by reconstructed
 1777 momentum and/or zenith angle and also provides a scale for the calculation errors
 1778 compared to their statistical uncertainties.

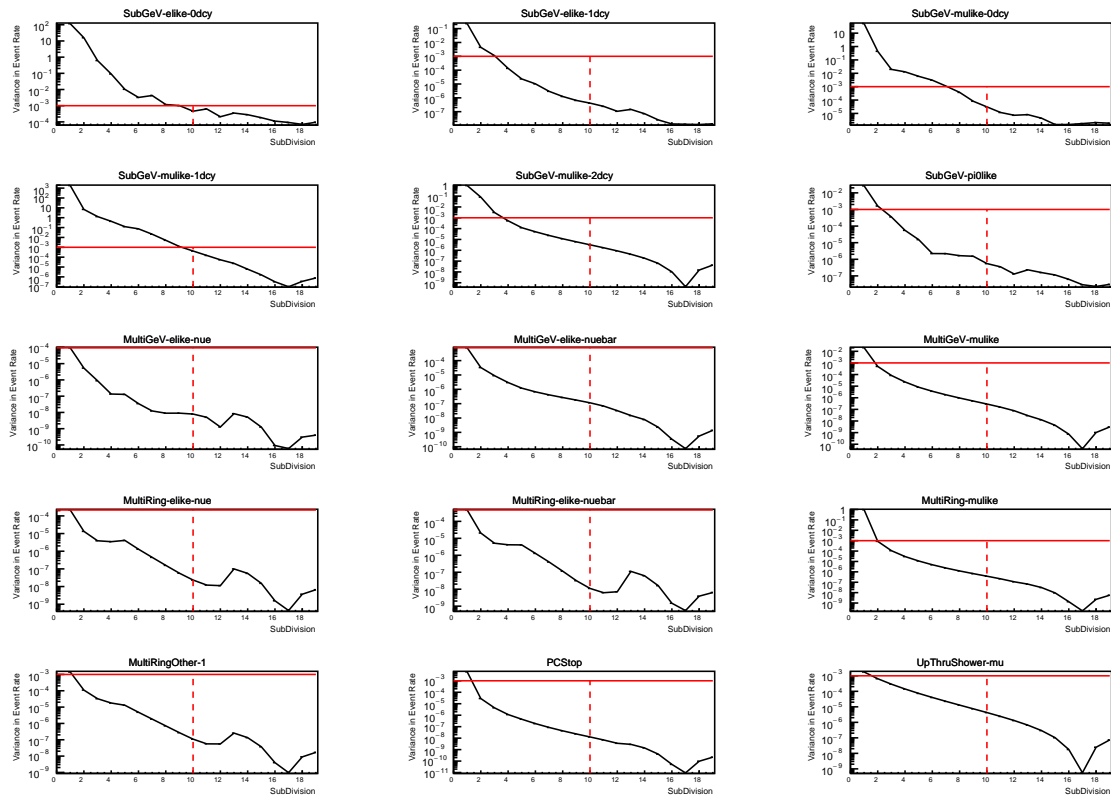


Figure 5.10: Variance of sample likelihood, when compared to 'Asimov data' set at Asimov A, for each atmospheric sample as a function of the number of sub-divisions per coarse bin. The solid red line indicates the 0.1% threshold and the dashed red line is a graphical indication of the variance at a sub-division $N = 10$.

1779 A choice of N sub-divisions per coarse bin has a variance in both event rate and
 1780 log-likelihood residuals less than the required threshold of 0.001. The event rate test is
 1781 the more stringent test. For the variance of log-likelihood residuals, the largest value is
 1782 of order 10^{-7} , corresponding to an error on the log-likelihood of about 3×10^{-4} , small
 1783 enough to be negligible for the oscillation analysis.

¹⁷⁸⁴ In practice Figure 5.11 illustrates the effect of the smearing using $N = 10$. The fast
¹⁷⁸⁵ oscillations in the sub-GeV upgoing region have been replaced with a normalisation
¹⁷⁸⁶ effect whilst the large matter resonance structure remains.

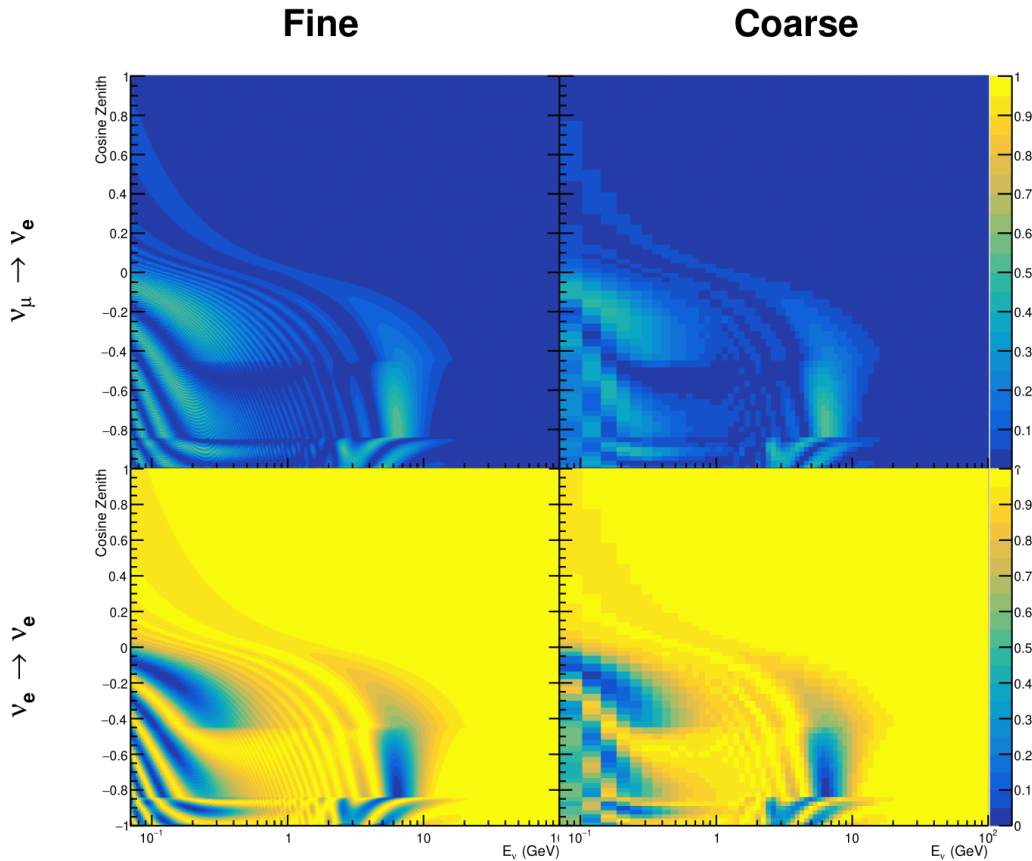


Figure 5.11: The oscillation probability, $P(\nu_\mu \rightarrow \nu_e)$ (top row) and $P(\nu_e \rightarrow \nu_e)$ (bottom row), given as a function of neutrino energy and zenith angle. The left column gives the “fine” binning used to calculate the oscillation probabilities and the right column illustrates the “coarse” binning used to reweight the MC events. The fine binning choice is given with $N = 10$, which was determined to be below threshold from Figure 5.9 and Figure 5.10.

1787 5.3 Calculation Engine

1788 As previously discussed in section 5.2, the calculation of oscillation probabilities is per-
1789 formed at run-time due to utilising continuous oscillation parameters. Consequently,
1790 the time per calculation is crucial for fit performance. The fitting framework used for
1791 this analysis was developed with ProbGPU [183]. This is a GPU-only implementation
1792 of the prob3 engine [184]. It is primarily designed for neutrino propagation in a beam
1793 experiment (single layer of constant density) with the atmospheric propagation code
1794 not being used prior to the analysis in this thesis.

1795 Another engine, CUDAProb3 [185], has been implemented within the fitting frame-
1796 work used within this analysis. It has been specifically optimised for atmospheric
1797 neutrino oscillation calculation so unfortunately does not contain the code to replace
1798 the beam oscillation calculation. Based on the benefits shown by the implementation
1799 in this chapter, efforts are being placed into including linear propagation for beam
1800 neutrino propagation into the engine [186]. The engine utilises object-orientated tech-
1801 niques as compared to the functional implementation of ProbGPU. This allows the
1802 energy and cosine zenith arrays to be kept on GPU memory, rather than having to
1803 load these arrays onto GPU memory for each calculation. General memory interfacing
1804 is one of the slowest tasks which GPUs can do, so being able to eliminate this signifi-
1805 cantly reduces the time required for calculation. This can be seen in Figure 5.12, where
1806 the GPU implementation of CUDAProb3 is approximately three times faster than the
1807 ProbGPU engine.

1808 Another significant advantage of CUDAProb3 is that it contains a CPU multithreaded
1809 implementation which is not possible with the ProbGPU or prob3 engines. This elimi-
1810 nates the requirement for GPU resources when submitting jobs to batch systems. As
1811 illustrated in Figure 5.12, the calculation speed depends on the number of available

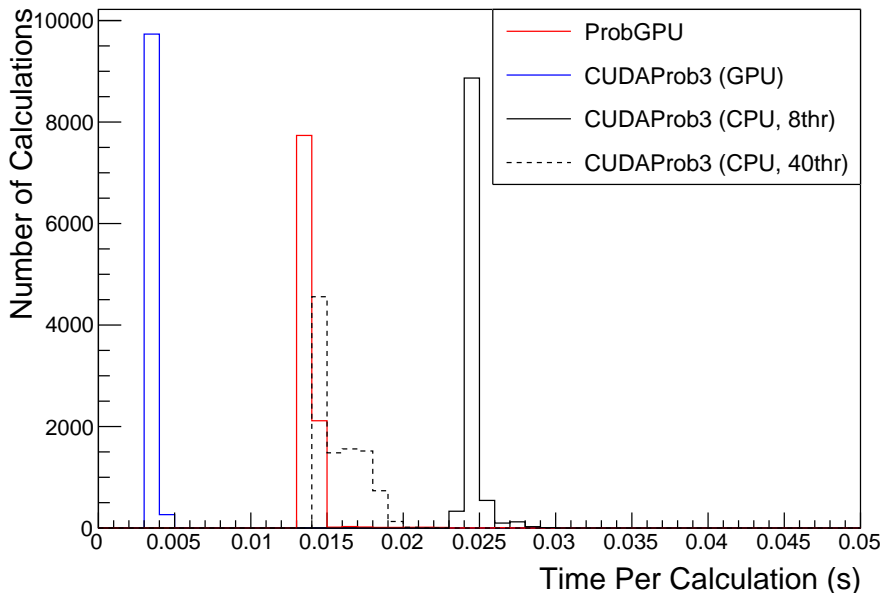


Figure 5.12: The calculation time taken to both calculate the oscillation probabilities and fill the “coarse” oscillograms, following the technique given in section 5.2, for the CUDAProb3 and ProbGPU (Red) calculation engines. CUDAProb3 has both a GPU (Blue) and CPU (Black) implementation, where the CPU implementation is multithreaded. Therefore, 8-threads (solid) and 40-threads (dashed) configurations have been used. Prob3, which is a CPU single-thread implementation has a mean step time of 1.142s.

1812 threads. Using 8 threads (which is typical of the batch systems being used) is ap-
 1813 proximately twice as slow as the ProbGPU engine implementation, but would allow
 1814 the fitting framework to be run on many more resources. This fact is utilised for any
 1815 SK-only fits but GPU resources are required for any fits which include beam samples
 1816 due to the ProbGPU requirement.

1817 5.4 Matter Density Profile

1818 For an experiment observing atmospheric neutrinos propagating through the Earth,
 1819 such as the studies presented in this thesis, a model of the Earth’s density and layering
 1820 is required. The model used within this analysis is the Preliminary Reference Earth
 1821 Model (PREM) [187]. This model provides piecewise cubic polynomials as a function

of radius which results in the density profile illustrated in Figure 5.13. As will be discussed in section 5.5, the propagator used within the calculation engine requires constant density layers. To follow the official SK-only analysis [182], the average density of each layer has been taken from the PREM model. Table 5.2 documents the density and radii of the layers used within this approximation.

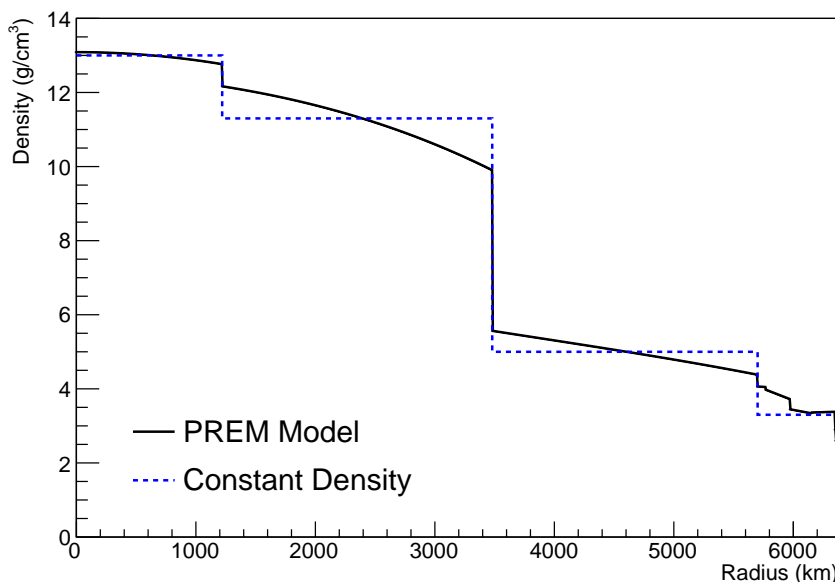


Figure 5.13: The density of the Earth given as a function of the radius, as given by the PREM model (Black) and the constant density four-layer approximation (Blue), as used in the official SK-only analysis.

Layer	Outer Radius [km]	Density [g/cm ³]	Chemical composition (Z/A)
Inner Core	1220	13	0.468 ± 0.029
Outer Core	3480	11.3	0.468 ± 0.029
Lower Mantle	5701	5.0	0.496
Transition Zone	6371	3.3	0.496

Table 5.2: Description of the four layers of the Earth invoked within the average constant density approximation of the PREM model [187].

The density measurements provided in the PREM model are provided in terms of mass density, whereas neutrino oscillations are sensitive to the electron number density. This value can be computed as the product of the chemical composition, or

the Z/A value, and the mass density of each layer. Currently, the only way to calculate this value for layers close to the Earth's core is through neutrino oscillations. The chemical composition of the upper layers of the Earth's Mantle and the Transition zone is well known due to it being predominantly pyrolite which has a chemical composition value of 0.496 [188]. The components of the Earth's core region are less well known. Consequently, the chemical composition dial for the core layers is set to a value of 0.468 [189]. This value is assigned a Gaussian error with a standard deviation equivalent to the difference in chemical composition in core and mantle layers. Figure 5.14 illustrates the effect of moving from the $Z/A = 0.5$ method which is used in the official SK-only analysis [182] to more precise values recorded by other neutrino experiments.

The beam oscillation probability in this thesis uses a baseline of 295km, density 2.6g/cm^3 [190], and chemical composition 0.5 as is done by the official T2K-only analysis.

Whilst the propagator requires a fixed density layer model of the Earth, the density only has to be fixed for a specific neutrino energy $\times \cos(\theta_Z)$ bin in a given layer (I.e. set of values at which to calculate the oscillation probability). As the density is a function of radius, which is a function of the direction in which a neutrino propagates, a better approximation of the PREM model can be made if a $\cos(\theta_Z)$ -specific density is calculated.

To achieve this, the average density, $\langle \rho \rangle_i$, in the i^{th} layer, is calculated as the density, ρ , integrated over the track a given $\cos(\theta_Z)$,

$$\langle \rho \rangle_i = \frac{1}{t_{i+1} - t_i} \int_{t_i}^{t_{i+1}} \rho(t) dt \quad (5.5)$$

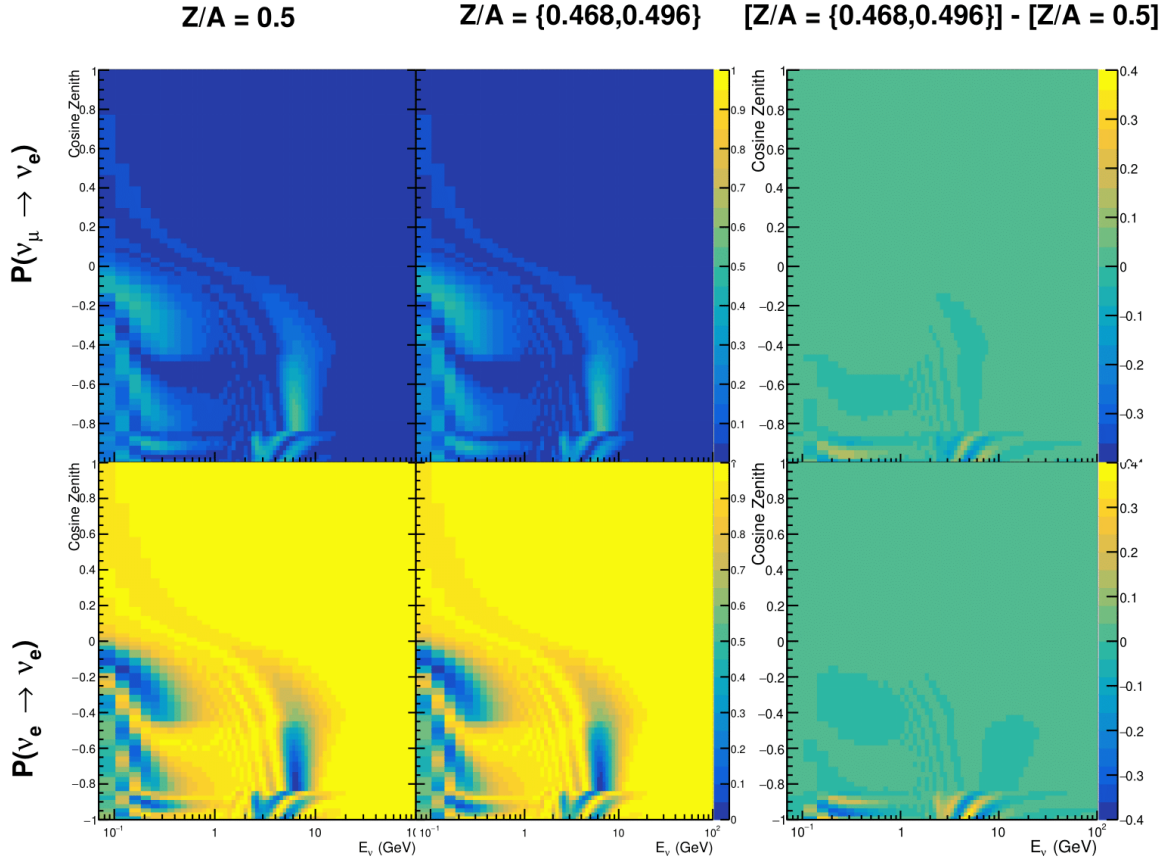


Figure 5.14: The oscillation probability, $P(\nu_\mu \rightarrow \nu_e)$ (top row) and $P(\nu_e \rightarrow \nu_\mu)$ (bottom row), given as a function of neutrino energy and zenith angle. The left column gives probabilities where the constant $Z/A = 0.5$ approximation which is used in the official SK-only analysis. The middle column gives the probabilities where the more accurate $Z/A = [0.468, 0.498]$ values as given in Table 5.2. The right column illustrates the difference in oscillation probability between the two different techniques.

where t_i are the intersection points between each layer and t is the path length of

the trajectory across the layer which is dependent upon $\cos(\theta_Z)$.

The oscillation probability calculation speed is approximately linear in the number of layers invoked within the Earth model. Therefore a four-layer model is still utilized with the only difference to the above example being that the four-layer model used for each value of $\cos(\theta_Z)$ is different. Following the method outlined in [191], a four-layer piecewise quadratic polynomial is fit to the PREM model for the four layers defined in

1859 Table 5.2. This fit was not performed by the author of the thesis and is documented
1860 in [192]. The coefficients of the quadratic fit to each layer are given in Table 5.3 with
1861 the final distribution illustrated in Figure 5.15. The quadratic approximation is clearly
1862 much closer to the PREM model as compared to the constant density approximation.

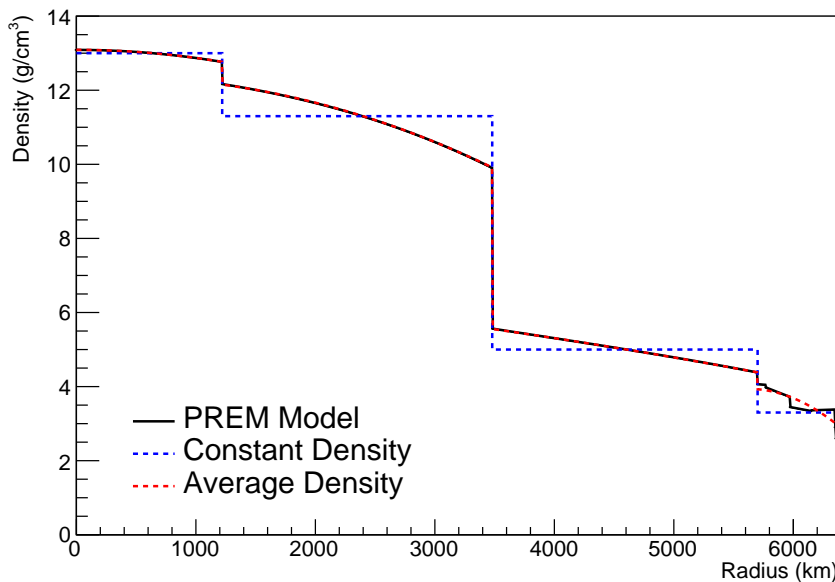


Figure 5.15: The density of the Earth given as a function of the radius, as given by the PREM model (Black), the constant density four-layer approximation (Blue), as used in the official SK-only analysis, and the quadratic approximation of the PREM model (Red).

Layer	Outer Radius [km]	Density [g/cm ³]
Inner Core	1220	$13.09 - 8.84x^2$
Outer Core	3480	$12.31 + 1.09x - 10.02x^2$
Lower Mantle	5701	$6.78 - 1.56x - 1.25x^2$
Transition Zone	6371	$-50.42 + 123.33x - 69.95x^2$

Table 5.3: The quadratic polynomial fits to the PREM model for four assumed layers of the PREM model. The fit to calculate the coefficients is given in [192], where $x = R/R_{Earth}$.

1863 The effect of using the average density per $\cos(\theta_Z)$ model is highlighted in Fig-
1864 ure 5.16. The slight discontinuity in the oscillation probability around $\cos(\theta_Z) \sim -0.45$
1865 in the fixed density model, which is due to the transition to mantle layer boundary, has

1866 been reduced. This is expected as the difference in the density across this boundary is
1867 significantly smaller in the average density model as compared to the constant density
1868 model. Whilst the difference in density across the other layer transitions is reduced,
1869 there is still a significant difference. This means the discontinuities in the oscillation
1870 probabilities remain but are significantly reduced. However, as the average density
1871 approximation matches the PREM model well in this region, these discontinuities are
1872 due to the Earth model rather than an artifact of the oscillation calculation.

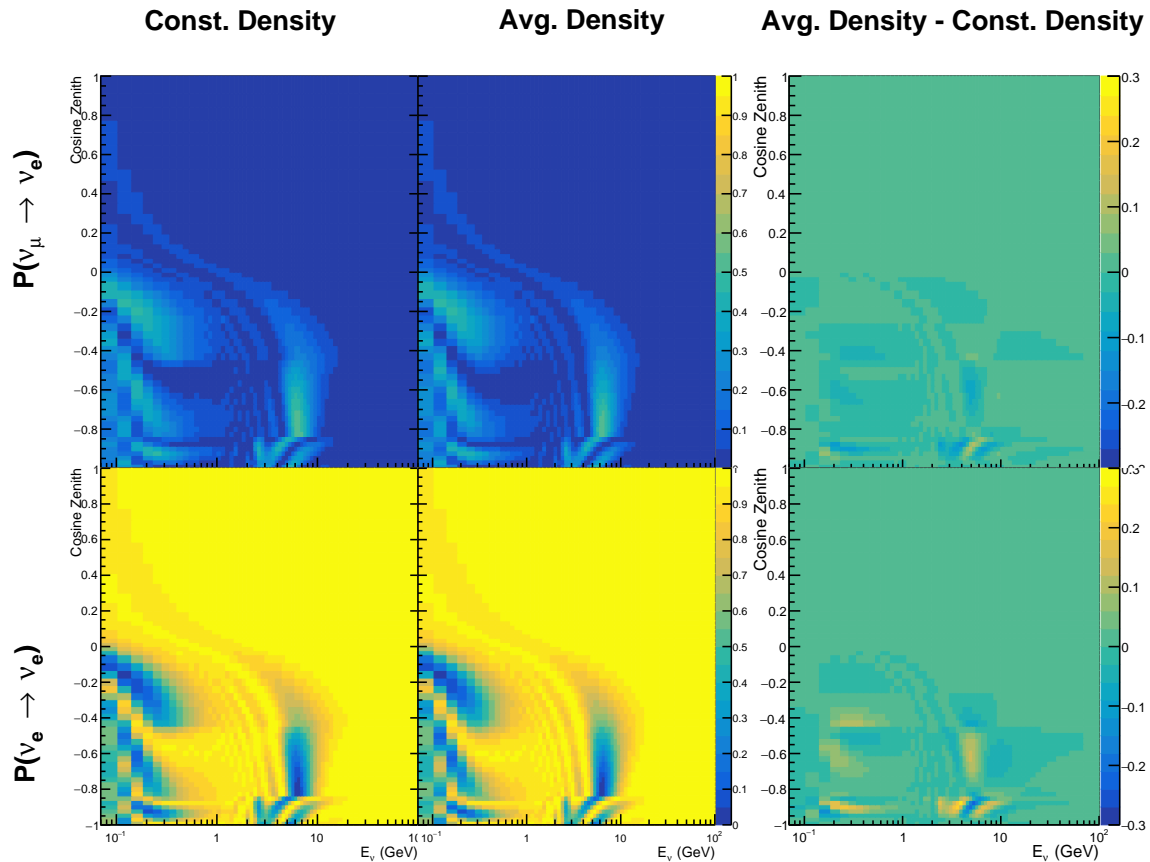


Figure 5.16: The oscillation probability, $P(\nu_\mu \rightarrow \nu_e)$ (top row) and $P(\nu_e \rightarrow \nu_\mu)$ (bottom row), given as a function of neutrino energy and zenith angle. The left column gives probabilities where the four-layer constant density approximation is used. The middle column gives the probabilities where the density is integrated over the trajectory, using the quadratic PREM approximation, for each $\cos(\theta_Z)$ is used. The right column illustrates the difference in oscillation probability between the two different techniques.

¹⁸⁷³ 5.5 Production Height Averaging

¹⁸⁷⁴ As discussed in section 5.1, the height at which the cosmic ray flux interacts in the
¹⁸⁷⁵ atmosphere is not known on an event-by-event basis. The production height can
¹⁸⁷⁶ vary from the Earth's surface to 50km above that. The SK-only analysis methodol-
¹⁸⁷⁷ ogy (described in section 5.2) for including the uncertainty on the production height
¹⁸⁷⁸ is to include variations from the Honda model when pre-calculating the oscillation
¹⁸⁷⁹ probabilities prior to the fit. This technique is not possible for this analysis which
¹⁸⁸⁰ uses continuous oscillation parameters that can not be known prior to the fit. Conse-
¹⁸⁸¹ quently, an analytical averaging technique was developed in [192]. The author of this
¹⁸⁸² thesis was not responsible for the derivation of the technique but has performed the
¹⁸⁸³ implementation and validation of the technique for this analysis alone.

¹⁸⁸⁴ The oscillation probability used within this analysis is based on [20]. The neutrino
¹⁸⁸⁵ wavefunction in the vacuum Hamiltonian evolves in each layer of constant matter
¹⁸⁸⁶ density via

$$i \frac{d\psi_j(t)}{dt} = \frac{m_j^2}{2E_\nu} \psi_j(t) - \sum_k \sqrt{2} G_F N_e U_{ej} U_{ke}^\dagger \psi_k(t), \quad (5.6)$$

¹⁸⁸⁷ where m_j^2 is the square of the j^{th} vacuum eigenstate mass, E_ν is the neutrino energy,
¹⁸⁸⁸ G_F is Fermi's constant, N_e is the electron number density and U is the PMNS matrix.
¹⁸⁸⁹ $N_e \rightarrow -N_e$ and $\delta_{CP} \rightarrow -\delta_{CP}$ for antineutrino propagation.

¹⁸⁹⁰ Using the 20 production heights per MC neutrino event, provided as 5% percentiles
¹⁸⁹¹ from the Honda flux model, a production height distribution $p_j(h|E_\nu, \cos \theta_Z)$ is built
¹⁸⁹² for each neutrino flavour $j = \nu_e, \bar{\nu}_e, \nu_\mu, \bar{\nu}_\mu$. In practice, a histogram is filled with 20
¹⁸⁹³ evenly spaced bins in production height h between 0 and 50km. The neutrino energy

1894 and cosine zenith binning is the same as that provided in section 5.2. The average
1895 production height, $\bar{h} = \int dh \frac{1}{4} \sum_j p_j(h|E_\nu, \cos(\theta_Z))$, is calculated. The production height
1896 binning of this histogram is then translated into $\delta t(h) = t(z, \bar{h}) - t(z, h)$, where $t(z, h)$
1897 is the distance travelled along the trajectory.

1898 For the i^{th} traversed layer, the transition amplitude, $D_i(t_{i+1}, t_i)$, is computed. The
1899 time ordered product of these is then used as the overall transition amplitude via

$$A(t_{n+1}, t_0) = D_n(t_{n+1}, t_n) \dots D_1(t_2, t_1) D_0(t_1, t_0), \quad (5.7)$$

1900 where,

$$\begin{aligned} D_n(t_{n+1}, t_n) &= \exp[-iH_n(t_{n+1} - t_n)] \\ &= \sum_{k=1}^3 C_k \exp[ia_k \delta t] \end{aligned} \quad (5.8)$$

1901 is expressed as a diagonalised time-dependent solution to the schrodinger equation.
1902 The 0^{th} layer is the propagation through the atmosphere and is the only term which
1903 depends on the production height. Using the subsitution $t_0 = t(\bar{h}) - \delta t(h)$, it can be
1904 shown that

$$D_0(t_1, t_0) = D_0(t_1, \bar{h}) D_0(\delta t). \quad (5.9)$$

1905 Thus Equation 5.7 becomes

$$\begin{aligned}
A(t_{n+1}, t_0) &= D_n(t_{n+1}, t_n) \dots D_1(t_2, t_1) D_0(t_1, \bar{h}) D(\delta t) \\
&= A(t_{n+1}, \bar{h}) \sum_{k=1}^3 C_k \exp[i a_k \delta t], \\
&= \sum_{k=1}^3 B_k \exp[i a_k \delta t].
\end{aligned} \tag{5.10}$$

¹⁹⁰⁶ The oscillation probability averaged over production height is calculated as

$$\begin{aligned}
\bar{P}(\nu_j \rightarrow \nu_i) &= \int d(\delta t) p_j(\delta t | E_\nu, \cos \theta_Z) P(\nu_j \rightarrow \nu_i) \\
&= \int d(\delta t) p_j(\delta t | E_\nu, \cos \theta_Z) A(t_{n+1}, t_0) A^*(t_{n+1}, t_0) \\
&= \sum_{km} (B_k)_{ij} (B_m)_{ij}^* \int d(\delta t) p_j(\delta t | E_\nu, \cos \theta_Z) \exp[i(a_k - a_m)\delta t]
\end{aligned} \tag{5.11}$$

¹⁹⁰⁷ In practice, implementation in CUDAProb3 [185] is relatively straightforward as
¹⁹⁰⁸ the majority of these terms are already calculated in the standard oscillation calculation.
¹⁹⁰⁹ Figure 5.17 illustrates the results of the production height averaging. As expected,
¹⁹¹⁰ the main effect is observed in the low-energy downward-going and horizontal-going
¹⁹¹¹ events. Upward-going events have to travel the radius of the Earth, $R_E = 6371\text{km}$,
¹⁹¹² where the production height uncertainty is a small fraction of the total path length.

¹⁹¹³

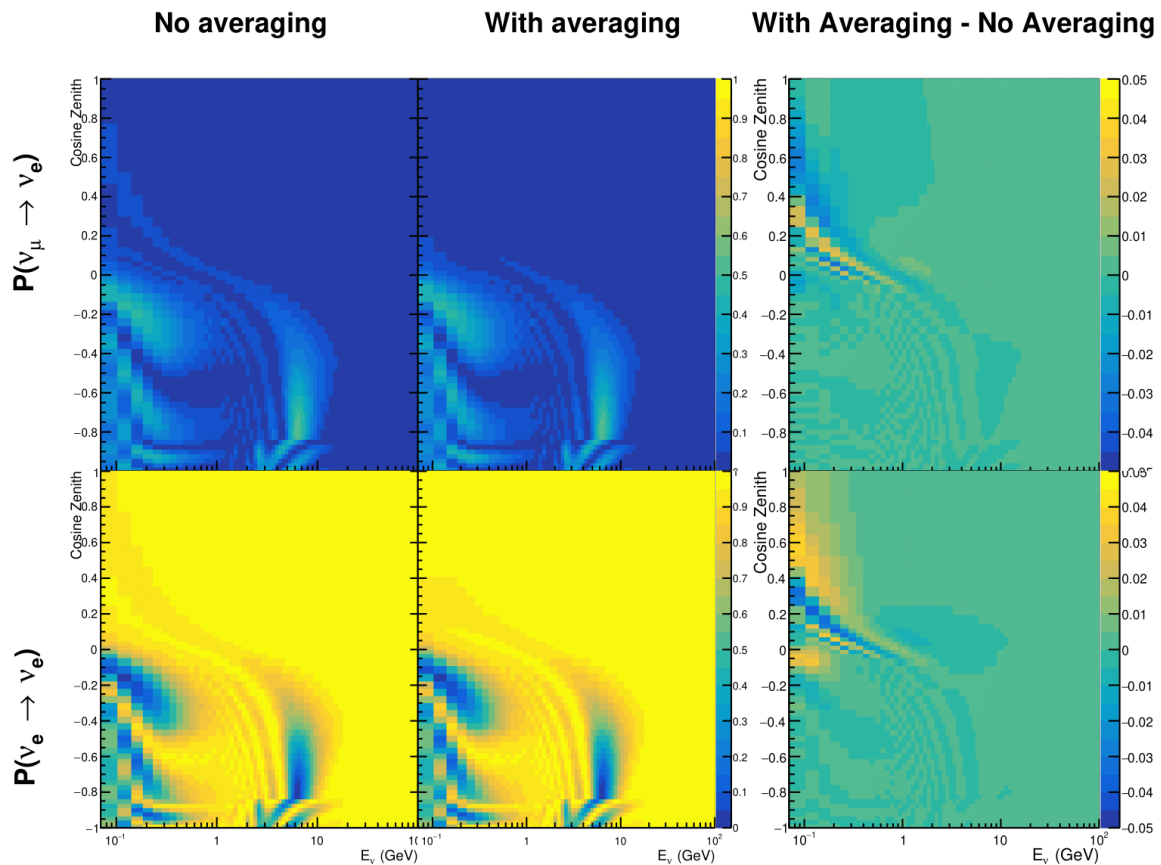


Figure 5.17: The oscillation probability, $P(\nu_\mu \rightarrow \nu_e)$ (top row) and $P(\nu_e \rightarrow \nu_e)$ (bottom row), given as a function of neutrino energy and zenith angle. The left column gives probabilities where a fixed production height of 25km is used. The middle column gives the probabilities where the production height is analytically averaged. The right column illustrates the difference in oscillation probability between the two different techniques.

₁₉₁₄ **Bibliography**

- ₁₉₁₅ [1] J. Chadwick, Verhandl. Dtsc. Phys. Ges. **16**, 383 (1914).
- ₁₉₁₆ [2] C. D. Ellis and W. A. Wooster, Proc. R. Soc. Lond. A Math. Phys. Sci. **117**, 109 (1927).
- ₁₉₁₈ [3] W. Pauli, Phys. Today **31N9**, 27 (1978).
- ₁₉₁₉ [4] E. Fermi, Z. Phys. **88**, 161 (1934).
- ₁₉₂₀ [5] F. Reines and C. L. Cowan, Phys. Rev. **92**, 830 (1953).
- ₁₉₂₁ [6] C. L. Cowan, F. Reines, F. B. Harrison, H. W. Kruse, and A. D. McGuire, Science **124**, 103 (1956), <http://science.sciencemag.org/content/124/3212/103.full.pdf>.
- ₁₉₂₃ [7] G. Danby *et al.*, Phys. Rev. Lett. **9**, 36 (1962).
- ₁₉₂₄ [8] K. Kodama *et al.*, Physics Letters B **504**, 218 (2001).
- ₁₉₂₅ [9] LSND, A. Aguilar-Arevalo *et al.*, Phys. Rev. **D64**, 112007 (2001), hep-ex/0104049.
- ₁₉₂₆ [10] MiniBooNE Collaboration, A. A. Aguilar-Arevalo *et al.*, Phys. Rev. Lett. **110**, 161801 (2013).
- ₁₉₂₈ [11] Planck Collaboration *et al.*, aap **641** (2020).
- ₁₉₂₉ [12] B. Pontecorvo, Sov. Phys. JETP **26**, 984 (1968), [Zh. Eksp. Teor. Fiz. 53, 1717 (1967)].
- ₁₉₃₀ [13] B. Pontecorvo, Sov. Phys. JETP **7**, 172 (1958), [Zh. Eksp. Teor. Fiz. 34, 247 (1957)].
- ₁₉₃₁ [14] M. Kobayashi and T. Maskawa, Progress of Theoretical Physics **49**, 652 (1973).
- ₁₉₃₂ [15] N. Cabibbo, Phys. Rev. Lett. **10**, 531 (1963).
- ₁₉₃₃ [16] A. M. and, Journal of Physics: Conference Series **587**, 012030 (2015).
- ₁₉₃₄ [17] A. Y. Smirnov, (2003).
- ₁₉₃₅ [18] S. Mikheyev and A. Smirnov, Soviet Journal of Nuclear Physics **42**, 913 (1985).
- ₁₉₃₆ [19] L. Wolfenstein, Phys. Rev. D **17**, 2369 (1978).
- ₁₉₃₇ [20] V. D. Barger, K. Whisnant, S. Pakvasa, and R. J. N. Phillips, Phys. Rev. D **22**, 2718 (1980).

- 1939 [21] The Super-Kamiokande Collaboration, Y. Ashie *et al.*, Phys. Rev. Lett. **93**, 101801
1940 (2004).
- 1941 [22] SNO Collaboration, Q. R. Ahmad *et al.*, Phys. Rev. Lett. **89**, 011301 (2002).
- 1942 [23] 2015 Nobel prize in Physics as listed by Nobelprize.org, [https://www.](https://www.nobelprize.org/nobel_prizes/physics/laureates/2015/)
1943 [nobelprize.org/nobel_prizes/physics/laureates/2015/](https://www.nobelprize.org/nobel_prizes/physics/laureates/2015/), Accessed: 22-06-
1944 2022.
- 1945 [24] J. A. Formaggio and G. P. Zeller, Rev. Mod. Phys. **84**, 1307 (2012), 1305.7513.
- 1946 [25] A. Bellerive, Int. J. Mod. Phys. A **19**, 1167 (2004).
- 1947 [26] R. Davis, D. S. Harmer, and K. C. Hoffman, Phys. Rev. Lett. **20**, 1205 (1968).
- 1948 [27] N. Vinyoles *et al.*, Astrophys. J. **835**, 202 (2017).
- 1949 [28] V. Gribov and B. Pontecorvo, Phys. Lett. B **28**, 493 (1969).
- 1950 [29] K. S. Hirata *et al.*, Phys. Rev. Lett. **63**, 16 (1989).
- 1951 [30] W. Hampel *et al.*, Phys. Lett. B **447**, 127 (1999).
- 1952 [31] SAGE Collaboration, J. N. Abdurashitov *et al.*, Phys. Rev. C **60**, 055801 (1999).
- 1953 [32] Q. R. Ahmad *et al.*, Phys. Rev. Lett. **89** (2002).
- 1954 [33] Borexino Collaboration, Nature **562**, 505 (2018).
- 1955 [34] B. Aharmim *et al.*, Astrophys. J. **653**, 1545 (2006).
- 1956 [35] M. Agostini *et al.*, (2020).
- 1957 [36] S. Andringa *et al.*, Adv. High Energy Phys. **2016**, 1 (2016).
- 1958 [37] J. F. Beacom *et al.*, Chin. phys. C **41**, 023002 (2017).
- 1959 [38] F. An *et al.*, J. Phys. G Nucl. Part. Phys. **43**, 030401 (2016).
- 1960 [39] J. Aalbers *et al.*, (2020), 2006.03114.
- 1961 [40] T. K. Gaisser and M. Honda, (2002).
- 1962 [41] G. D. Barr, T. K. Gaisser, P. Lipari, S. Robbins, and T. Stanev, Physical Review D
1963 **70** (2004).
- 1964 [42] M. Honda, T. Kajita, K. Kasahara, S. Midorikawa, and T. Sanuki, Physical Review

- 1965 D **75** (2007).
- 1966 [43] M. Honda, T. Kajita, K. Kasahara, and S. Midorikawa, Phys. Rev. D **70**, 043008 (2004).
- 1967
- 1968 [44] M. Honda, T. Kajita, K. Kasahara, and S. Midorikawa, Phys. Rev. D **83**, 123001 (2011).
- 1969
- 1970 [45] A. Fasso, A. Ferrari, P. R. Sala, and J. Ranft, (2001).
- 1971 [46] Y. Ashie *et al.*, Physical Review D **71** (2005).
- 1972 [47] F. Reines *et al.*, Phys. Rev. Lett. **15**, 429 (1965).
- 1973 [48] D. Casper *et al.*, Phys. Rev. Lett. **66**, 2561 (1991).
- 1974 [49] K. S. Hirata *et al.*, Phys. Lett. B **280**, 146 (1992).
- 1975 [50] Z. Li *et al.*, Physical Review D **98** (2018).
- 1976 [51] Kamiokande Collaboration *et al.*, (2017).
- 1977 [52] T2K Collaboration, Nature **580**, 339 (2020).
- 1978 [53] M. A. Acero *et al.*, Phys. Rev. Lett. **123**, 151803 (2019).
- 1979 [54] M. G. Aartsen *et al.*, Phys. Rev. Lett. **120** (2018).
- 1980 [55] P. Adamson *et al.*, Phys. Rev. Lett. **112** (2014).
- 1981 [56] M. S. Athar *et al.*, Progress in Particle and Nuclear Physics **124**, 103947 (2022).
- 1982 [57] G. Danby *et al.*, Phys. Rev. Lett. **9**, 36 (1962).
- 1983 [58] K. Abe *et al.*, Physical Review D **87** (2013).
- 1984 [59] MINOS Collaboration, D. G. Michael *et al.*, Phys. Rev. Lett. **97**, 191801 (2006).
- 1985 [60] G. Danby *et al.*, Phys. Rev. Lett. **9**, 36 (1962).
- 1986 [61] NOvA Collaboration, M. A. Acero *et al.*, Phys. Rev. Lett. **123**, 151803 (2019).
- 1987 [62] B. Abi, R. Acciarri, M. A. Acero, and G. e. a. Adamov, Eur. Phys. J. C Part. Fields **80** (2020).
- 1988
- 1989 [63] Hyper-Kamiokande Proto-Collaboration *et al.*, Prog. Theor. Exp. Phys. **2015**, 53C02 (2015).
- 1990

- 1991 [64] C. Blanco, D. Hooper, and P. Machado, Physical Review D **101** (2020).
- 1992 [65] MicroBooNE Collaboration *et al.*, Search for an Excess of Electron Neutrino
1993 Interactions in MicroBooNE Using Multiple Final State Topologies, 2021.
- 1994 [66] KARMEN Collaboration, B. Armbruster *et al.*, Phys. Rev. D **65**, 112001 (2002).
- 1995 [67] S.-B. Kim, T. Lasserre, and Y. Wang, Adv. High Energy Phys. **2013**, 1 (2013).
- 1996 [68] M. Sajjad Athar *et al.*, Prog. Part. Nucl. Phys. **124**, 103947 (2022), 2111.07586.
- 1997 [69] K. Abe *et al.*, Nucl. Instrum. Methods Phys. Res. A **1027**, 166248 (2022).
- 1998 [70] F. P. An *et al.*, Phys. Rev. Lett. **108**, 171803 (2012).
- 1999 [71] RENO Collaboration, J. K. Ahn *et al.*, Phys. Rev. Lett. **108**, 191802 (2012).
- 2000 [72] Double Chooz Collaboration, Y. Abe *et al.*, Phys. Rev. Lett. **108**, 131801 (2012).
- 2001 [73] J. Collaboration *et al.*, TAO Conceptual Design Report: A Precision Measurement
2002 of the Reactor Antineutrino Spectrum with Sub-percent Energy Resolution, 2020,
2003 2005.08745.
- 2004 [74] for the RENO Collaboration, New results from RENO and the 5 MeV excess,
2005 AIP Publishing LLC, 2015.
- 2006 [75] Y. Abe *et al.*, Journal of High Energy Physics **2014** (2014).
- 2007 [76] Daya Bay Collaboration, D. Adey *et al.*, Phys. Rev. Lett. **123**, 111801 (2019).
- 2008 [77] M. P. Decowski, Nucl. Phys. B. **908**, 52 (2016).
- 2009 [78] The KamLAND Collaboration, A. Gando *et al.*, Phys. Rev. D **83**, 052002 (2011).
- 2010 [79] Y. Fukuda *et al.*, Phys. Rev. Lett. **81**, 1562 (1998).
- 2011 [80] K. Abe *et al.*, Nuclear Instruments and Methods in Physics Research Section
2012 A: Accelerators, Spectrometers, Detectors and Associated Equipment **737**, 253
2013 (2014).
- 2014 [81] S. Fukuda *et al.*, Nucl. Instrum. Methods Phys. Res. A **501**, 418 (2003).
- 2015 [82] Y. Itow *et al.*, (2001).
- 2016 [83] M. Jiang *et al.*, Prog. Theor. Exp. Phys. **2019** (2019).

- 2017 [84] S. Fukuda *et al.*, Nuclear Instruments and Methods in Physics Research Section
2018 A: Accelerators, Spectrometers, Detectors and Associated Equipment **501**, 418
2019 (2003), <http://www.sciencedirect.com/science/article/pii/S016890020300425X>.
- 2020 [85] Y. Nakano *et al.*, Nucl. Instrum. Methods Phys. Res. A **977**, 164297 (2020).
- 2021 [86] Hamamatsu, Hamamatsu Photonics Photomultiplier Tubes Handbook.
- 2022 [87] K. Abe *et al.*, Nucl. Instrum. Methods Phys. Res. A **1027**, 166248 (2022).
- 2023 [88] J. F. Beacom and M. R. Vagins, Phys. Rev. Lett. **93**, 171101 (2004).
- 2024 [89] L. Marti *et al.*, Nucl. Instrum. Methods Phys. Res. A **959**, 163549 (2020).
- 2025 [90] L. Marti *et al.*, (2019).
- 2026 [91] T. Tanimori *et al.*, IEEE Transactions on Nuclear Science **36**, 497 (1989).
- 2027 [92] Super-Kamiokande Collaboration, J. Hosaka *et al.*, Phys. Rev. D **73**, 112001
2028 (2006).
- 2029 [93] H. Nishino *et al.*, Nucl. Instrum. Methods Phys. Res. A **610**, 710 (2009).
- 2030 [94] S. Yamada *et al.*, IEEE Transactions on Nuclear Science **57**, 428 (2010).
- 2031 [95] S. Yamada, Y. Hayato, Y. Obayashi, and M. Shiozawa, New online system
2032 without hardware trigger for the Super-Kamiokande experiment, in *2007 IEEE*
2033 *Nuclear Science Symposium Conference Record*, IEEE, 2007.
- 2034 [96] G. Carminati, Phys. Procedia **61**, 666 (2015).
- 2035 [97] P. A. Čerenkov, Phys. Rev. **52**, 378 (1937).
- 2036 [98] I. Frank and I. Tamm, Coherent visible radiation of fast electrons passing
2037 through matter, in *Selected Papers*, pp. 29–35, Springer Berlin Heidelberg, Berlin,
2038 Heidelberg, 1991.
- 2039 [99] The T2K Collaboration, KEK Proposal (2001),
2040 <http://neutrino.kek.jp/jhfnu/loi/loi.v2.030528.pdf>.
- 2041 [100] Y. Itow *et al.*, (2001), hep-ex/0106019.
- 2042 [101] The K2K Collaboration and S. H. Ahn, (2001), hep-ex/0103001.
- 2043 [102] The T2K Collaboration, KEK Proposal (2006), <http://j->

- 2044 parc.jp/researcher/Hadron/en/pac_0606/pdf/p11-Nishikawa.pdf.
- 2045 [103] T2K Collaboration, K. Abe *et al.*, Phys. Rev. Lett. **112**, 061802 (2014),
2046 <https://link.aps.org/doi/10.1103/PhysRevLett.112.061802>.
- 2047 [104] NINJA Collaboration, T. Fukuda *et al.*, Proposal for precise measurement of
2048 neutrino-water cross-section in NINJA physics run, Proposal for J-PARC and
2049 KEK, 2017.
- 2050 [105] T. Ovsianikova *et al.*, Physics of Particles and Nuclei **48**, 1014 (2017),
2051 <https://doi.org/10.1134/S1063779617060478>.
- 2052 [106] M. Antonova *et al.*, Journal of Instrumentation **12**, C07028 (2017),
2053 <http://stacks.iop.org/1748-0221/12/i=07/a=C07028>.
- 2054 [107] The T2K Collaboration, K. Abe *et al.*, Phys. Rev. D **102**, 012007 (2020).
- 2055 [108] K. Abe *et al.*, Progress of Theoretical and Experimental Physics **2021** (2021).
- 2056 [109] The T2K Collaboration, K. Abe *et al.*, Nuclear Instruments
2057 and Methods in Physics Research Section A: Accelerators, Spectrometers,
2058 Detectors and Associated Equipment **659**, 106 (2011),
2059 <http://www.sciencedirect.com/science/article/pii/S0168900211011910>.
- 2060 [110] K. Matsuoka *et al.*, Nuclear Instruments and Methods in Physics Research Section
2061 A: Accelerators, Spectrometers, Detectors and Associated Equipment **624**, 591
2062 (2010), <http://www.sciencedirect.com/science/article/pii/S016890021002098X>.
- 2063 [111] K. Abe *et al.*, Phys. Rev. D. **103** (2021).
- 2064 [112] T. Vladislavljevic, *Predicting the T2K neutrino flux and measuring oscillation parameters* Springer theses, 1 ed. (Springer Nature, Cham, Switzerland, 2020).
- 2066 [113] D. Beavis, A. Carroll, and I. Chiang, (1995).
- 2067 [114] P.-A. Amaudruz *et al.*, Nuclear Instruments and Methods in Physics Research
2068 Section A: Accelerators, Spectrometers, Detectors and Associated Equipment
2069 **696**, 1 (2012).
- 2070 [115] N. Abgrall *et al.*, Nuclear Instruments and Methods in Physics Research Section
2071 A: Accelerators, Spectrometers, Detectors and Associated Equipment **637**, 25
2072 (2011).

- 2073 [116] S. Assylbekov *et al.*, Nuclear Instruments and Methods in Physics Research
2074 Section A: Accelerators, Spectrometers, Detectors and Associated Equipment
2075 **686**, 48 (2012).
- 2076 [117] D. Allan *et al.*, Journal of Instrumentation **8**, P10019 (2013).
- 2077 [118] F. Vannucci, Advances in High Energy Physics **2014**, 1 (2014).
- 2078 [119] UA1 magnet sets off for a second new life, 2022.
- 2079 [120] S. Aoki *et al.*, Nuclear Instruments and Methods in Physics Research Section
2080 A: Accelerators, Spectrometers, Detectors and Associated Equipment **698**, 135
2081 (2013).
- 2082 [121] M. Yokoyama *et al.*, Nuclear Instruments and Methods in Physics Research
2083 Section A: Accelerators, Spectrometers, Detectors and Associated Equipment
2084 **622**, 567 (2010).
- 2085 [122] K. Suzuki *et al.*, Progress of Theoretical and Experimental Physics **2015**, 53C01
2086 (2015).
- 2087 [123] S. Brooks, A. Gelman, G. L. Jones, and X.-L. Meng, *Handbook of Markov Chain
Monte Carlo* (CRC Press, 2011).
- 2088 [124] W. R. Gilks, S. Richardson, and D. J. Spiegelhalter, *Markov Chain Monte Carlo in
Practice* (Chapman & Hall/CRC Interdisciplinary Statistics, 1995).
- 2089 [125] C. Wret, *Minimising systematic uncertainties in the T2K experiment using near-
detector and external data*, PhD thesis, Imperial College London, 2018.
- 2090 [126] K. E. Duffy, *Measurement of the Neutrino Oscillation Parameters $\sin^2 \theta_{23}$, Δm_{32}^2 ,
 $\sin^2 \theta_{13}$, and δ_{CP} in Neutrino and Antineutrino Oscillation at T2K*, PhD thesis, Oriel
2091 College, University of Oxford, 2016.
- 2092 [127] T. Bayes, Rev., Phil. Trans. Roy. Soc. Lond. **53**, 370 (1764).
- 2093 [128] N. Metropolis, A. W. Rosenbluth, M. N. Rosenbluth, A. H. Teller, and E. Teller,
2094 Journal of Chemical Physics **21** (1970).
- 2095 [129] W. K. Hastings, Biometrika **57** (1970).
- 2096 [130] J. Dunkley, M. Bucher, P. G. Ferreira, K. Moodley, and C. Skordis, Mon. Not. R.
2097 Astron. Soc. **356**, 925 (2005).

- ²¹⁰² [131] Particle Data Group *et al.*, Prog. Theor. Exp. Phys. **2020** (2020).
- ²¹⁰³ [132] H. Jeffreys, *The Theory of Probability* Oxford Classic Texts in the Physical Sciences
²¹⁰⁴ (, 1939).
- ²¹⁰⁵ [133] R. E. Kass and A. E. Raftery, J. Am. Stat. Assoc. **90**, 773 (1995).
- ²¹⁰⁶ [134] T. Böhlen *et al.*, Nuclear Data Sheets **120**, 211 (2014),
²¹⁰⁷ <http://www.sciencedirect.com/science/article/pii/S0090375214005018>.
- ²¹⁰⁸ [135] R. Brun *et al.*, *GEANT: Detector Description and Simulation Tool; Oct 1994*CERN
²¹⁰⁹ Program Library (CERN, Geneva, 1993), <http://cds.cern.ch/record/1082634>,
²¹¹⁰ Long Writeup W5013.
- ²¹¹¹ [136] T2K Collaboration, K. Abe *et al.*, Phys. Rev. D **87**, 012001 (2013).
- ²¹¹² [137] C. Zeitnitz and T. Gabriel, Nuclear Instruments and Methods in Physics Research Section A: Accelerators, Spectrometers, Detectors and Associated Equipment **349**, 106 (1994),
²¹¹³ <http://www.sciencedirect.com/science/article/pii/0168900294906130>.
- ²¹¹⁶ [138] N. Abgrall *et al.*, Physical Review C **84** (2011).
- ²¹¹⁷ [139] N. Abgrall *et al.*, Physical Review C **85** (2012).
- ²¹¹⁸ [140] N. Abgrall *et al.*, Nuclear Instruments and Methods in Physics Research Section
²¹¹⁹ A: Accelerators, Spectrometers, Detectors and Associated Equipment **701**, 99
²¹²⁰ (2013), <http://www.sciencedirect.com/science/article/pii/S016890021201234X>.
- ²¹²¹ [141] HARP Collaboration, M. Apollonio *et al.*, Phys. Rev. C **80**, 035208 (2009),
²¹²² <https://link.aps.org/doi/10.1103/PhysRevC.80.035208>.
- ²¹²³ [142] A. Fiorentini *et al.*, T2K Technical Note **217** (2017).
- ²¹²⁴ [143] B. Blau *et al.*, Nuclear Physics B - Proceedings Supplements **113**, 125 (2002).
- ²¹²⁵ [144] S. Haino *et al.*, Physics Letters B **594**, 35 (2004).
- ²¹²⁶ [145] NASA, U.S. Standard Atmosphere, 1976, 1976.
- ²¹²⁷ [146] S. Roesler, R. Engel, and J. Ranft, The Monte Carlo Event Generator DPMJET-III,
²¹²⁸ in *Advanced Monte Carlo for Radiation Physics, Particle Transport Simulation and*
²¹²⁹ *Applications*, pp. 1033–1038, Springer Berlin Heidelberg, 2001.

- 2130 [147] K. Niita *et al.*, Radiation Measurements **41**, 1080 (2006).
- 2131 [148] T. Sanuki *et al.*, Physics Letters B **541**, 234 (2002).
- 2132 [149] P. Achard *et al.*, Physics Letters B **598**, 15 (2004).
- 2133 [150] Y. Hayato and L. Pickering, The European Physical Journal Special Topics **230**, 4469 (2021).
- 2134
- 2135 [151] Y. Hayato, Acta Physica Polonica B **40** (2009).
- 2136 [152] C. L. Smith, Physics Reports **3**, 261 (1972),
2137 <http://www.sciencedirect.com/science/article/pii/0370157372900105>.
- 2138 [153] O. Benhar, A. Fabrocini, and S. Fantoni, Nuclear Physics A **497**, 423 (1989).
- 2139 [154] R. Bradford, A. Bodek, H. Budd, and J. Arrington, Nuclear Physics B - Proceedings Supplements **159**, 127 (2006),
2140 <http://www.sciencedirect.com/science/article/pii/S0920563206005184>,
2141 Proceedings of the 4th International Workshop on Neutrino-Nucleus Interac-
2142 tions in the Few-GeV Region.
- 2143
- 2144 [155] A. A. Aguilar-Arevalo *et al.*, Physical Review D **81** (2010).
- 2145 [156] R. Gran, J. Nieves, F. Sanchez, and M. J. V. Vacas, Phys. Rev. D **88**, 113007 (2013),
2146 <https://link.aps.org/doi/10.1103/PhysRevD.88.113007>.
- 2147 [157] C. Berger and L. M. Sehgal, Phys. Rev. D **76**, 113004 (2007).
- 2148 [158] C. Berger and L. M. Sehgal, Phys. Rev. D **79**, 053003 (2009),
2149 <https://link.aps.org/doi/10.1103/PhysRevD.79.053003>.
- 2150 [159] T. Sjöstrand, Computer Physics Communications **82**, 74 (1994).
- 2151 [160] C. Bronner and M. Hartz, Tuning of the Charged Hadrons Multiplicities for Deep
2152 Inelastic Interactions in NEUT, in *Proceedings of the 10th International Workshop on*
2153 *Neutrino-Nucleus Interactions in Few-GeV Region (NuInt15)*, Journal of the Physical
2154 Society of Japan, 2016.
- 2155 [161] M. Glück, E. Reya, and A. Vogt, The European Physical Journal C **5**, 461 (1998).
- 2156 [162] A. Bodek and U.-k. Yang, Axial and Vector Structure Functions for Electron- and
2157 Neutrino- Nucleon Scattering Cross Sections at all Q^2 using Effective Leading
2158 order Parton Distribution Functions, 2010.

- ²¹⁵⁹ [163] A. Bodek and U.-K. Yang, (2010).
- ²¹⁶⁰ [164] S. Gollapinni, (2016).
- ²¹⁶¹ [165] E. S. P. Guerra *et al.*, Phys. Rev. D **99**, 052007 (2019).
- ²¹⁶² [166] GEANT4, S. Agostinelli *et al.*, Nucl. Instrum. Meth. **A506**, 250 (2003).
- ²¹⁶³ [167] R. Brun, F. Bruyant, M. Maire, A. C. McPherson, and P. Zanarini, (1987).
- ²¹⁶⁴ [168] K. Abe *et al.*, Physical Review Letters **121** (2018).
- ²¹⁶⁵ [169] K. Abe *et al.*, Physical Review D **91** (2015).
- ²¹⁶⁶ [170] R. Patterson *et al.*, Nuclear Instruments and Methods in Physics Research Section A: Accelerators, Spectrometers, Detectors and Associated Equipment **608**, 206 (2009).
- ²¹⁶⁹ [171] e. a. S. Berkman, T2K Technical Note **146** (2013).
- ²¹⁷⁰ [172] e. a. A. Himmel, T2K Technical Note **219** (2015).
- ²¹⁷¹ [173] F. a. James, (1998), CERN Program Library Long Writeups.
- ²¹⁷² [174] e. a. D. Barrow, T2K Technical Note **326** (2020).
- ²¹⁷³ [175] A. Maghrabi, A. Aldosari, and M. Almutairi, Advances in Space Research **68**, 2941 (2021).
- ²¹⁷⁵ [176] Super-Kamiokande Collaboration, K. Abe *et al.*, Phys. Rev. D **97**, 072001 (2018),
²¹⁷⁶ <https://link.aps.org/doi/10.1103/PhysRevD.97.072001>.
- ²¹⁷⁷ [177] Particle Data Group, J. Beringer *et al.*, Phys. Rev. D **86**, 010001 (2012).
- ²¹⁷⁸ [178] Y. N. and, Journal of Physics: Conference Series **888**, 012191 (2017).
- ²¹⁷⁹ [179] M. Jiang, *Study of the neutrino mass hierarchy with the atmospheric neutrino data collected in Super-Kamiokande IV*, PhD thesis, Kyoto University, 2019.
- ²¹⁸¹ [180] P. Machado, H. Schulz, and J. Turner, Physical Review D **102** (2020).
- ²¹⁸² [181] T2K Collaboration, K. Abe *et al.*, Phys. Rev. Lett. **112**, 181801 (2014).
- ²¹⁸³ [182] R. Wendell, *Three Flavor Oscillation Analysis of Atmospheric Neutrinos in Super-Kamiokande*, PhD thesis, University of North Carolina, 2008.

- ²¹⁸⁵ [183] R. G. Calland, A. C. Kaboth, and D. Payne, **9**, P04016 (2014).
- ²¹⁸⁶ [184] R. Wendell, <http://www.phy.duke.edu/raw22/public/Prob3++/>.
- ²¹⁸⁷ [185] F. Kallenborn, C. Hundt, S. Böser, and B. Schmidt, Computer Physics Communications **234**, 235 (2019).
- ²¹⁸⁸
- ²¹⁸⁹ [186] L. Warsame, MaCh3 Analysis Progress.
- ²¹⁹⁰ [187] A. M. Dziewonski and D. L. Anderson, Phys. Earth Planet. Inter. **25**, 297 (1981).
- ²¹⁹¹ [188] S. Bourret, J. A. B. Coelho, and V. V. E. and, Journal of Physics: Conference Series **888**, 012114 (2017).
- ²¹⁹²
- ²¹⁹³ [189] C. Rott, A. Taketa, and D. Bose, Scientific Reports **5** (2015).
- ²¹⁹⁴ [190] K. Hagiwara, N. Okamura, and K. ichi Senda, Journal of High Energy Physics **2011** (2011).
- ²¹⁹⁵
- ²¹⁹⁶ [191] D. Typinski, Earth Gravity, <http://www.typnet.net/Essays/EarthGravGraphics/EarthGrav.pdf>, Accessed: 24-06-2022.
- ²¹⁹⁷
- ²¹⁹⁸ [192] e. a. D. Barrow, T2K Technical Note **425** (2022).

²¹⁹⁹ List of Figures

²²⁰⁰	1.1	The cross-section of neutrinos from various natural and man-made sources as a function of neutrino energy. Taken from [24]	10
²²⁰¹			
²²⁰²	1.2	The solar neutrino flux as a function of neutrino energy for various fusion reactions and decay chains as predicted by the Standard Solar Model. Taken from [25].	11
²²⁰³			
²²⁰⁴			
²²⁰⁵	1.3	Left panel: The atmospheric neutrino flux for different neutrino flavours as a function of neutrino energy as predicted by the 2007 Honda model (“This work”) [42], the 2004 Honda model (“HKKM04”) [43], the Bartol model [41] and the FLUKA model [45]. Right panel: The ratio of the muon to electron neutrino flux as predicted by all the quoted models. Both figures taken from [42].	13
²²⁰⁶			
²²⁰⁷			
²²⁰⁸			
²²⁰⁹			
²²¹⁰			
²²¹¹	1.4	A diagram illustrating the definition of zenith angle as used in the Super Kamiokande experiment [46].	13
²²¹²			
²²¹³	1.5	Prediction of $\nu_e, \bar{\nu}_e, \nu_\mu, \bar{\nu}_\mu$ fluxes as a function of zenith angle as calculated by the HKKM model [44]. The left, middle and right panels represent three values of neutrino energy, 0.32GeV, 1.0GeV and 3.2GeV respectively. Predictions for other models including Bartol [41], Honda [42] and FLUKA [45] are given in [46].	14
²²¹⁴			
²²¹⁵			
²²¹⁶			
²²¹⁷			
²²¹⁸	1.6	Constraints on the atmospheric oscillation parameters, $\sin^2(\theta_{23})$ and Δm_{23}^2 , from atmospheric and long baseline experiments: SK [51], T2K [52], NO ν A [53], IceCube [54] and MINOS [55]. Figure taken from [56].	15
²²¹⁹			
²²²⁰			
²²²¹	1.7	Reactor electron antineutrino fluxes for ^{235}U (Black), ^{238}U (Green), ^{239}Pu (Purple), and ^{241}Pu (Orange) isotopes. The inverse β -decay cross-section (Blue) and corresponding measurable neutrino spectrum (Red) are also given. Top panel: Schematic of Inverse β -decay interaction including the eventual capture of the emitted neutron. This capture emits a γ -ray which provides a second signal of the event. Taken from [68].	18
²²²²			
²²²³			
²²²⁴			
²²²⁵			
²²²⁶			
²²²⁷	2.1	A schematic diagram of the Super-Kamiokande Detector. Taken from [82].	22

2228	2.2	The location of “standard PMTs” (red) inside the SK detector. Taken from [80].	26
2229	2.3	Schematic view of the data flow through the data acquisition and online system. Taken from [94].	29
2232	2.4	The cross-section view of the Tokai to Kamioka experiment illustrating the beam generation facility at J-PARC, the near detector situated at a baseline of 280m and the Super Kamiokande far detector situated 295km from the beam target.	33
2233	2.5	The near detector suite for the T2K experiment showing the ND280 and INGRID detectors. The distance between the detectors and the beam target is 280m.	34
2236	2.6	Top panel: Bird’s eye view of the most relevant part of primary and sec- ondary beamline used within the T2K experiment. The primary beam- line is the main-ring proton synchrotron, kicker magnet, and graphite target. The secondary beamline consists of the three focusing horns, decay volume, and beam dump. Figure taken from [109]. Bottom panel: The side-view of the secondary beamline including the focusing horns, beam dump and neutrino detectors. Figure taken from [110].	35
2240	2.7	The Monte Carlo prediction of the energy spectrum for each flavour of neutrino (ν_e , $\bar{\nu}_e$, ν_μ and $\bar{\nu}_\mu$) in the neutrino dominated beam FHC mode (Left) and antineutrino dominated beam RHC mode (Right) expected at SK. Taken from [111].	37
2244	2.8	Top panel: T2K muon neutrino disappearance probability as a function of neutrino energy. Middle panel: T2K electron neutrino appearance probability as a function of neutrino energy. Bottom panel: The neutrino flux distribution for three different off-axis angles (Arbitrary units) as a function of neutrino energy.	38
2245	2.9	The components of the ND280 detector. The neutrino beam travels from left to right. Taken from [109].	39
2257	2.10	Comparison of data to Monte Carlo prediction of integrated deposited energy as a function of track length for particles that stopped in FGD1. Taken from [114].	41

2260	2.11 Schematic design of a Time Projection Chamber detector. Taken from [115].	42
2261	2.12 The distribution of energy loss as a function of reconstructed momentum for charged particles passing through the TPC, comparing data to Monte Carlo prediction. Taken from [115].	43
2264	2.13 A schematic of the P0D side-view. Taken from [116].	44
2265	2.14 Left panel: The Interactive Neutrino GRID on-axis Detector. 14 modules are arranged in a cross-shape configuration, with the center modules being directly aligned with the on-axis beam. Right panel: The layout of a single module of the INGRID detector. Both figures are recreated from [109].	47
2270	3.1 Example of using Monte Carlo techniques to find the area under the blue line. The gradient and intercept of the line are 0.4 and 1.0 respectively. The area found to be under the curve using one thousand samples is 29.9 units.	52
2274	3.2 The area under a line of gradient 0.4 and intercept 1.0 for the range $0 \leq x \leq 10$ as calculated using Monte Carlo techniques as a function of the number of samples used in each repetition. The analytical solution to the area is 30 units as given by the red line.	53
2278	3.3 Three MCMC chains, each with a stationary distribution equal to a Gaussian centered at 0 and width 1 (As indicated by the black dotted lines). All of the chains use a Gaussian proposal function but have different widths (or 'step size σ '). The top panel has $\sigma = 0.1$, middle panel has $\sigma = 0.5$ and the bottom panel has $\sigma = 5.0$.	58
2283	3.4 The log-likelihood from the fit detailed in DB: Link to AsimovA Sensitivity Section as a function of the number of steps accumulated in each fit. Many independent MCMC chains were run in parallel and overlaid on this plot. The red line indicates the 1×10^5 step burn-in period after which the log-likelihood becomes stable.	59

2288	3.5	Left: The two dimensional probability distribution for two correlated parameters x and y . The red distribution shows the two dimensional probability distribution when $0 \leq x \leq 5$. Right: The marginalised probability distribution for the y parameter found when requiring the x to be bound between $-5 \leq x \leq 5$ and $0 \leq x \leq 5$ for the black and red distribution, respectively.	62
2294	4.1	The NEUT prediction of the ν_μ -H ₂ O cross-section overlaid on the T2K ν_μ flux. The charged current (black, solid) and neutral current (black, dashed) inclusive, charged current quasi-elastic (blue, solid), charged current 2p2h (blue, dashed), charged current single pion production (pink), and charged current multi- π and DIS (Purple) cross-sections are illustrated. Taken from [150].	68
2300	4.2	Illustration of the various processes which a pion can undergo before exiting the nucleus. Taken from [164].	70
2302	4.3	Event displays from Super Kamiokande illustrating the “crisp” ring from a muon and the typically “fuzzier” electron ring. Each pixel represents a PMT and the color scheme denotes the accumulated charge deposited on that PMT. Figures taken from [172].	72
2306	4.4	The electron/muon PID separation parameter for all sub-GeV single-ring events in SK-IV. The charged current (CC) component is broken down in four flavours of neutrino ($\nu_\mu, \bar{\nu}_\mu, \nu_e$ and $\bar{\nu}_e$). Events with positive values of the parameter are determined to be electron-like.	76
2310	4.5	The variation of the measured dark rate as a function of date, broken down by PMT type. The SK-IV and SK-V periods span September 2008 to May 2018 and January 2019 to July 2020 respectively. The break in measurement between 2018 corresponds to the period of tank repair and refurbishment. Figure adapted from [174].	78
2315	4.6	Comparison of the measured raw charge deposited per event from the stopping muon data samples between SK-IV (Blue) and SK-V (Red), split by the primary muon subevent and the associated decay electron subevent.	79

2319	4.7	The distribution of the reconstructed momentum from the muon ring divided by the distance between the reconstructed muon and decay elec- tron vertices as found in the stopping muon data sets of SK-IV (Black) and SK-IV (Red). Only events with one tagged decay electron and con- sidered. A Gaussian fit is considered in the range [2.0, 2.4] MeV/cm and illustrated as the solid curve.	80
2320			
2321			
2322			
2323			
2324			
2325	4.8	The χ^2 difference between the SK-IV and SK-V reconstructed muon momentum divided by range when the SK-V is modified by the scaling parameter α . Both additive (Blue) and multiplicative (Black) scaling factors have been considered. In practice, the additive scaling factor actually uses the value of $(\alpha - 1.0)$	81
2326			
2327			
2328			
2329			
2330	4.9	A depiction of the topology patterns for fully-contained (FC), partially- contained (PC) and up-going muon (Up- μ) samples included in this analysis.	82
2331			
2332			
2333	4.10	The predicted neutrino flux of the fully contained (FC) sub-GeV and multi-GeV, partially contained (PC) and upward-going muon (Up- μ) events. The prediction is broken down by the $\nu_x \rightarrow \nu_e$ prediction (top left), $\nu_x \rightarrow \nu_\mu$ prediction (top right) and $\nu_x \rightarrow \nu_\tau$ prediction (bottom). All systematic dials are set to their nominal values and the Asimov A oscillation parameters are assumed.	84
2334			
2335			
2336			
2337			
2338			
2339	5.1	An “Oscillogram” that depicts the $P(\nu_\mu \rightarrow \nu_e)$ oscillation probability as a function of neutrino energy and cosine of the zenith angle. The zenith angle is defined such that $\cos(\theta_Z) = 1.0$ represents neutrinos that travel from directly above the detector. The four-layer constant density PREM model approximation is used and Asimov A oscillation parameters are assumed.	88
2340			
2341			
2342			
2343			
2344			
2345	5.2	The effect of δ_{CP} for atmospheric neutrinos given in terms of the neu- trino energy and zenith angle. The oscillogram compares the $P(\nu_\mu \rightarrow \nu_e)$ oscillation probability for a CP conserving ($\delta_{CP} = 0.0$) and CP violating ($\delta_{CP} = -1.601$) value of δ_{CP} . The other oscillation parameters assume the “Asimov A” oscillation parameter set given in Table 5.1.	90
2346			
2347			
2348			
2349			

2350 5.3	An illustration of the matter-induced effects on the oscillation probability, given as a function of neutrino energy and zenith angle. The top row of panels gives the $P(\nu_e \rightarrow \nu_e)$ oscillation probability and the bottom row illustrates the $P(\bar{\nu}_e \rightarrow \bar{\nu}_e)$ oscillation probability. The left column highlights the oscillation probability in a vacuum, whereas the middle and right column represents the oscillation probabilities when the four layer fixed density PREM model is assumed. All oscillation probabilities assume the “Asimov A” set given in Table 5.1, but importantly, the right column sets an inverted mass hierarchy. The “matter resonance” effects at $E_\nu \sim 5\text{GeV}$ can be seen in the $P(\nu_e \rightarrow \nu_e)$ for normal mass hierarchy and $P(\bar{\nu}_e \rightarrow \bar{\nu}_e)$ for inverted hierarchy.	91
2361 5.4	The oscillation probability for beam neutrino events given as a function of neutrino energy. All oscillation parameters assume the “Asimov A” set given in Table 5.1 unless otherwise stated. Each panel represents a change in one of the oscillation parameters whilst keeping the remaining parameters fixed.	92
2366 5.5	The number of electron-like events in the FHC and RHC operating mode of the beam, as a function of the oscillation probabilities. Both normal hierarchy (Solid) and inverse hierarchy (Dashed) values of Δm_{23}^2 are given.	93
2370 5.6	The oscillation probability $P(\nu_\mu \rightarrow \nu_e)$, given as a function of neutrino energy and zenith angle, which highlights an example of the “fast” oscillations in the sub-GeV upgoing region.	95
2373 5.7	Illustration of the averaging procedure for $N = 2$. The oscillation probabilities calculated on the finer left binning are averaged to obtain the oscillation probabilities in the coarser right binning. These averaged oscillation probabilities with the coarser binning are then applied to each event during the fit.	97
2378 5.8	Event rate of the SubGeV_elike_0dcy sample as a function of the number of sub-divisions per coarse bin. Each subplot represents the event rate of the sample at a different oscillation parameter set (thrown from the PDG priors). The red line in each subplot represents the mean of the event rate over the different values of sub-divisions for that particular oscillation parameter throw.	99

2384	5.9	Variance of event rate for each atmospheric sample as a function of the number of sub-divisions per coarse bin. The solid red line indicates the 0.1% threshold and the dashed red line is a graphical indication of the variance at a sub-division $N = 10$	100
2388	5.10	Variance of sample likelihood, when compared to ‘Asimov data’ set at Asimov A, for each atmospheric sample as a function of the number of sub-divisions per coarse bin. The solid red line indicates the 0.1% threshold and the dashed red line is a graphical indication of the variance at a sub-division $N = 10$	101
2393	5.11	The oscillation probability, $P(\nu_\mu \rightarrow \nu_e)$ (top row) and $P(\nu_e \rightarrow \nu_e)$ (bottom row), given as a function of neutrino energy and zenith angle. The left column gives the “fine” binning used to calculate the oscillation probabilities and the right column illustrates the “coarse” binning used to reweight the MC events. The fine binning choice is given with $N = 10$, which was determined to be below threshold from Figure 5.9 and Figure 5.10.	102
2400	5.12	The calculation time taken to both calculate the oscillation probabilities and fill the “coarse” oscillograms, following the technique given in section 5.2, for the CUDAProb3 and ProbGPU (Red) calculation engines. CUDAProb3 has both a GPU (Blue) and CPU (Black) implementation, where the CPU implementation is multithreaded. Therefore, 8-threads (solid) and 40-threads (dashed) configurations have been used. Prob3, which is a CPU single-thread implementation has a mean step time of 1.142s.	104
2408	5.13	The density of the Earth given as a function of the radius, as given by the PREM model (Black) and the constant density four-layer approximation (Blue), as used in the official SK-only analysis.	105

2411	5.14 The oscillation probability, $P(\nu_\mu \rightarrow \nu_e)$ (top row) and $P(\nu_e \rightarrow \nu_e)$ (bottom row), given as a function of neutrino energy and zenith angle. The left column gives probabilities where the constant $Z/A = 0.5$ approximation which is used in the official SK-only analysis. The middle column gives the probabilities where the more accurate $Z/A = [0.468, 0.498]$ values as given in Table 5.2. The right column illustrates the difference in oscillation probability between the two different techniques.	107
2419	5.15 The density of the Earth given as a function of the radius, as given by the PREM model (Black), the constant density four-layer approximation (Blue), as used in the official SK-only analysis, and the quadratic approximation of the PREM model (Red).	108
2423	5.16 The oscillation probability, $P(\nu_\mu \rightarrow \nu_e)$ (top row) and $P(\nu_e \rightarrow \nu_e)$ (bottom row), given as a function of neutrino energy and zenith angle. The left column gives probabilities where the four-layer constant density approximation is used. The middle column gives the probabilities where the density is integrated over the trajectory, using the quadratic PREM approximation, for each $\cos(\theta_Z)$ is used. The right column illustrates the difference in oscillation probability between the two different techniques.	110
2430	5.17 The oscillation probability, $P(\nu_\mu \rightarrow \nu_e)$ (top row) and $P(\nu_e \rightarrow \nu_e)$ (bottom row), given as a function of neutrino energy and zenith angle. The left column gives probabilities where a fixed production height of 25km is used. The middle column gives the probabilities where the production height is analytically averaged. The right column illustrates the difference in oscillation probability between the two different techniques.	114

List of Tables

2437	2.1	The various SK periods and respective live-time. The SK-VI live-time is calculated until 1 st April 2022. SK-VII started during the writing of this thesis.	21
2440	2.2	The trigger thresholds and extended time windows saved around an event which were utilised throughout the SK-IV period. The exact thresholds can change and the values listed here represent the thresh- olds at the start and end of the SK-IV period.	30
2444	2.3	The threshold momentum and energy for a particle to generate Cherenkov light in ultrapure water, as calculated in Equation 2.2 in ultrapure water which has refractive index $n = 1.33$	31
2447	3.1	Jeffreys scale for strength of preference for two models A and B as a function of the calculated Bayes factor ($B_{AB} = B(A/B)$) between the two models [132]. The original scale is given in terms of $\log_{10}(B(A/B))$ but converted to linear scale for easy comparison throughout this thesis.	64
2451	5.1	Reference values of the neutrino oscillation parameters for two different oscillation parameter sets.	93
2453	5.2	Description of the four layers of the Earth invoked within the average constant density approximation of the PREM model [187].	105
2455	5.3	The quadratic polynomial fits to the PREM model for four assumed layers of the PREM model. The fit to calculate the coefficients is given in [192], where $x = R/R_{Earth}$	108